

Multidimensional supernova simulations with approximative neutrino transport

I. Neutron star kicks and the anisotropy of neutrino-driven explosions in two spatial dimensions

L. Scheck, K. Kifonidis, H.-Th. Janka, and E. Müller

Max-Planck-Institut für Astrophysik, Karl-Schwarzschild-Straße 1, D-85741 Garching, Germany

received; accepted

Abstract. By means of two-dimensional (2D) simulations we study hydrodynamic instabilities during the first seconds of neutrino-driven supernova explosions. We use a PPM hydrodynamics code, supplemented with an approximative, gray, non-equilibrium treatment of radial neutrino transport, based on an analytic integration of the neutrino number and energy equations. Tests show that this treatment reproduces basic features of more detailed transport calculations in the semitransparent and transparent regimes. It is sufficiently fast to allow us to compute a large number of models with high spatial resolution. Our simulations start with post-core bounce models of three $15 M_{\odot}$ progenitors that have markedly different density profiles, and one $15 M_{\odot}$ star that includes rotation. The dense core of the contracting, newly formed neutron star is replaced at neutrino optical depths of typically more than 100 by an inner boundary at which the incoming neutrino fluxes are imposed as a systematically varied boundary condition, thus triggering neutrino-driven explosions. Confirming more idealised studies as well as supernova simulations with spectral transport, we find that random seed perturbations can grow by hydrodynamic instabilities to a globally asymmetric mass distribution in the region between the nascent neutron star and the accretion shock, leading to a dominance of dipole ($l = 1$) and quadrupole ($l = 2$) modes in the explosion ejecta, provided the onset of the supernova explosion is sufficiently slower than the growth time scale of the low-mode instability. By gravitational and hydrodynamic forces, the anisotropic mass distribution causes an acceleration of the nascent neutron star, which lasts for several seconds and can propel the neutron star to velocities of more than 1000 km s^{-1} . Because the explosion anisotropies develop chaotically and change by small differences in the fluid flow, the magnitude of the kick varies stochastically. No systematic dependence of the average neutron star velocity on the explosion energy or the properties of the considered progenitors is found, but the kick seems to increase when the nascent neutron star contracts more quickly. Our more than 70 models separate into two groups, one with high and the other with low neutron star velocities and accelerations after one second of post-bounce evolution, depending on whether the $l = 1$ mode is dominant in the ejecta or not. This leads to a bimodality of the distribution when the neutron star velocities are extrapolated to their terminal values. Establishing a link to the measured distribution of pulsar velocities, however, requires a much larger set of calculations and ultimately 3D modelling.

Key words. hydrodynamics – instabilities – radiative transfer – neutrinos – supernovae: general – pulsars: general

1. Introduction

Spectropolarimetry (Wang et al. 2001, 2003, and references therein) indicates that global anisotropies are a common feature of many core-collapse supernovae (SNe). Since the asymmetry inferred from the observed polarisation grows with the depth one can look into the expanding supernova ejecta, the origin of the anisotropy seems to be intrinsically linked to the mechanism of the explosion. Recent high-resolution imaging of SN 1987A with the Hubble Space Telescope (Wang et al.

2002) as well as large values for the measured space velocities of young galactic pulsars may be interpreted as a support of such a link. The average pulsar velocities are as high as $200\text{--}500 \text{ km/s}$, and some neutron stars (NSs) move through interstellar space with more than 1000 km/s (e.g. Cordes et al. 1993; Lyne & Lorimer 1994; Hansen & Phinney 1997; Zou et al. 2005; Chatterjee et al. 2005). Claims of a bimodality of the pulsar velocity distribution are still controversial. While some authors have obtained evidence for such a bimodality (Cordes & Chernoff 1998; Fryer et al. 1998; Arzoumanian et al. 2002; Brisken et al. 2003), others found that a simple Maxwellian fit works best (Hansen & Phinney 1997; Hobbs et al. 2005).

Send offprint requests to: L. Scheck
Correspondence to: scheck@mpa-garching.mpg.de

Binary disruption, e.g. as a consequence of the SN explosions which give birth to the NSs, does not lead to suffi-

ciently high velocities, and also the orbital parameters of many binary systems imply an intrinsic acceleration mechanism of the pulsars, probably linked to their creation (see Lai 2001; Lai et al. 2001 for reviews). Quite a number of explanations have been suggested, mostly involving anisotropic mass ejection in the SN explosion or anisotropic neutrino emission of the cooling, nascent NS. The former suggestion might be supported by the fact that some pulsars seem to propagate in a direction opposite to mass distribution asymmetries of their associated SN remnants. But a clear observational evidence is missing, and hydrodynamic simulations have previously either produced rather small recoil velocities (Janka & Müller 1994), or started from the assumption that a dipolar asymmetry was already present in the pre-collapse iron core and thus gave rise to a large anisotropy of the SN explosion (Burrows & Hayes 1996). The origin of such big pre-collapse perturbations, however, is not clear (Murphy et al. 2004). Suggestions that a “neutrino rocket engine” boosts NSs to big velocities make use of the fact that the huge reservoir of gravitational binding energy released during the collapse of the stellar core is mostly carried away by the neutrinos. Creating a global emission anisotropy of these neutrinos of even only 1% — which is sufficient to obtain a NS recoil of about 300 km s^{-1} —, however, turned out to be very difficult. Most ideas refer to unknown neutrino properties (e.g., Fuller et al. 2003; Fryer & Kusenko 2005 and refs. therein) and/or require the presence of a very strong magnetic field with a large dipole component (instead of being randomly structured and variable with time) in the newly formed NS (e.g. Arras & Lai 1999a,b; Socrates et al. 2005). Such assumptions are not generally accepted and are not the result of self-consistent calculations but put into the models “by hand”.

If the observed high pulsar velocities indeed go back to the early moments of the SN explosion, the simplest explanation would certainly be a common origin of explosion asymmetries and pulsar acceleration, in which case anisotropic ejection of mass would lead to a recoil (or “kick”) of the NS due to (linear) momentum conservation. Various kinds of hydrodynamic instabilities might in fact be responsible for a large-scale deformation of the ejecta and globally aspherical explosions. Motivated by a perturbation analysis of volume-filling thermal convection in a fluid sphere by Chandrasekhar (1961), who found largest growth rates for the $l = 1, m = 0$ mode (in terms of an expansion in spherical harmonics Y_l^m of order l, m), Herant (1995) speculated about the formation of a stable $l = 1, m = 0$ convective mode in the neutrino-heated layers between the gain radius and the supernova shock. In this configuration there exists only a single buoyant bubble (outflow), and a single accretion funnel (inflow), which reaches from the postshock region down to the NS. Herant (1995) suggested the potential importance of such a convective pattern for NS kicks up to nearly 1000 km/s. Instability of the accretion shock to a global Rayleigh-Taylor mode which could lead to asymmetric shock expansion and a net recoil of the NS of several 100 km/s was also predicted by Thompson (2000). However, according to the linear analysis by Foglizzo et al. (2005), advection tends to stabilise the growth of long-wavelength perturbations in the neutrino-heated accretion flow behind the standing shock. A

convective trigger of such instabilities therefore requires the growth rate to exceed a critical threshold value.

Non-radial, low-mode instability of shocked accretion flows can also be caused by the “advection-acoustic cycle”. In the astrophysical context, this instability was first discussed by Foglizzo & Tagger (2000) and Foglizzo (2001, 2002) in application to Bondi-Hoyle accretion of black holes. It was more recently considered for supernova-core like conditions by Galletti & Foglizzo (2005). Blondin et al. (2003) investigated numerically an idealised setup for the stalled shock in a supernova core and showed that a spherical shock is dynamically unstable to non-radial perturbations, even without neutrino heating and convection. The authors referred to this as the “standing accretion shock instability”, or SASI, which reveals a preferred growth of $l = 1$ mode deformation (Blondin & Mezzacappa 2005) and was explained by Blondin & Mezzacappa (2005) as a consequence of the propagation of sound waves in the volume enclosed by the shock.

While these investigations lacked the use of a detailed description of the neutrino physics and of the equation of state of the supernova medium, Scheck et al. (2004); Janka et al. (2005b, 2004b, 2005a), and Ohnishi et al. (2005) provided results which demonstrate that the instability of the accretion shock also occurs in models which include the relevant microphysics with more realism. Scheck et al. (2004) suggested a link of these low-mode instabilities of the supernova shock during the neutrino-heating phase to global explosion asymmetries (see also Kifonidis et al. 2005) and pulsar kicks. Most previous two-dimensional (2D) simulations of successful neutrino-driven explosions (Herant et al. 1992; Herant et al. 1994; Burrows & Fryxell 1993; Burrows et al. 1995) failed to see the development of $l = 1, 2$ modes — such an anisotropy, however, showed up in one of the models with a weak explosion in Janka & Müller 1996 — because most of the simulations were done with limited computational wedges of only 90° to 120° latitudinal width, or because very rapid explosions were obtained. In these cases the low-mode asymmetries were excluded by constraining boundary conditions or they could not grow in the time available between shock stagnation and revival. The neutron star recoil velocities remained correspondingly low (typically less than about 200 km/s, see Janka & Müller 1994).

The main goal of this paper (the first in a series) is to show that global anisotropies and large NS kicks can be obtained naturally in the framework of the neutrino-driven SN explosion mechanism due to the symmetry breaking by hydrodynamic instabilities, without the need to resort to rapid rotation (e.g. Kotake et al. 2003), large pre-collapse perturbations in the iron core (Burrows & Hayes 1996; Goldreich et al. 1996; Lai & Goldreich 2000), strong magnetic fields (Wheeler et al. 2002; Kotake et al. 2004), anisotropic neutrino emission associated with exotic neutrino properties (e.g. Fryer & Kusenko 2005; Fuller et al. 2003), or jets (Cen 1998; Khokhlov et al. 1999; Lai et al. 2001). To this end we present a comprehensive 2D study of supernova dynamics that can be considered as a significant improvement and extension of the earlier calculations of Janka & Müller (1996) with respect to the treatment of neutrino transport, the assumed characteristics of the neu-

trino emission from the neutron star core, the inclusion of rotation, the influence of the initial seed perturbations, the spatial resolution, and the covered evolutionary time of the supernova explosions.

We have developed a simple, yet sufficiently accurate neutrino transport scheme for the transparent and semi-transparent regimes, that allows us to study fundamental aspects of the still poorly understood interaction between hydrodynamic instabilities and neutrino heating for a large number of multidimensional models. We do not attempt here to follow the transport of neutrinos seamlessly from the optically thick core of the proto-neutron star into the optically thin regime. Such an approach (see for example Buras et al. 2005a and references therein) ultimately requires a Boltzmann transport solver, which is computationally too expensive for performing the large number of simulations that we will present in this study. Instead, we treat the fluxes and spectra of the neutrinos emitted from the neutron star core as a boundary condition, and explore the explosion dynamics in dependence of systematic variations, limited by fundamental constraints, of the neutrino emission properties of the nascent neutron star. Our models are therefore parametric studies and based on the assumption that the convectively supported neutrino-heating mechanism (Herant et al. 1994; Burrows et al. 1995; Janka & Müller 1996) works. The viability of neutrino-driven supernova explosions for progenitor stars of more than $\approx 10 M_{\odot}$, however, is still an open question (see, e.g., Buras et al. 2003, 2005a,b).

Parts of the present work were already presented in a Letter by Scheck et al. (2004), but a detailed description of both our methods and results will be given here. We proceed by summarising our numerical algorithms and computational approach in Sect. 2. We then discuss in Sect. 3 the considered progenitor stars and define physical quantities which characterise the different runs of our large set of simulations. Moreover, we describe the post-processing procedures that we applied to the numerical calculations to compute these characteristic quantities. In Sect. 4 we present results for two exemplary neutrino-hydrodynamic calculations. In Section 5 we explore the dependence of our simulations on the properties of the stellar progenitors and on the assumed core neutrino fluxes, and establish correlations between explosion parameters and neutron star kicks. Section 6 is devoted to the effects of rotation. In Sect. 7 we return to the neutron star recoils and investigate their robustness with respect to the approximations and assumptions that we have employed. Furthermore, we investigate the long-time evolution of the recoil velocities for a few models beyond the time interval of one second after core bounce, for which we have evolved most of our models. Estimating the terminal values of the NS velocities by a calibrated extrapolation procedure, we will speculate about the possible implications of our results for the velocity distribution of neutron stars in Sect. 8. Section 9, finally, contains our conclusions. Appendix A contains a detailed description of our neutrino transport scheme, in Appendix B we discuss the solution of the hydrodynamics equations in an accelerated frame of reference, and in Appendix C we analyse the explosion energetics of the neutrino-driven supernovae in our simulations.

2. Computational approach and numerical methods

2.1. Hydrodynamics and gravity

The basic version of the computer program that we employ for this study is described in Kifonidis et al. (2003). It consists of a hydrodynamics module which is based on the direct Eulerian version of the Piecewise Parabolic Method (PPM) of Colella & Woodward (1984) (augmented by the HLL solver of Einfeldt 1988 to avoid the odd-even-decoupling instability), and a module that computes the source terms for energy and lepton number which enter the hydrodynamic equations due to neutrino absorption, scattering, and emission processes (see below). The equation of state is that of Janka & Müller (1996). It includes contributions by photons, electrons and positrons of arbitrary degeneracy and relativity, and non-degenerate neutrons, protons, α 's and a representative nucleus of the iron group (in our case this nucleus is chosen to be ^{54}Mn). In contrast to Kifonidis et al. (2003, 2005) we do not follow explosive nucleosynthesis in this work. This allows us to save a considerable amount of computer time, which is mandatory for carrying out an extended parameter study like the one presented here.

Following Kifonidis et al. (2003), we include relativistic corrections in our otherwise Newtonian code by replacing the “spherical part” of the gravitational potential of the 2D mass distribution by the “effective relativistic potential” of Rampp & Janka (2002) (for details, see Marek et al. 2005). For describing the gravity of the central “point mass” (i.e., the mass enclosed by the inner boundary) we use the baryonic mass where Eq. (53) in Rampp & Janka (2002) requires the gravitational mass. This turned out to yield very good agreement with the improved version of the effective relativistic potential developed by Marek et al. (2005).

2.2. Neutrino transport and neutrino source terms

The original code version of Kifonidis et al. (2003) made use of a simple light-bulb approximation (Janka & Müller 1996) in which luminosities of neutrinos and antineutrinos of all flavours were imposed at the inner boundary (which is usually below the neutrinospheres) and kept constant with radius. These luminosities were typically *not* chosen to give accurate values for the fluxes prevailing below the neutrinospheric layers, but their choice was guided by the asymptotic luminosities that emerge from the contracting and accreting nascent neutron star at *large* radii. This was necessary in order to cope with the main problem of a light-bulb approach, namely that it neglects changes of the neutrino fluxes and spectra that result from the interactions of neutrinos with the stellar matter, thus ignoring, for example, the contributions of the neutrino emission from accreted matter to the neutrino luminosity.

In this work we considerably improve upon this former approach by explicitly including these effects. We achieve this by abandoning the light bulb in favour of a gray, characteristics-based scheme which can approximate neutrino transport in the transparent and semi-transparent regimes. The approach is not particularly suitable to handle also the regime of very large

optical depths, τ . Therefore we still do our simulations with an inner grid boundary at $\tau \approx 10 \dots 100$. However, the luminosities prescribed there have no relation to those used in the older light-bulb calculations. We have chosen them to reproduce qualitatively the evolution of the luminosities in a Lagrangian mass shell below the neutrinospheres as obtained in recent Boltzmann transport calculations. More details will be given in Sect. 2.4.2.

The transport scheme itself solves the zeroth order moment equation of the Boltzmann transport equation in spherical symmetry in the form

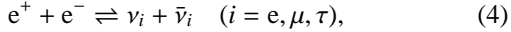
$$\frac{\partial}{\partial t} L + c_{\text{eff}} \frac{\partial}{\partial r} L = 4\pi r^2 c_{\text{eff}} Q_v^+ - \kappa c L. \quad (1)$$

Here $L(r, t)$ stands for the neutrino number flux or the neutrino luminosity, Q_v^+ is the neutrino number or energy production rate per unit volume (which is equal to the corresponding loss rate of the stellar medium), and κ is the corresponding absorptivity. The “effective speed” of the neutrino propagation, c_{eff} , is governed by diffusion at high densities and reaches the speed of light, c , at large radii and low optical depths. Equation (1) has been derived under the assumption that $\partial_t c_{\text{eff}} = 0$. It can be solved analytically, when Q_v^+ , κ and c_{eff} are assumed to be constant within each cell of the numerical grid. For c_{eff} a functional form in dependence of τ is adopted, which fits the results of detailed transport simulations in neutron star “atmospheres”.

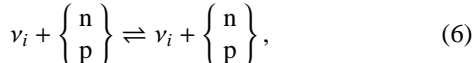
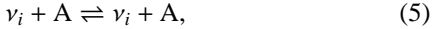
The neutrino-matter interaction rates are calculated using the assumption that the spectra have Fermi-Dirac form. Charged-current processes with neutrons (n) and protons (p),



thermal electron-positron (e^\pm) pair creation and annihilation,



and neutrino scattering off nuclei (A), nucleons, and electrons and positrons,



are taken into account.

We solve Eq. (1) for neutrino number and energy transport separately for neutrinos and antineutrinos of all flavours (e, μ, τ). This allows us to adopt a non-equilibrium description of the transport in the sense that the spectral form is assumed to be Fermi-Dirac, but the neutrino temperatures T_{ν_i} are not necessarily equal to the gas temperature T . Solving two transport equations for neutrino number and energy, we therefore can determine locally neutrino number and energy densities and thus the spectral temperatures T_{ν_i} from the mean neutrino energies. A detailed description of our approximative solution of the non-equilibrium transport problem and the exact expressions for the employed interaction kernels can be found in Appendix A. While giving qualitatively similar results as

Boltzmann-solvers in spherical symmetry (cf. Sect. 4.4), the computational cost of this approximative transport scheme is two orders of magnitude lower.

Equation (1) describes the neutrino transport in the radial direction only. Transport in the lateral direction is ignored in our two-dimensional simulations, but lateral variations of the neutrino quantities are allowed for by applying the radial transport solver independently on different radial “rays” corresponding to the different angular (i.e. lateral in 2D) directions of our polar grid.

2.3. Numerical grid

We adopt 2D spherical coordinates (r, θ) and assume axisymmetry. Unless noted otherwise, the calculations presented in the following are carried out in a full sphere, i.e. $0 \leq \theta \leq \pi$ (in 2D), with a grid that is equidistant in the lateral direction. A non-equidistant grid is employed in the radial direction whose local spacing, Δr , is chosen such that square-shaped cells are obtained in the convective region, i.e. $\Delta r \approx r\Delta\theta$. Typically 400 radial and 180 lateral zones are used.

The outer boundary of the computational domain is typically located at $R_{\text{ob}} \approx 2 \times 10^4$ km, while the inner boundary is placed within the forming neutron star after core bounce, at a *Lagrangian* mass shell somewhat below the electron neutrinosphere. The spacing of the zones near and below the neutrinospheres is chosen such that variations of the optical depth per zone remain smaller than a few. The baryonic matter of the neutron star interior to the inner boundary, M_{core} (which is typically $\sim 1.1 M_\odot$), is removed and its gravitational attraction is taken into account by assuming a point mass at $r = 0$ (see Sect. 2.1).

Since we are mainly interested in neutron star kicks in this paper, we need to point out that the use of the inner boundary condition (enclosing the neutron star “core”) implies that the neutron star is attached to the centre of our computational grid. It is therefore not free to move relative to the ejecta during the simulation (unless special measures are taken, see below). This is tantamount to assuming that the neutron star has an infinite *inertial* mass. Two implications result from this approximation: A potential hydrodynamic feedback of a displacement of the neutron star relative to the ejecta is neglected, and the neutron star recoil velocity has to be determined indirectly in a post-processing step by making use of the assumption of total momentum conservation (see Sect. 3.2).

The relative motion between neutron star and ejecta can, however, be accounted for during a simulation by “wagging the dog”, i.e. by assuming that instead of the neutron star the ejecta move coherently in the opposite direction of the neutron star’s recoil velocity. This can be achieved technically by applying a Galilei transformation to the gas on the computational grid after every time step. To accomplish this for several of our computed models (Table 5), we assume that the frame of reference connected with the neutron star core is (in a first approximation) an inertial frame (see Appendix B for a justification of this assumption). We then evaluate for every time step n the change of the total linear momentum of the matter on the

grid, $\Delta\mathbf{P}_{\text{grid}}^n$. By virtue of momentum conservation this must be equal to the change of the momentum of the neutron star core. In case the core mass is constant, this gives

$$\Delta\mathbf{P}_{\text{grid}}^n = -M_{\text{core}}^n \Delta\mathbf{v}_{\text{core}}^n. \quad (8)$$

Hence, after the time step, the core should move with a velocity that has changed by $\Delta\mathbf{v}_{\text{core}}^n$. Changing the frame of reference instead, we perform a Galilei transformation by adding $-\Delta\mathbf{v}_{\text{core}}^n$ to the gas velocities in all zones of the grid. In the new inertial frame the neutron star core remains at rest and centred at $r = 0$. Simulations including this procedure will be used to investigate potential deficiencies of our standard assumption that the NS has an infinite inertial mass and takes up momentum without starting to move (see Sects. 4.2 and 7).

2.4. Boundary conditions

2.4.1. Hydrodynamics

The boundary conditions for the hydrodynamics equations are defined similar to those in Kifonidis et al. (2003). Reflecting conditions are imposed at the lateral boundaries at $\theta = 0$ and $\theta = \pi$, while transmitting (i.e. zero gradient) boundary conditions are employed at the outer radial boundary.

The inner boundary, which is located at the Lagrangian mass coordinate where we cut our initial (i.e. immediate post-bounce) models, is taken to be impenetrable. The contraction of this mass shell (and hence of the neutron star core) is mimicked by moving the inner boundary of our Eulerian grid from its initial radius, R_{ib}^i , inwards to a final radius R_{ib}^f according to the expression

$$R_{\text{ib}}(t) = \frac{R_{\text{ib}}^i}{1 + (1 - \exp(-t/t_{\text{ib}})) (R_{\text{ib}}^i/R_{\text{ib}}^f - 1)} \quad (9)$$

of Janka & Müller (1996). The parameter R_{ib}^i is typically in the range $55 \text{ km} < R_{\text{ib}}^i < 85 \text{ km}$.

For R_{ib}^f and t_{ib} we use two alternative prescriptions: In what we henceforth will call the “standard boundary contraction case”, we set $R_{\text{ib}}^f = 15 \text{ km}$ and $t_{\text{ib}} = t_L$, where the time scale t_L is connected to the luminosity decay and will be defined in Sect. 2.4.2. In the second prescription, the so-called “rapid boundary contraction case”, we set $R_{\text{ib}}^f = 10.5 \text{ km}$ and $t_{\text{ib}} = 0.25 \text{ s}$.

Figure 1 compares both prescriptions with each other and with data from a supernova simulation with the nuclear equation of state of Lattimer & Swesty (1991) and with Boltzmann neutrino transport (Buras et al. 2003) for one of our initial models. The standard boundary contraction results in a larger final radius and a slower contraction of the neutron star. The rapid boundary contraction gives results which are almost indistinguishable from the Boltzmann calculation, and might therefore be considered as more realistic. The standard case has practical advantages, though, because it allows for larger time steps and thus reduces the computational cost of a simulation. Unless noted otherwise, the simulations are performed for the standard contraction of the inner boundary.

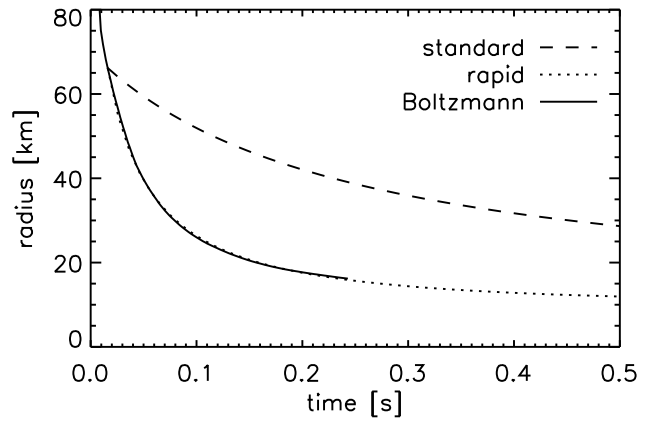


Fig. 1. Evolution after core bounce of the radius corresponding to a mass coordinate of $1.1M_{\odot}$ from a supernova simulation with Boltzmann neutrino transport (Buras et al. 2003), compared to the motion of the inner boundary radius as defined by Eq. (9) for the standard and rapid boundary contraction cases.

2.4.2. Neutrinos

The boundary conditions for the neutrino properties at the inner grid boundary are chosen to be *isotropic*. We impose luminosities for neutrinos and antineutrinos of all three flavours which are assumed to be constant for a time interval t_L (typically 1 s), and to decay subsequently with a power-law:

$$L_{e,\nu_e}(R_{\text{ib}}, t) = L_{\nu}^{\text{tot},0} K_{\nu_e} f(t), \quad (10)$$

$$L_{e,\bar{\nu}_e}(R_{\text{ib}}, t) = L_{\nu}^{\text{tot},0} K_{\bar{\nu}_e} f(t), \quad (11)$$

$$L_{e,\nu_x}(R_{\text{ib}}, t) = L_{\nu}^{\text{tot},0} K_{\nu_x} f(t), \quad (12)$$

where

$$f(t) = \begin{cases} 1.0 & \text{if } t \leq t_L, \\ (t_L/t)^{3/2} & \text{if } t > t_L, \end{cases} \quad (13)$$

and $\nu_x \equiv \nu_{\mu}, \bar{\nu}_{\mu}, \nu_{\tau}, \bar{\nu}_{\tau}$. The constants K_{ν_i} denote the fractional contributions of the individual luminosities to the total neutrino luminosity. They fulfil the requirement

$$K_{\nu_e} + K_{\bar{\nu}_e} + 4 K_{\nu_x} = 1. \quad (14)$$

The functional form used in Eq. (13) can be motivated by the Boltzmann transport calculations of Buras et al. (2003). These show that after a transient phase of $\sim 50 \text{ ms}$, which is short compared to the explosion time scales of our simulations, the sum of all luminosities is almost constant or varies only very weakly, at least over the next $\sim 250 \text{ ms}$, for which data from the Boltzmann transport simulations are available (see Fig. 2).

According to Eqs. (10–13) we need to prescribe the time scale t_L and the total initial luminosity $L_{\nu}^{\text{tot},0}$. However, instead of choosing these two quantities as basic parameters of our models, we prefer to prescribe t_L and the gravitational binding energy $\Delta E_{\text{core}}^{\infty}$ that is released by the neutron star core via neutrino emission. We then obtain $L_{\nu}^{\text{tot},0}$ from the constraint

$$\Delta E_{\text{core}}^{\infty} = \int_0^{\infty} L_{\nu}^{\text{tot},0} f(t) dt = 3 L_{\nu}^{\text{tot},0} t_L, \quad (15)$$

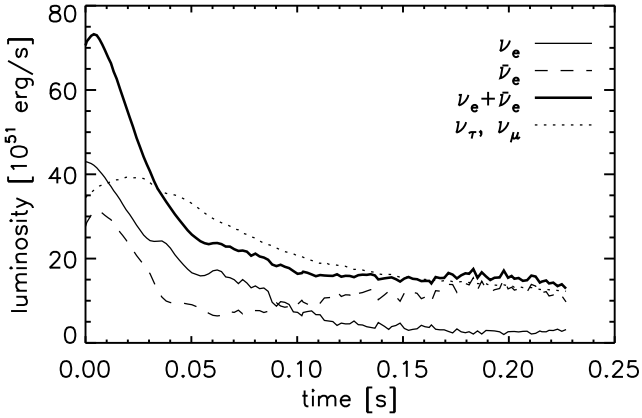


Fig. 2. Evolution after core bounce of the neutrino luminosities at a Lagrangian mass shell of $1.1 M_{\odot}$ from a supernova simulation with Boltzmann neutrino transport (Buras et al. 2003). After an initial phase of 50 ms duration, the sum of the ν_e and $\bar{\nu}_e$ luminosities as well as the ν_μ/ν_τ luminosities vary only slowly.

i.e. our ansatz of Eq. (13) implies that $1/3$ of $\Delta E_{\text{core}}^{\infty}$ is radiated away within the chosen time interval t_L in neutrinos and antineutrinos of all flavours.

Moreover, we prescribe the mean energies of neutrinos entering the computational grid at the inner boundary. The corresponding values are chosen to be $\langle \epsilon_{\nu_e} \rangle^{\text{ib}} = 12 \text{ MeV}$, $\langle \epsilon_{\bar{\nu}_e} \rangle^{\text{ib}} = 16 \text{ MeV}$, and $\langle \epsilon_{\nu_x} \rangle^{\text{ib}} = 20 \text{ MeV}$, and kept constant during our simulations. Thereby also the number fluxes $L_{n,\nu_i} = L_{e,\nu_i}/\langle \epsilon_{\nu_i} \rangle$ at $r = R_{\text{ib}}$ are defined.

L_{e,ν_i} and L_{n,ν_i} for $\nu_i = \nu_e, \bar{\nu}_e, \nu_x$ allow us to solve Eq. (1) by integrating from the inner boundary outwards (provided $c_{\text{eff}} > 0$, see Appendix A). The total lepton number lost by the neutron star core until time t , normalised to the total baryon number $N_{\text{b, core}}$ of the core, is given by

$$\Delta Y_{\text{e,core}}(t) = N_{\text{b,core}}^{-1} \int_0^t (L_{n,\nu_e}(R_{\text{ib}}, t') - L_{n,\bar{\nu}_e}(R_{\text{ib}}, t')) dt'. \quad (16)$$

For $t = t_L$ this yields

$$\Delta Y_{\text{e,core}}(t_L) = \frac{L_{\nu}^{\text{tot,0}} t_L}{N_{\text{b,core}}} \left(\frac{K_{\nu_e}}{\langle \epsilon_{\nu_e} \rangle^{\text{ib}}} - \frac{K_{\bar{\nu}_e}}{\langle \epsilon_{\bar{\nu}_e} \rangle^{\text{ib}}} \right). \quad (17)$$

We assume that the lepton number loss during time interval t_L is proportional to the energy loss during this time. Therefore we choose $K_{\nu_i} = \text{const}$, because $\langle \epsilon_{\nu_i} \rangle^{\text{ib}} = \text{const}$, and set $K_{\nu_e} = 0.2$, $K_{\bar{\nu}_e} = 0.215$ for the calculations in this paper. K_{ν_x} follows from Eq. (14).

3. Preliminaries

3.1. Initial models and initial perturbations

Our calculations are started at $\sim 15 - 20$ ms after core bounce from detailed post-collapse models. We make use of four such models which are based on three different progenitors. The first was calculated by Bruenn (1993) with a general relativistic,

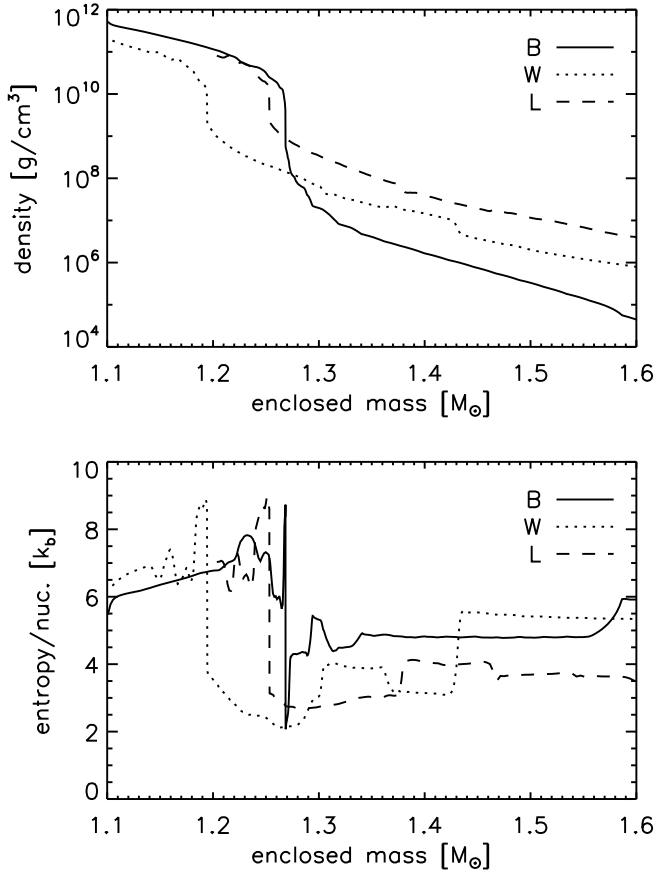


Fig. 3. Density and entropy as functions of the enclosed mass for the B, L and W initial models a few milliseconds after core bounce (see the main text for details). The differences in the density profiles have a strong influence on the mass accretion rates. The relatively low densities in the B model lead to a small accretion rate and a fast onset of the explosion. The opposite is true for the L model, which shows the highest densities (see Sect. 5). The small steps in the density profiles correspond to interfaces separating shells of different composition. These interfaces are better visible in the entropy profiles. The pronounced “discontinuity” at $\rho = 10^{10} \text{ g/cm}^3$ is the supernova shock.

one-dimensional (1D), Lagrangian hydrodynamics code coupled to neutrino transport by multi-group, flux-limited diffusion (see his Model WPE15 LS 180). It employs the $15 M_{\odot}$ progenitor of Woosley et al. (1988). Simulations based on this model will henceforth be called the “B-series”.

Our second 1D post-collapse model, provided by M. Rampp (priv. comm.), uses a $15 M_{\odot}$ progenitor star of Limongi et al. (2000) and was computed with the PROMETHEUS PPM hydrodynamics code coupled to the VERTEX multi-group variable Eddington factor/Boltzmann neutrino transport solver (Rampp & Janka 2002). Our “L-series” of simulations makes use of that model.

We also consider two post-bounce models that were computed for the s15s7b2 progenitor of Woosley & Weaver (1995) with PROMETHEUS/VERTEX by Buras et al. (2003, 2005a) (see

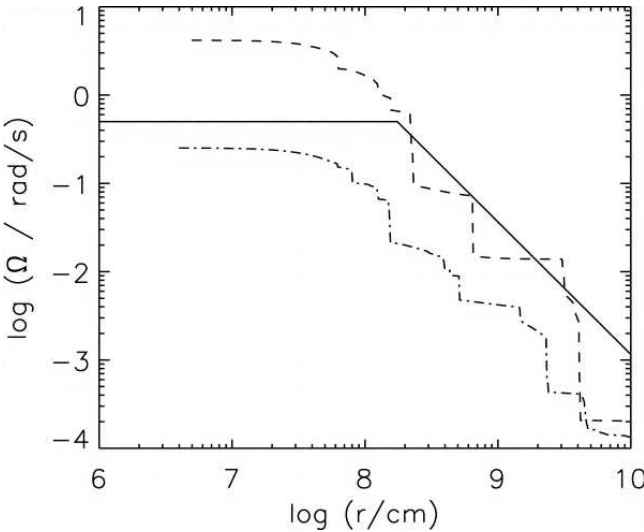


Fig. 4. Angular velocity profiles for the rotating $15M_{\odot}$ pre-supernova model (dashed curve) of Heger et al. (2000), for the magnetised, rotating $15M_{\odot}$ pre-supernova model (dash-dotted curve) of Heger et al. (2004), and for the rotating model s15r of Buras et al. (2003) prior to core collapse (solid curve).

their Models s15/1D and s15r). The first of these models is from a one-dimensional simulation and gives rise to the “W-series” of runs, while the second is a rotating, two-dimensional (axisymmetric) model, which we use for our “R-series” of calculations. Density and entropy profiles of all 1D initial models plotted as a function of the enclosed mass are displayed in Fig. 3.

To obtain the rotating model, Buras et al. (2003, 2005a) imposed the angular velocity profile shown in Fig. 4 on the s15s7b2 progenitor and followed the evolution of this model through core bounce, assuming equatorial symmetry and using a computational wedge extending over $0 \leq \theta \leq \pi/2$. The initial angular frequency was assumed to be constant in the Fe and Si core and to decrease as $r^{-3/2}$ outside a radius of 1750 km (corresponding to a mass coordinate of $1.425 M_{\odot}$, which is the inner edge of the oxygen-rich silicon layer in the progenitor). Outside the iron core the rotation profile followed (on average) the profile of the rotating $15 M_{\odot}$ progenitor of Heger et al. (2000). Inside the iron core an angular frequency of $\Omega = 0.5 \text{ rad/s}$ was chosen, which is lower than in the stellar evolution calculations for non-magnetised stars of Heger et al. (2000), but somewhat higher than in the calculations of Heger et al. (2004), which include the effects of magnetic torques. This choice ensured that the ratio of the centrifugal to the gravitational force was below 7×10^{-3} everywhere in the pre-collapse core. The ratio of the rotational energy to the gravitational binding energy of the pre-collapse star was only $T/W \approx 10^{-3}$, which resulted in negligible effects of rotation on the evolution until core bounce.

The level of numerical noise in our hydrodynamics code is so low that a one-dimensional, isotropic initial configuration remains isotropic, even in the presence of a convectively unstable stratification. Therefore we need to explicitly add random perturbations in order to start the convective activity. The portable, high-quality random number generator RANLUX due to James

(1994, 1996) and Lüscher (1994) is employed. We apply the perturbation to the velocity field and typically use an amplitude of 0.1%. To break the equatorial symmetry of the rotating 2D model of Buras et al. (2003, 2005a), we have to add perturbations with an amplitude of several per cent, since in this model the initial perturbations have already grown to such a level by the time we map the model to our full 180° grid (see Sect. 2.3).

3.2. Definitions and approximations for post-processing the simulations

We evaluate our about 80 hydrodynamic models for interesting characteristic quantities by post-processing the data of the simulations. To keep the evaluation as straightforward as possible we sometimes employ approximations which we will define below.

The two parameters which constrain the inner boundary condition for the neutrinos, $\Delta Y_{e,\text{core}}(t)$ (Eq. 16) and

$$\Delta E_{v,\text{core}}^{\text{tot}}(t) = \int_0^t L_v^{\text{tot}}(R_{\text{ib}}, t') dt', \quad (18)$$

are given at a time $t = 1 \text{ s}$ in Tables 1–5.

A characterising value for the neutrino luminosities imposed at the inner boundary is

$$L_{\text{ib}}(t) \equiv L_{e,\nu_e}(R_{\text{ib}}, t) + L_{e,\bar{\nu}_e}(R_{\text{ib}}, t), \quad (19)$$

neglecting the contribution from heavy-lepton neutrinos, whose interactions in the computational domain are less important than those of ν_e and $\bar{\nu}_e$, and who, in particular, do not contribute to the neutrino heating behind the shock at a significant level. We also consider the sum of the ν_e and $\bar{\nu}_e$ luminosities at a radius of 500 km,

$$L_{500}(t) = L_{e,\nu_e}(r = 500 \text{ km}, t) + L_{e,\bar{\nu}_e}(r = 500 \text{ km}, t), \quad (20)$$

and define the time average of this quantity in the time interval $[0, t_{\text{exp}}]$ as

$$\langle L_{500} \rangle = t_{\text{exp}}^{-1} \int_0^{t_{\text{exp}}} L_{500}(t) dt. \quad (21)$$

The value of $\langle L_{500} \rangle$ represents approximatively the $(\nu_e + \bar{\nu}_e)$ luminosity that is responsible for the energy deposition behind the supernova shock until the explosion sets in at a post-bounce time $t = t_{\text{exp}}$. Therefore the difference between $\langle L_{500} \rangle$ and L_{ib} can be considered as a rough measure for the radial change of the neutrino luminosities in contrast to their constancy in case of the light-bulb scheme used by Janka & Müller (1996).

We will also consider the total energy in ν_e and $\bar{\nu}_e$ neutrinos that streams through a sphere with a radius of 500 km in the time interval $[0, t]$,

$$\Delta E_{500}(t) = \int_0^t (L_{e,\nu_e} + L_{e,\bar{\nu}_e})(r = 500 \text{ km}, t') dt'. \quad (22)$$

The explosion energy, E_{exp} , of a model is defined as the sum of the total energy of all zones of the grid where this energy is positive, i.e.

$$E_{\text{exp}} = \sum_{e_{\text{tot},i} > 0} e_{\text{tot},i} \Delta m_i, \quad (23)$$

Table 1. Simulations based on the Woosley et al. (1988)/Bruenn (1993) post-bounce model. The luminosity time scale t_L is 1 s. Unless noted otherwise the inertial mass of the neutron star is assumed to be infinite for these and the simulations listed in the following tables, i.e. the neutron star takes up momentum but cannot move on the grid. For the definitions of the listed quantities, see Sect. 3.2. All time-dependent quantities are given at a time $t = 1$ s, when we terminated the simulations. Energies are given in units of 1 B = 1 bethe = 10^{51} erg.

Model	L_{ib} [B/s]	$\Delta E_{\nu, \text{core}}^{\text{tot}}$ [B]	$\Delta Y_{e, \text{core}}$	$\langle L_{500} \rangle$ [B/s]	ΔE_{500} [B]	E_{exp} [B]	t_{exp} [s]	M_{ns} [M_{\odot}]	v_z^{ns} [km/s]	$v_z^{\text{ns}, \nu}$ [km/s]	a_z^{ns} [km/s 2]	α_{gas}	d_{shock}
B10	24.7	59.6	0.09	57.1	45.9	0.19	0.294	1.426	-164.1	44.4	-180.2	0.24	0.67
B11	27.2	65.5	0.10	58.8	46.3	0.27	0.280	1.401	-23.6	0.7	-248.9	0.03	0.97
B12	29.7	71.5	0.11	60.6	48.7	0.37	0.220	1.399	-389.5	45.0	-372.4	0.32	0.06
B12-1	29.7	71.5	0.11	60.5	47.5	0.33	0.228	1.377	72.8	-4.7	47.9	0.07	0.22
B12-2	29.7	71.5	0.11	60.9	48.5	0.39	0.212	1.391	85.8	9.7	345.7	0.07	0.82
B12-3	29.7	71.5	0.11	60.9	46.5	0.38	0.207	1.369	242.0	2.0	464.3	0.18	0.97
B12-4	29.7	71.5	0.11	61.1	47.7	0.35	0.216	1.385	-115.1	20.4	-154.2	0.10	0.51
B12-5	29.7	71.5	0.11	61.0	47.8	0.33	0.211	1.387	-206.9	11.6	-483.1	0.19	0.52
B13	32.2	77.5	0.12	62.4	49.6	0.45	0.188	1.378	-355.3	32.0	-408.0	0.25	0.36
B14	34.6	83.4	0.13	63.6	49.6	0.51	0.198	1.345	-128.0	-11.2	-66.7	0.07	0.40
B15	37.1	89.4	0.14	65.3	50.3	0.65	0.162	1.318	36.1	-1.0	36.0	0.02	0.27
B16	39.6	95.3	0.15	66.3	51.8	0.81	0.160	1.305	-214.6	-2.6	-334.4	0.08	0.57
B17	42.1	101.3	0.15	67.6	53.3	0.95	0.146	1.289	-25.5	14.8	-102.6	0.01	0.05
B17-1	42.1	101.3	0.15	67.8	53.4	0.92	0.160	1.290	-354.0	5.6	-202.2	0.12	0.31
B18	44.5	107.3	0.16	68.3	54.8	1.16	0.152	1.275	515.3	5.2	290.5	0.15	0.42
B18-1	44.5	107.3	0.16	68.4	54.7	1.12	0.154	1.274	-126.5	-0.8	-49.1	0.04	0.20
B18-2	44.5	107.3	0.16	68.9	54.7	1.14	0.152	1.268	82.5	-5.2	16.5	0.02	0.07
B18-3	44.5	107.3	0.16	68.8	57.1	1.15	0.142	1.305	798.8	-41.2	552.1	0.24	-0.06
B18-4	44.5	107.3	0.16	68.2	54.6	1.14	0.150	1.272	-171.6	4.0	65.7	0.05	0.46
B18-5	44.5	107.3	0.16	68.5	55.2	1.09	0.164	1.280	-121.8	-0.9	15.4	0.04	-0.02
B18-6	44.5	107.3	0.16	68.7	55.4	1.11	0.160	1.283	502.1	-20.6	220.0	0.15	-0.06
B18-g1	44.5	107.3	0.16	68.7	54.5	1.12	0.142	1.269	-60.3	3.9	-55.4	0.02	0.06
B18-g2	44.5	107.3	0.16	68.7	54.8	1.12	0.138	1.273	267.9	-8.1	126.7	0.08	0.28
B18-g3	44.5	107.3	0.16	68.5	54.9	1.10	0.150	1.274	-7.4	-3.5	0.9	0.00	0.02
B18-g4	44.5	107.3	0.16	68.7	54.5	1.16	0.132	1.270	-416.8	1.7	-150.9	0.11	0.37
B19-g1	47.0	113.2	0.17	69.6	55.9	1.31	0.148	1.253	-273.8	0.3	-96.7	0.07	0.41
B19-g2	47.0	113.2	0.17	69.5	56.0	1.33	0.148	1.255	188.5	6.4	48.8	0.05	0.15
B19-g3	47.0	113.2	0.17	70.0	56.6	1.26	0.132	1.263	366.6	1.1	183.7	0.10	0.13
B19-g4	47.0	113.2	0.17	70.0	56.8	1.33	0.130	1.267	477.1	-18.3	195.6	0.12	-0.02
B20	49.5	119.2	0.18	71.0	57.3	1.49	0.128	1.238	133.2	5.6	52.6	0.03	0.40
B21	51.9	125.1	0.19	72.1	58.5	1.72	0.122	1.222	30.6	-0.9	-20.2	0.01	0.24

Table 2. Simulations based on the Limongi et al. (2000)/Rampp post-bounce model. The luminosity time scale t_L is 0.7 s for these simulations. For more details, see the caption of Table 1.

Model	L_{ib} [B/s]	$\Delta E_{\nu, \text{core}}^{\text{tot}}$ [B]	$\Delta Y_{e, \text{core}}$	$\langle L_{500} \rangle$ [B/s]	ΔE_{500} [B]	E_{exp} [B]	t_{exp} [s]	M_{ns} [M_{\odot}]	v_z^{ns} [km/s]	$v_z^{\text{ns}, \nu}$ [km/s]	a_z^{ns} [km/s 2]	α_{gas}	d_{shock}
L12	42.4	94.6	0.13	90.7	70.7	0.51	0.321	1.677	278.5	-12.9	334.3	0.24	0.11
L13	45.9	102.5	0.14	91.7	69.2	0.68	0.268	1.620	-92.6	-5.9	-333.6	0.05	0.77
L14	49.5	110.4	0.15	94.6	72.8	0.81	0.280	1.628	482.1	-22.0	297.1	0.26	0.31
L15	53.0	118.3	0.17	96.2	75.2	1.02	0.266	1.617	-239.5	-3.9	-378.5	0.10	0.63
L16	56.5	126.2	0.18	97.8	76.3	1.07	0.256	1.586	-437.9	12.8	-715.2	0.17	0.47
L17	60.1	134.0	0.19	100.3	77.4	1.19	0.256	1.558	-24.7	5.5	-47.6	0.01	0.37

where i is the zone counter, Δm_i the mass contained in zone i , and the total specific energy e_{tot} is given by the sum of the specific gravitational, kinetic, and internal energies,

$$e_{\text{tot}} = e_{\text{grav}} + \frac{1}{2} v^2 + e_{\text{int}}. \quad (24)$$

For the sake of simplicity we use here the one-dimensional Newtonian expression

$$e_{\text{grav}}(r) = -\frac{GM(r)}{r} \quad (25)$$

Table 3. Simulations based on the non-rotating Woosley & Weaver (1995)/Buras et al. (2003) post-bounce model. The luminosity time scale t_L is 1 s for these simulations. For more details, see the caption of Table 1.

Model	L_{ib} [B/s]	$\Delta E_{\nu,\text{core}}^{\text{tot}}$ [B]	$\Delta Y_{\text{e,core}}$	$\langle L_{500} \rangle$ [B/s]	ΔE_{500} [B]	E_{exp} [B]	t_{exp} [s]	M_{ns} [M_{\odot}]	v_z^{ns} [km/s]	$v_z^{\text{ns},\nu}$ [km/s]	a_z^{ns} [km/s 2]	α_{gas}	d_{shock}
W10	24.7	59.6	0.09	64.3	55.4	0.21	0.420	1.568	-129.8	42.1	-443.1	0.15	0.81
W12	29.7	71.5	0.11	69.0	53.9	0.31	0.322	1.501	-97.7	-9.7	-132.5	0.10	0.61
W12-1	29.7	71.5	0.11	68.0	59.5	0.32	0.374	1.563	-363.8	81.2	-377.0	0.32	0.13
W14	34.6	83.4	0.13	72.9	56.6	0.46	0.250	1.473	-62.0	-1.5	66.1	0.04	0.37
W16	39.6	95.3	0.15	76.0	58.5	0.67	0.244	1.430	287.2	-5.5	464.2	0.14	0.68
W18	44.5	107.3	0.16	79.3	61.5	0.89	0.226	1.401	-283.6	4.2	-290.1	0.11	0.44
W20	49.5	119.2	0.18	82.0	63.5	1.36	0.216	1.354	-377.3	0.6	-277.0	0.10	0.39

Table 4. Simulations based on the rotating Woosley & Weaver (1995)/Buras et al. (2003) post-bounce model. The luminosity time scale t_L is 1 s. For more details, see the caption of Table 1.

Model	L_{ib} [B/s]	$\Delta E_{\nu,\text{core}}^{\text{tot}}$ [B]	$\Delta Y_{\text{e,core}}$	$\langle L_{500} \rangle$ [B/s]	ΔE_{500} [B]	E_{exp} [B]	t_{exp} [s]	M_{ns} [M_{\odot}]	v_z^{ns} [km/s]	$v_z^{\text{ns},\nu}$ [km/s]	a_z^{ns} [km/s 2]	α_{gas}	d_{shock}
R10	24.7	59.6	0.09	59.9	48.8	0.25	0.418	1.521	-15.4	-14.3	-118.7	0.02	-0.02
R12	29.7	71.5	0.11	64.6	49.9	0.50	0.316	1.461	-235.8	17.5	-203.4	0.16	0.15
R14	34.6	83.4	0.13	69.2	52.4	0.69	0.264	1.420	88.4	14.6	86.9	0.04	0.15
R16	39.6	95.3	0.14	71.9	56.0	0.98	0.256	1.396	321.2	-8.9	210.1	0.11	0.06
R18	44.5	107.3	0.16	75.8	58.3	1.24	0.232	1.349	-4.8	-3.7	-26.7	0.00	-0.07
R18-g	44.5	107.3	0.16	75.8	58.5	1.23	0.226	1.352	-113.9	2.1	-188.1	0.03	0.07
R20	49.5	119.2	0.18	78.8	60.9	1.64	0.214	1.309	280.1	0.8	123.9	0.06	0.14

Table 5. Simulations based on the Woosley et al. (1988)/Bruenn (1993) post-bounce model. The luminosity time scale t_L is 1 s. For more details, see the caption of Table 1. Different from the models listed in all other tables, the recoil motion of the neutron star was accounted for in the simulations listed here (as described in Sect. 2.3).

Model	L_{ib} [B/s]	$\Delta E_{\nu,\text{core}}^{\text{tot}}$ [B]	$\Delta Y_{\text{e,core}}$	$\langle L_{500} \rangle$ [B/s]	ΔE_{500} [B]	E_{exp} [B]	t_{exp} [s]	M_{ns} [M_{\odot}]	v_z^{ns} [km/s]	$v_z^{\text{ns},\nu}$ [km/s]	a_z^{ns} [km/s 2]	α_{gas}	d_{shock}
B12-m1	29.7	71.5	0.11	60.9	47.4	0.36	0.226	1.384	-56.8	-1.7	-208.2	0.06	0.48
B12-m2	29.7	71.5	0.11	60.9	47.7	0.31	0.222	1.385	-100.0	19.1	-63.5	0.10	0.72
B12-m3	29.7	71.5	0.11	61.2	47.8	0.38	0.210	1.388	272.6	-16.5	91.9	0.23	0.35
B12-m4	29.7	71.5	0.11	60.9	47.0	0.35	0.209	1.378	-104.3	-7.4	-197.2	0.09	0.43
B12-m5	29.7	71.5	0.11	60.8	47.9	0.35	0.219	1.389	365.6	-10.1	219.1	0.32	0.47
B12-m6	29.7	71.5	0.11	60.7	48.4	0.36	0.229	1.395	-334.1	42.4	-462.9	0.30	0.26
B18-m1	44.5	107.3	0.16	68.9	54.9	1.12	0.136	1.274	43.3	-4.8	-108.8	0.02	0.12
B18-m2	44.5	107.3	0.16	68.9	54.8	1.14	0.139	1.273	-86.8	-1.1	-31.1	0.03	0.20
B18-m3	44.5	107.3	0.16	68.8	55.3	1.12	0.131	1.281	76.4	-8.8	-11.4	0.03	0.39
B18-m4	44.5	107.3	0.16	68.5	54.9	1.14	0.150	1.274	-118.7	14.5	-156.4	0.05	0.13
B18-m5	44.5	107.3	0.16	68.3	54.7	1.12	0.166	1.273	-339.7	-4.5	-152.4	0.13	-0.06
B18-m6	44.5	107.3	0.16	68.6	55.4	1.12	0.166	1.283	-439.3	14.0	-194.5	0.17	0.04
B18-m7	44.5	107.3	0.16	68.8	54.7	1.12	0.138	1.272	109.2	8.6	2.1	0.04	0.38
B18-m8	44.5	107.3	0.16	69.3	54.5	1.13	0.134	1.269	455.0	-4.1	187.4	0.17	0.05

to evaluate the gravitational energy, neglecting the relatively small general relativistic corrections, which have been taken into account in the simulations.

Another quantity of interest is the explosion time scale, t_{exp} , which we define as the time after the start of the simulation when E_{exp} exceeds 10^{48} erg. It turns out that the exact choice of this threshold value does not matter very much. Other definitions of the explosion time scale (e.g., linked to the time when the expansion velocity of the shock exceeds a certain value) do also not lead to qualitatively different results.

The neutron star mass and the neutron star radius are considered to be associated with a certain value of the density, $\rho_{\text{ns}} = 10^{11} \text{ g cm}^{-3}$. The neutron star radius, R_{ns} , is then simply defined as the radius where the lateral average of the density is equal to ρ_{ns} , and the baryonic mass of the neutron star, M_{ns} , is given by the sum of the central point mass and the mass integral over all grid zones with densities $\geq \rho_{\text{ns}}$. Since M_{ns} will in general vary with time due to accretion and mass stripping in the neutrino-driven wind, we also monitor the rate of mass

change, \dot{M}_{ns} , using finite differences in time. The sign of \dot{M}_{ns} is positive/negative when net accretion/ablation of matter occurs.

In evaluating the neutron star recoil velocity, \mathbf{v}_{ns} , we have to distinguish between simulations in which we consider the neutron star motion relative to the ejecta by changing the frame of reference after each time step (see Sect. 2.3), and simulations in which this motion is not accounted for. In the first case no post-processing is required, because the neutron star velocity is given at all times by the accumulated effects of the Galilei transformations applied until time t or time step n ,

$$\mathbf{v}_{\text{ns}}(t) = \sum_{m=1,\dots,n} \Delta \mathbf{v}_{\text{core}}^m. \quad (26)$$

In the second case, \mathbf{v}_{ns} is computed a posteriori, by making use of linear momentum conservation. The total momentum of the system, i.e. the sum of the neutron star momentum $\mathbf{P}_{\text{ns}} = M_{\text{ns}} \mathbf{v}_{\text{ns}}$ and the momentum of the surrounding gas on the computational grid, \mathbf{P}_{gas} , is initially zero (because all models that we consider are spherically symmetric or equatorially and axially symmetric just after collapse). Hence we have for all times

$$\mathbf{v}_{\text{ns}}(t) = -\mathbf{P}_{\text{gas}}(t)/M_{\text{ns}}(t), \quad (27)$$

and $\mathbf{v}_{\text{ns}}(t)$ can be determined by evaluating the neutron star mass and the momentum integral of the ejecta gas,

$$\mathbf{P}_{\text{gas}}(t) = \int_{R_{\text{ns}} < r < \infty} \rho \mathbf{v} \, dV. \quad (28)$$

Here $dV = r^2 \sin \theta \, dr \, d\theta \, d\phi$. Note that the volume integral in Eq. (28) is limited by the outer boundary of our Eulerian grid and that the momentum flux associated with anisotropic mass flow over the grid boundary would have to be taken into account.

Equation (27) may actually also be coined in terms of an anisotropy parameter of the ejecta, α_{gas} (see Janka & Müller 1994; Herant 1995). To accomplish this, we make use of the following scalar quantity

$$P_{\text{ej}}(t) := \int_{R_{\text{ns}}}^{R_s(\theta)} \rho |\mathbf{v}| \, dV, \quad (29)$$

which has the dimension of a momentum. Then we can write the anisotropy parameter as

$$\alpha_{\text{gas}} := |\mathbf{P}_{\text{gas}}| / P_{\text{ej}}, \quad (30)$$

and the absolute value of the neutron star velocity as

$$|\mathbf{v}_{\text{ns}}| = \alpha_{\text{gas}} P_{\text{ej}} / M_{\text{ns}}. \quad (31)$$

The neutron star acceleration corresponding to the velocity change at a given time is calculated by finite differences:

$$\mathbf{a}_{\text{ns}}^{(n)} = \frac{\mathbf{v}_{\text{ns}}^{(n+1)} - \mathbf{v}_{\text{ns}}^{(n-1)}}{t^{(n+1)} - t^{(n-1)}}. \quad (32)$$

In computing the recoil velocity according to Eqs. (27) and (31), we have so far neglected the fact that the neutron star may also be accelerated by anisotropic neutrino emission. While our core luminosities at the inner grid boundary are assumed to be

isotropic at all times and no neutron star acceleration can result from these, direction-dependent variations of the thermodynamic variables in layers close to the neutron star surface develop during the simulations and ultimately lead to anisotropies of the neutrinospheric emission of neutrinos. In particular, density inhomogeneities and local hot-spots (in temperature) occur as a consequence of narrow accretion flows that transport gas from the postshock layers to the neutron star, where they are decelerated in shocks and radiate away energy in neutrinos. The anisotropy of this neutrino emission can give rise to a “neutrino rocket effect”, whose magnitude can be estimated by considering the integrated momentum of the escaping neutrinos.

For a transport scheme along radial rays like ours, the neutrino momentum density has only a radial component and can thus be written as (see also Appendix A)

$$p_{\nu} \mathbf{e}_r = \frac{n_{\nu} \epsilon_{\nu}}{c} \mathbf{e}_r = \frac{F_{\nu}}{c^2} \mathbf{e}_r, \quad (33)$$

where F_{ν} is the local neutrino energy flux and \mathbf{e}_r the unit vector in the radial direction. The integrated neutrino momentum at time t is then given by

$$\begin{aligned} \mathbf{P}_{\nu}(t) &= \int_{R_{\text{ib}} < r < \infty} p_{\nu} \mathbf{e}_r \, dV \\ &= \int_{R_{\text{ib}} < r < R_{\text{ob}}} p_{\nu} \mathbf{e}_r \, dV + \int_0^t dt \oint_{r=R_{\text{ob}}} p_{\nu} c \mathbf{e}_r \, dS, \end{aligned} \quad (34)$$

with the surface element $dS = r^2 \sin \theta \, d\theta \, d\phi$. Here the surface integral accounts for the fact that a significant amount of neutrino momentum may have left our grid through the outer boundary by the time t . The momentum of the neutron star, including now also the effect of anisotropic neutrino emission, is

$$\mathbf{P}_{\text{ns}} = -(\mathbf{P}_{\text{gas}} + \mathbf{P}_{\nu}), \quad (35)$$

so that the neutron star velocity, corrected for the recoil by anisotropic neutrino emission, can be written as

$$\mathbf{v}_{\text{ns,corr}} = \mathbf{v}_{\text{ns}} + \mathbf{v}_{\text{ns},\nu} = -\mathbf{P}_{\text{gas}}/M_{\text{ns}} - \mathbf{P}_{\nu}/M_{\text{ns}}. \quad (36)$$

We finally note that for symmetry reasons \mathbf{P}_{gas} and \mathbf{P}_{ν} , and thus also \mathbf{P}_{ns} and \mathbf{v}_{ns} , can have only a component parallel to the symmetry axis, i.e. along the z -axis, in 2D axisymmetric calculations. Equation (28), for instance, therefore reduces to

$$\begin{aligned} P_{z,\text{gas}} &= 2\pi \int_{R_{\text{ns}}}^{\infty} dr \int_0^{\pi} d\theta r^2 \sin \theta p_z(r, \theta) \\ &= 2\pi \int_{R_{\text{ns}}}^{\infty} dr \int_0^{\pi/2} d\theta r^2 \sin \theta [p_z(r, \theta) + p_z(r, \pi - \theta)] \\ &= P_{z,\text{gas}}^N + P_{z,\text{gas}}^S. \end{aligned} \quad (37)$$

Here $p_z(r, \theta) = \rho (v_r \cos \theta - v_{\theta} \sin \theta)$ is the z -component of the momentum density of the gas, and $P_{z,\text{gas}}^N$ and $P_{z,\text{gas}}^S$ are introduced as the z -momenta of the gas in the northern and southern hemispheres, respectively.

To characterise the deviation of the shape of the supernova shock from a sphere we introduce a shock deformation parameter,

$$d_{\text{shock}} := \frac{\max(R_s(\theta) \cos \theta) - \min(R_s(\theta) \cos \theta)}{2 \times \max(R_s(\theta) \sin \theta)} - 1, \quad (38)$$

where $R_s(\theta)$ is the local shock radius as a function of polar angle θ . The numerator and denominator in Eq. (38) are the maximum shock diameters in projection on the symmetry axis and perpendicular to it, respectively. A prolate deformation leads to a positive value of d_{shock} , an oblate deformation gives a negative value. Note that a linear shift of the shock surface in the direction of the z -axis does not change d_{shock} .

3.3. Overview of the simulations

Tables 1–5 give an overview of the characterising quantities as defined in Sect. 3.2 for all simulations performed with our “standard boundary contraction”. The naming convention we have chosen for our models is the following: The first letter denotes the initial model (i.e. the progenitor/post-bounce data), followed by a two-digit code which corresponds to the chosen value for the total neutrino energy loss of the neutron star core, $\Delta E_{\nu,\text{core}}^\infty$, in units of $\frac{1}{100} M_\odot c^2$. Thus B18, for example, refers to a simulation based on the Woosley et al. (1988)/Bruenn (1993) initial data with an assumed release of gravitational binding energy of the core of $\Delta E_{\nu,\text{core}}^\infty = 0.18 M_\odot c^2$. The second fundamental model parameter, the luminosity time scale t_L , is not taken into account in the model names, because it has the same value for all models of a series. The chosen value in each case is given in the captions of Tables 1–5.

Simulations performed on a larger grid (with an outer boundary radius of 10^{10} cm and 500 radial zones) are indicated by the letter “g” appended to the model name, e.g. B18-g, simulations which account for the recoil motion of the neutron star contain the letter “m” in the model name, and model series started from different random seed perturbations are denoted by numbers appended to the model names. Hence Model B18-1 differs from Model B18 (and from Models B18-2, B18-3 etc.) only in the random perturbations imposed on the initial velocity distribution (with the perturbation amplitude being the same in all cases).

Note that in Tables 1–5 the time-dependent quantities $\Delta Y_{\nu,\text{core}}$, $\Delta E_{\nu,\text{core}}^{\text{tot}}$, ΔE_{500} , E_{exp} , M_{ns} , v_z^{ns} , $v_z^{\text{ns},y}$, a_z^{ns} , α_{gas} and d_{shock} are given at the time $t = 1$ s, at which we usually stop our simulations. We have to point out here that the listed neutron star recoils velocities, v_z^{ns} , are *not* the final ones, but that even at the end of our simulations the neutron star can still experience a large acceleration. We therefore also give the neutron star acceleration, $a_z^{\text{ns}} = dv_z^{\text{ns}}/dt$ (averaged over the last 100 ms and without neutrino effects), at the end of our simulations and will attempt to estimate final velocities of the neutron stars in Sect. 7.4.

The model parameters should be chosen (or should come out) such that basic constraints for the loss of energy and lepton number from the forming neutron star core are fulfilled. For example the lepton number loss during time t_L is in all cases of order 0.1–0.2, and the total (asymptotic) energy loss

$$\Delta E_{\text{core}}^\infty = 3 \times \Delta E_{\nu,\text{core}}^{\text{tot}}(t_L) \quad (39)$$

does not exceed the gravitational energy

$$E \approx 3 \times 10^{53} \left(\frac{M_{\text{ns}}}{M_\odot} \right)^2 \left(\frac{R_{\text{ns}}}{10 \text{ km}} \right)^{-1} \text{ ergs}, \quad (40)$$

which can be released during the birth of a neutron star. The energy ΔE_{500} radiated in ν_e and $\bar{\nu}_e$ is roughly consistent with the expected contribution of these neutrinos to the energy loss during the time interval t_L , i.e. $\Delta E_{500} \approx \frac{1}{3} \times \frac{1}{3} E$.

4. Two representative models

4.1. The character of the flow

Giving an accurate qualitative description of the flow that establishes in our calculations is a difficult endeavour, as the evolution that we observe during the first $\sim 300 - 400$ ms is wildly time-dependent and extremely non-linear. One may even characterise it as chaotic (see Sect. 4.5). The layer between the proto-neutron star and the supernova shock is Ledoux-unstable, because a negative entropy gradient is established due to neutrino heating within ~ 50 ms after bounce. Small Rayleigh-Taylor mushrooms grow from the imposed random seed perturbations and start rising towards the shock. They merge quickly and grow to fewer but larger bubbles that deform the shock and push it outward (Fig. 5). Initially, this deformation of the shock is confined to latitudes close to the poles, where the growth of the bubbles is faster than near the equator (cf. Sect. 4.3), but soon the entire shock surface is affected.

Due to the violent convective motions of the rising high-entropy plumes the shock gets bumpy and deformed, and caustic-like kinks of the shock emerge where two such bubbles approach each other and collide. Downstream of the shock, decelerated and compressed matter forms a high-density (low-entropy) shell, which sits atop high-entropy material that boils vigorously as it is heated by neutrinos from below. The interface between these layers is Rayleigh-Taylor unstable (Herant 1995) and gives therefore rise to narrow, low-entropy downflows of matter, which penetrate from the postshock layer to the neutron star with supersonic velocities. When they reach surroundings with entropies lower than their own, the downflows are decelerated and their material spreads around the neutron star. The evolution of these downflows is highly dynamic. They form, merge with other accretion funnels, or are blown away by the rising buoyant matter on a time scale of 10–20 ms, while their number decreases with time. The most massive of these downflows originate from the kinks at the shock surface, where the deceleration of the infalling matter is weaker due to the (local) obliqueness of the shock. During this phase of violent “boiling” the shock develops a strong, time-dependent deformation and expands slowly outward. In Model B12, whose evolution is shown in the sequence of plots on the left side of Fig. 5, pronounced bipolar hemispheric oscillations become visible after about 150 ms. This model differs from Model B18 (on the right side of Fig. 5) by lower neutrino luminosities at the inner boundary and a correspondingly lower explosion energy and later onset of the explosion. Model B18 shows also violent convective activity, but no such bipolar oscillations.

Owing to the persistent deposition of energy by neutrinos in the region between gain radius and shock, and the increase of the efficiency of the heating by convection, Models B12 and B18 ultimately explode at $t_{\text{exp}} = 220$ ms and $t_{\text{exp}} = 152$ ms, respectively, in contrast to one-dimensional counterparts of both

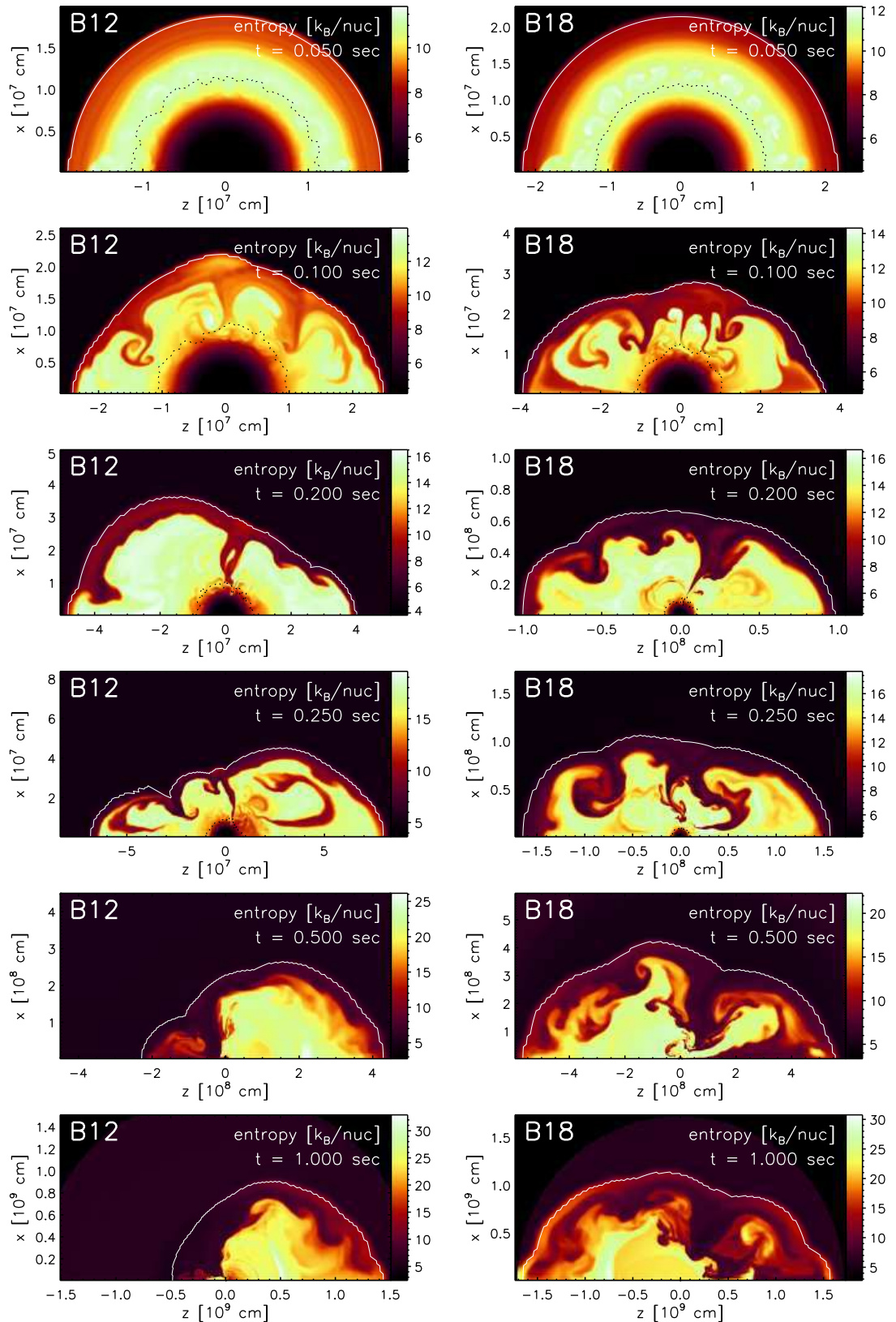


Fig. 5. Entropy distributions in Model B12 (left column) and Model B18 (right column) for different times. The figures are plotted such that the polar axis is oriented horizontally with “south” ($\theta = \pi$) on the left and “north” ($\theta = 0$) on the right. Dotted black lines mark the gain radius and white lines the supernova shock. Note that the scales differ between the plots. Convective activity starts with small Rayleigh-Taylor structures ($t = 50 \text{ ms}$) which then grow and merge to larger cells and global anisotropy. In contrast to Model B18, the low-energy model B12 develops pronounced bipolar oscillations (compare the plots for $t = 200 \text{ ms}$ and $t = 250 \text{ ms}$ between both cases). After the explosion has set in, the convective pattern “freezes out” and the expansion continues essentially self-similarly (see the plots for $t = 500 \text{ ms}$ and $t = 1000 \text{ ms}$).

models, which fail to explode. At these times the morphology is still evolving rapidly. About 100–200 ms later, however, the overall flow has settled into a quasi-self-similar state and has become remarkably stable (as predicted by Herant 1995), in stark contrast to the preceding phase. The boiling motions have given rise to only two bubbles, which show a Kelvin-Helmholtz unstable shear layer at their outer boundaries, and are separated by a single accretion funnel. The bubbles may occupy roughly a hemisphere each as in Model B18, but they may also differ significantly in size, resulting in a global $l = 1$ mode anisotropy as in Model B12 (see Fig. 5).

For sufficiently high core luminosities, accretion of matter onto the neutron star is eventually superseded by the onset of a neutrino-driven wind (see also Burrows et al. 1995; Janka & Müller 1996). If the wind is strong enough, as in Model B18 where the mass-loss rate of the nascent neutron star by the wind is $\dot{M}_{\text{ns}} = -5.1 \times 10^{-2} M_{\odot}/\text{s}$, it blows away the accretion funnel and establishes a high-entropy shell or cavity of rapidly expanding low-density material around the neutron star, which is separated from the ejecta by a strong reverse shock. Otherwise accretion through the funnel continues until more than about 1 s after bounce, as in Model B12. In this case the accreted material reaches infall velocities of about 1/4 of the speed of light, while the accretion rate at $t = 1$ s has decreased to $\dot{M}_{\text{accr}} \approx 4 \times 10^{-2} M_{\odot}/\text{s}$. Since at the same time the neutron star mass changes at a rate of $\dot{M}_{\text{ns}} \approx 1.1 \times 10^{-2} M_{\odot}/\text{s}$, only a fraction of $\sim 25\%$ of the infalling matter is actually integrated into the neutron star. The remaining 75% are heated and reejected with high velocity, inflating the buoyant bubble of neutrino-heated gas. The resulting flow, which is characterised by a strong dipole mode, can be conveyed only incompletely with plots such as Fig. 5 and is much more impressively captured by movies that we have produced from our data.

At the end of the simulations, Models B12 and B18 have attained explosion energies of 0.37×10^{51} erg and 1.16×10^{51} erg, respectively, which makes them representative of a low-energy and a rather high-energy (more standard) explosion.

4.2. Acceleration and recoil of the neutron star

We have shown in Sect. 3.2 that in a 2D axisymmetric calculation the neutron star recoil can only have a component parallel to the z -axis, and that for its calculation only the z -momenta of the gas in the northern and southern hemispheres need to be considered (see Eq. 37). If the momentum density of the ejecta, $p_z(r, \theta)$, is mirror symmetric with respect to the equatorial plane, i.e., if

$$p_z(r, \theta) = -p_z(r, \pi - \theta) \quad (41)$$

holds, the sum of the z -momenta of the two hemispheres vanishes

$$P_{z,\text{gas}} = P_{z,\text{gas}}^N + P_{z,\text{gas}}^S = 0, \quad (42)$$

and thus also the neutron star remains at rest (cf. Eqs. 37 and 27). The latter situation is given e.g. for an $l = 2$ mode, i.e. for two polar bubbles of equal size separated by a single downflow which is located in the equatorial plane. However, in general

Table 6. Integrated momenta of the ejecta in the northern ($\theta < \pi/2$) and southern hemispheres as well as their sum, $P_{z,\text{gas}}$, and the resulting neutron star recoil velocity, v_z^{ns} , at $t = 1$ s.

Model	$P_{z,\text{gas}}^N$ [$\frac{\text{g cm}}{\text{s}}$]	$P_{z,\text{gas}}^S$ [$\frac{\text{g cm}}{\text{s}}$]	$P_{z,\text{gas}}$ [$\frac{\text{g cm}}{\text{s}}$]	v_z^{ns} [$\frac{\text{km}}{\text{s}}$]
B12	1.26×10^{41}	-0.20×10^{41}	1.06×10^{41}	-389.3
B18	1.77×10^{41}	-3.07×10^{41}	-1.30×10^{41}	515.1

the expansion of the ejecta will proceed differently in the two hemispheres, so that a net momentum $P_{z,\text{gas}} \neq 0$ will result.

If a single downflow has formed, e.g., in the southern hemisphere, the expansion of the ejecta will be hampered there. On the other hand it will proceed unaffected in the northern hemisphere, and thus $|P_{z,\text{gas}}^N|$ will be larger than $|P_{z,\text{gas}}^S|$. Hence, $P_{z,\text{gas}}$ will be dominated by $P_{z,\text{gas}}^N$ (which is positive since all of the gas in this hemisphere is moving outwards). According to Eq. (27), the neutron star must then be accelerated in the negative z -direction, i.e. towards the (southern) hemisphere which contains the downflow. This is the situation that ultimately establishes in Model B12 (compare Fig. 5 and Table 6), and which is also illustrated in the right panel of Fig. 6. In this case the neutron star has attained a velocity of $v_z^{\text{ns}} = -389 \text{ km/s}$ one second after core bounce, and is still accelerated with $a_z^{\text{ns}} = -372 \text{ km/s}^2$ (Fig. 7).

Model B18 also develops a single downflow, which, however, is located in the northern hemisphere, rather close to the equator. Although this model is clearly less anisotropic than Model B12 (which is dominated by an $l = 1$ mode), the larger explosion energy and faster expansion result in a larger $|P_{z,\text{gas}}|$ (Table 6). This leads to a larger neutron star kick of $v_z^{\text{ns}} = 515 \text{ km/s}$ at $t = 1$ s, while the acceleration at this time is $a_z^{\text{ns}} = 290 \text{ km/s}^2$ (Fig. 7). Note that these values are comparable to the mean pulsar birth velocities derived from observations (see Sect. 7.4), and that they are considerably higher than those found in earlier simulations (e.g. Janka & Müller 1994). This is mainly due to the low-order modes in our calculations, which result in a larger anisotropy, α_{gas} , compared to previous work.

The neutron star velocities shown in Fig. 7 (left panel), as well as their time-derivatives labelled with “derivative” and plotted with solid lines in the acceleration plots of Fig. 7 (right panel), are calculated from the simulation data with our standard post-processing approach by assuming total momentum conservation (see Sect. 3.2). The use of this approach requires a justification, because momentum conservation may be numerically violated due to deficiencies of the solver for the gravity potential. Moreover, it can be guaranteed analytically and rigorously only if the gravitational potential can be written as the solution of a Poisson equation. This is, of course, the case for Newtonian gravity. Yet, for the “general relativistic potential” of Rampp & Janka (2002) that we used in the simulations, an equivalent of the Poisson equation cannot be derived (Marek et al. 2005).

We do not expect that the small general relativistic corrections can seriously affect the results of our post-processing to an extent that unrealistically large values for the neutron star recoil velocities are obtained, especially because we find sim-

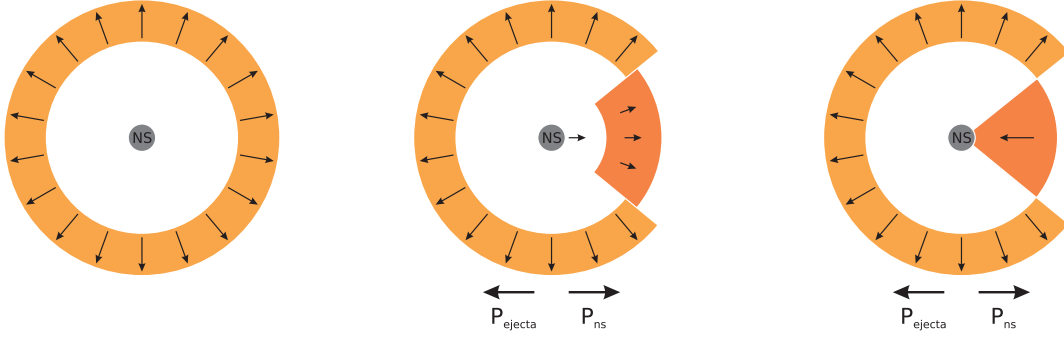


Fig. 6. Graphical illustration of the momentum balance between neutron star and ejecta. The largest fraction of the ejecta mass is concentrated in a dense shell behind the shock (bright coloured ring). For a spherical explosion (left panel) the momenta of the neutron star and the ejecta are zero. If the expansion of one hemisphere lags behind the other, the gas has a net momentum in the direction of the faster expanding hemisphere. The neutron star is always accelerated in the opposite direction, i.e. towards the slower moving gas (middle and right panels). This acceleration can be mediated by the gravitational attraction of the anisotropic ejecta (middle panel). In case accretion flows reach down to the neutron star surface (right panel), additional (hydrodynamic) forces may contribute, but the gravitational force, in general, remains dominant.

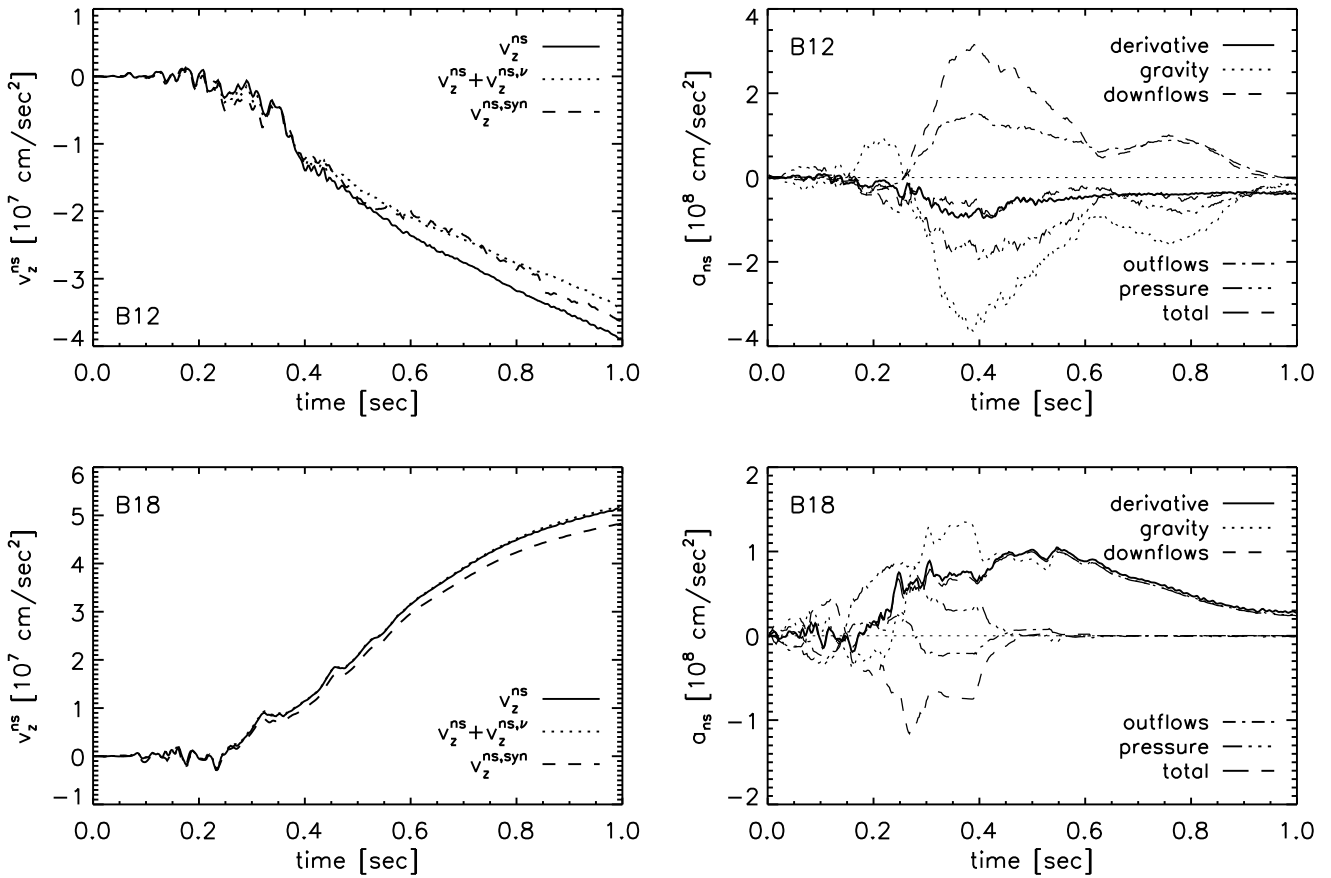


Fig. 7. *Left:* Evolution of the neutron star velocities for Models B12 and B18. The solid curve is the neutron star recoil velocity derived from total momentum conservation of gas and neutron star (see Eq. 27). The dotted curve includes corrections due to anisotropic neutrino emission. The dashed curve is an estimate obtained by integrating Eq. (43) over time. *Right:* Evolution of the neutron star acceleration (solid curve), as computed from the (numerical) time derivative of the solid curve shown in the velocity plots on the left side. Also shown are the individual terms of Eq. (43), corresponding to momentum transfer due to downflows, outflows (e.g. in the neutrino-driven wind), anisotropic pressure distribution around the neutron star, and gravitational pull of the anisotropic ejecta. The sum of these terms (the long-dashed curve labelled “total”) agrees well with the (solid) curve obtained independently from total momentum conservation applied to the hydrodynamics results.

ilarly large neutron star kicks in simulations with Newtonian gravity (see Sect. 7.3). Yet, to provide additional support that our standard post-processing method yields reliable results, we check it by calculating the neutron star acceleration as a sum of the different forces which contribute to the momentum transfer to the neutron star.

For this purpose we consider a sphere of radius $r_0 \approx 1.1R_{\text{ns}}$ that encloses the neutron star. The time-derivative of the neutron star momentum (and hence the neutron star acceleration at a certain time) can then be obtained by integrating the Euler equation over the volume of that sphere, resulting in

$$\dot{\mathbf{P}}_{\text{ns}} \approx - \oint_{r=r_0} \mathcal{P} \, d\mathbf{S} - \oint_{r=r_0} \rho \mathbf{v} \cdot \mathbf{v}_r \, d\mathbf{S} + \int_{r>r_0} GM_{\text{ns}} \frac{\mathbf{r}}{r^3} \, dm. \quad (43)$$

Here the individual terms account for the varying pressure \mathcal{P} around the sphere, the flux of momentum through the surface of the sphere, and the gravitational acceleration due to the anisotropic matter distribution outside the sphere. For the gravitational term we assume that the matter distribution inside the sphere is spherically symmetric and that the gravitational potential is *Newtonian*.

The time evolution of the acceleration corresponding to these terms, calculated from the data of Models B12 and B18, is shown in the right panels of Fig. 7. Here the second term has been split into two components associated with momentum flux into (“downflows”) and out of the sphere (“outflows”). Also displayed is the sum of all terms (labelled by “total”). Integration over time of the latter quantity yields the dashed velocity curve for $v_z^{\text{ns,syn}}$ in the left panels of Fig. 7. This should be compared to the solid curve (v_z^{ns}) which was computed with our standard post-processing approach of the gas momentum (and which includes the effects due to general relativistic corrections). It is evident that there are only small differences between both results, which are significantly smaller than 10%. This demonstrates that the use of relativistic corrections to the gravitational potential is not the cause of our high neutron star velocities.

An interesting implication of Fig. 7 is the fact that the largest contribution to the acceleration is, in general, due to the gravitational term. In certain evolutionary phases also the other terms may contribute significantly. Yet, the total acceleration points nearly always in the same direction as the gravitational pull. Momentum transfer by pressure and gas flow (the first and the second term in Eq. 43) are only important as long as the inhomogeneous ejecta have sonic contact with the neutron star and thus can exert hydrodynamic forces on the central object. This is the situation found in Model B18 for times before $t \approx 0.5$ s. After that time the supersonic neutrino-driven wind, which is very strong in this energetic model (due to the high neutrino luminosities) has blown away the accretion downflows from the neutron star. Ongoing acceleration is then exclusively caused by the gravitational pull of the anisotropic ejecta and decreases slowly as the nearly spherically symmetric wind clears the surroundings of the neutron star. Hydrodynamic forces therefore do not contribute at later times in Model B18. On the other hand, they are important at all times in Model B12. The acceleration due to the momentum flux associated with the

narrow downflows that reach the neutron star is usually the second most important term, and is directed opposite to the gravitational acceleration. Anisotropies in the pressure distribution and wind outflow contribute on a smaller level.

Finally, we show in Fig. 7 (left) with dotted lines the neutron star velocities corrected for the effects of anisotropic neutrino emission (see Sect. 3.2). These effects turn out to be small. For Model B12 the neutron star kick is thus reduced by about 10%, which is unusually large. For most of our models (including Model B18) the corrections due to anisotropic neutrino emission are smaller than 5% (see Sect. 7.1).

4.3. Possible origin of the low-order modes

The occurrence of a convective $l = 1$ mode in supernova explosions was already speculated about by Herant et al. (1992) and Herant (1995). Their suggestion was apparently motivated by Chandrasekhar’s finding that the easiest modes to excite in a thermally unstable flow between two spherical shells are those belonging to $l = 1$. The static situation discussed by Chandrasekhar (1961) requires that the inner shell radius is small compared to the outer one, so that convection can become “volume-filling”. Results of Woodward et al. (2003) and Kuhlen et al. (2003) show that the $l = 1$ mode indeed dominates in (full 4π) *three-dimensional* simulations of convection in red giant and non-rotating main sequence stars, respectively. Using linear stability analysis, Foglizzo et al. (2005) have recently shown that low modes can also dominate when the convectively unstable situation occurs in a neutrino-heated accretion flow behind a standing shock, a situation that corresponds more closely to the one developing in the SN core than the setup studied by Chandrasekhar (1961). The analysis revealed that for the lowest modes to be excited there, the growth rate of perturbations must exceed a certain threshold value. Even if the buoyancy forces are not strong enough, however, low-mode flow may be caused by other instabilities in the region between proto-neutron star and stalled shock. Blondin et al. (2003) discovered in 2D hydrodynamic simulations of adiabatic accretion flows that the standing shock is stable to radial perturbations and unstable to non-radial deformation with the $l = 1$ mode being the most unstable one. The instability was termed “standing accretion shock instability”, SASI, and was found to lead to a rapid increase of turbulence in the accretion layer and the development of large bipolar shock oscillations. Blondin & Mezzacappa (2005) explained this phenomenon by a growing standing pressure wave behind the deformed shock, which oscillates inside the cavity of the stalled shock with the speed of sound.

Yet another way to excite low-mode instabilities of accretion shocks was discussed as “advection-acoustic cycle” on the basis of linear analysis by Foglizzo (2001, 2002); Foglizzo & Galletti (2004) and Galletti & Foglizzo (2005). This instability relies on the fact that the infall of entropy and vorticity perturbations produces acoustic waves that propagate outward and create new entropy and vorticity perturbations when reaching the shock, thus closing an amplifying feedback cycle which eventually results in a dominant $l = 1$ or $l = 2$

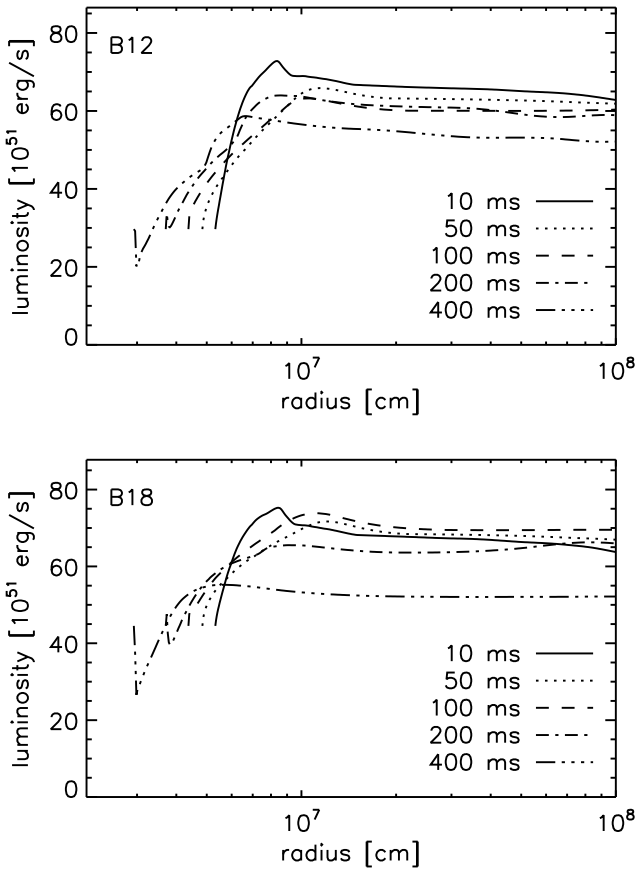


Fig. 8. Radial profiles of the sum of the ν_e and $\bar{\nu}_e$ luminosities for Models B12 and B18 at different times after the start of the simulations.

mode. This advective-acoustic cycle can even operate under conditions, in which convective instabilities are hampered, e.g. if the advection of matter out of the convectively unstable region is too fast to allow for a significant convective growth of small perturbations. Ohnishi et al. (2005) interpreted their 2D hydrodynamic simulations as a confirmation of the action of the advective-acoustic cycle at supernova core conditions, a conclusion which agrees with a detailed analysis of models similar to the ones presented in this paper by Scheck et al. (in preparation).

In all simulations discussed here, it is Ledoux convection which breaks the initial spherical symmetry. However, the advective-acoustic cycle may contribute in the later non-linear, chaotic phase. During this phase the two instabilities cannot be clearly disentangled any more. Yet, the bipolar oscillation (or “sloshing”) of the shock in low-energy models, like B12, has been found to be typical of $l = 1$ mode instabilities as associated with the advective-acoustic instability and the SASI. On the other hand, models with a moderately high explosion energy, like B18, do not show these pronounced oscillations. This fact might indicate that these models are dominated by the convective instability.

It should be noted that in the present paper we have constrained ourselves to 2D axisymmetric simulations, defer-

ring the three-dimensional case to a subsequent publication. It is well-known that the assumption of axisymmetry leads to smaller growth rates for equatorial, toroidal structures than for polar buoyant bubbles, and that both of these growth rates differ from those in a corresponding 3D calculation (see Kane et al. 2000). Furthermore, the use of reflecting boundary conditions in θ restricts the degrees of freedom of the flow. In addition, a coordinate singularity is present at the polar axis of a spherical grid. Therefore the question arises whether these shortcomings of axisymmetric calculations are causal for a preference of low-mode flows in two dimensions, whereas the true 3D situation might look different. This point was also raised by Blondin et al. (2003). The preliminary three-dimensional simulations that we have performed suggest that this is not the case. Low-order modes occur also in these simulations, and the evolution resembles qualitatively the two-dimensional case.

In previous 2D simulations Janka & Müller (1996) and Kifonidis et al. (2003) did *not* obtain the global anisotropies and low-mode flows that we discuss in the present paper. Instead, these models developed only small scale anisotropies, except for one model in Janka & Müller (1996), which exploded with a rather low energy and revealed the tendency towards an $l = 1$ asymmetry in the late post-bounce flow.

4.4. Comparison with other work

The fact that these earlier 2D simulations, which were performed with a neutrino light-bulb description, were not dominated by low-order modes, poses the question to which extent the development of such global asphericity in the flow is sensitive to the treatment of the neutrino transport. Figure 8 shows that our new neutrino transport description (which is presented in detail in Appendix A) yields radial profiles for the sum of the ν_e and $\bar{\nu}_e$ luminosities which deviate markedly from the radius-independent luminosities used in a light-bulb approach: The luminosities are significantly modified compared to the values imposed at the inner boundary. After some adjustment to the local thermodynamic conditions, which takes place in a few radial zones next to the inner boundary, the luminosities rise steeply in the cooling region below the gain radius, and decline slightly in the heating region farther out. The rise is caused by the creation of neutrinos when gravitational energy is released during the accretion and the contraction of the neutron star, while the slight decline results from the absorption of the ν_e and $\bar{\nu}_e$ in the heating region.

The “accretion” luminosity that is produced on the grid is usually of the same order as the luminosity emerging from the core. In low-energy models, like B12, the accretion component exceeds the core component early on, while in high-energy models the core component is dominant at all times (see the neutrino “lightcurves” for Models B12 and B18 shown in Fig. 9).

Yet, we point out here that all these (previously not modelled) effects are *not* the reason why the development of $l = 1, 2$ modes is seen here, whereas it was not visible in the calculations of Janka & Müller (1996) and Kifonidis et al. (2003). Highly anisotropic explosions can also be obtained with the

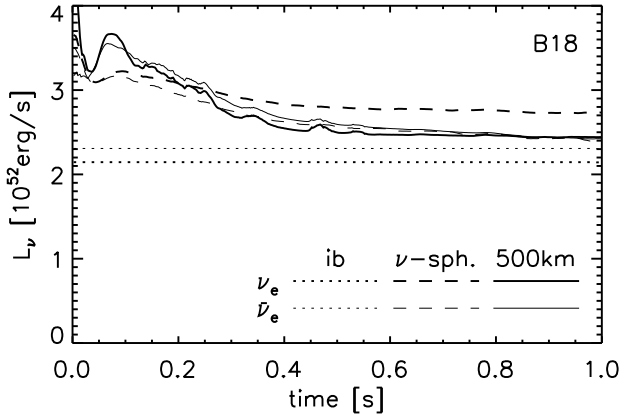
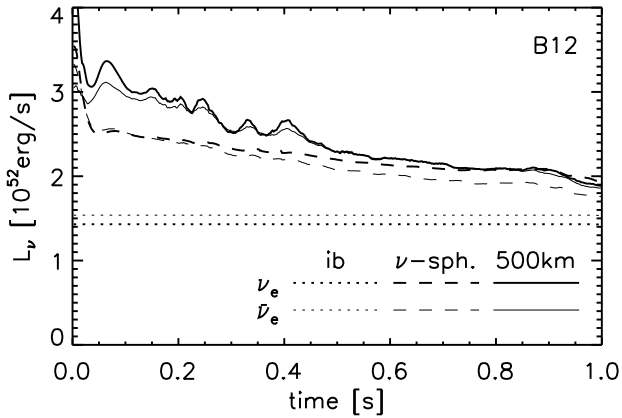


Fig. 9. Luminosities of ν_e and $\bar{\nu}_e$ at the inner boundary, at the ν_e -sphere, and at a radius of 500 km. Note the different importance of the accretion contribution to the luminosity in the low-energy explosion (Model B12) compared to the high-energy explosion (Model B18) and the rapid decay of the accretion luminosity after the onset of the explosion in the latter model.

light-bulb assumption (see Janka et al. 2003; Janka et al. 2004a for an example). In other words, the details of the functional form of $L(r)$, which are visible in Fig. 8, are *not* decisive for the growth of the $l = 1, 2$ modes. What is crucial, however, is that the explosions in the current models start *slowly*. This was not the case in all but one of the simulations of Janka & Müller (1996) and Kifonidis et al. (2003), where the neutrino luminosities were assumed to decay exponentially instead of varying slowly. The exponential, “burst-like” decline of the neutrino light bulb implied fairly high initial luminosities – which were required in case of the exponential decay for getting “typical” supernova explosion energies – and thus strong neutrino heating occurred at early times after bounce. This led to rapid explosions, which in turn did not leave enough time for the convective cells and bubbles to merge before the expansion became so fast that it continued in a quasi self-similar way. Since the convective bubbles are initially small, their early “freezing out” in the rapidly expanding flow had the effect that small structures (i.e. high-order modes) prevailed until very late times. The rapid explosions also caused a quick end of the accretion of the proto-neutron star, and therefore the neutron stars

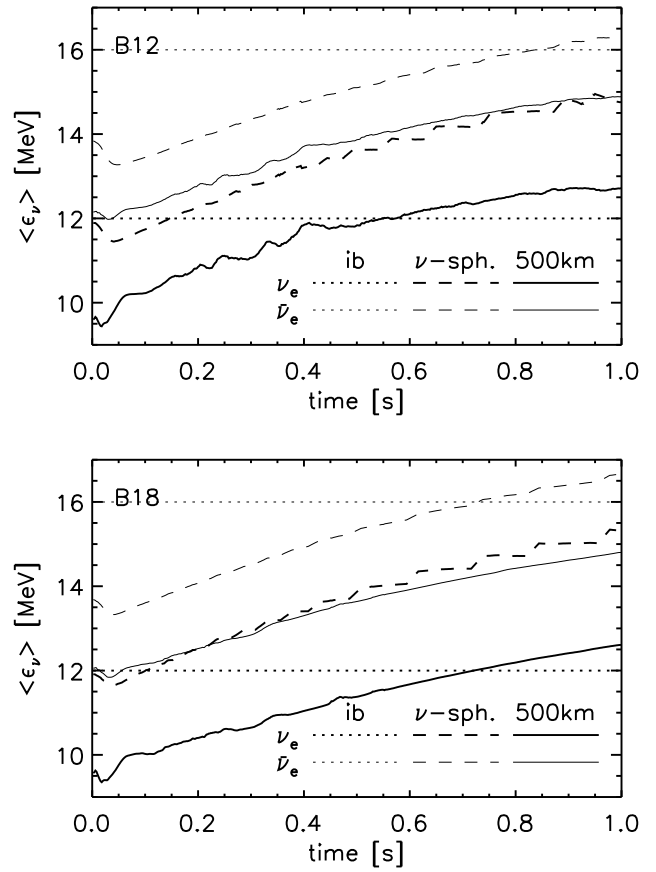


Fig. 10. Evolution of the mean ν_e and $\bar{\nu}_e$ energies at the inner boundary (ib), at the ν_e -sphere, and at a radius of 500 km. Note that due to the contraction and compressional heating of the nascent neutron star the average energies of the radiated neutrinos continue to rise until the end of our simulated evolution.

remained small. In contrast, the present transport description gives neutrino luminosities between the neutrino spheres and a radius of 500 km that vary much less steeply than exponentially with time (see Fig. 9). This leads to explosion time scales that are sufficiently long to allow for the formation of low-order convective modes.

A comparison with hydrodynamic supernova models which solve the Boltzmann equation for neutrino transport (e.g. Liebendörfer et al. 2001; Liebendörfer et al. 2005; Rampp & Janka 2000; Buras et al. 2003, 2005a,b; Thompson et al. 2003) shows that the approximative transport description of this work reproduces qualitatively well the temporal behaviour of the ν_e and $\bar{\nu}_e$ emission (luminosities, Fig. 9, and mean energies, Fig. 10) after core bounce found with the more accurate spectral transport solvers. Also the size of the neutrino luminosities and mean neutrino energies is in reasonably good agreement with the Boltzmann results. A more detailed comparison beyond the qualitative level, however, is not possible and in fact does not make much sense, because the approximations employed in the transport description of this work are manifold, e.g., the spectra are assumed to have Fermi-Dirac shape, the effective neutrino flux velocity is

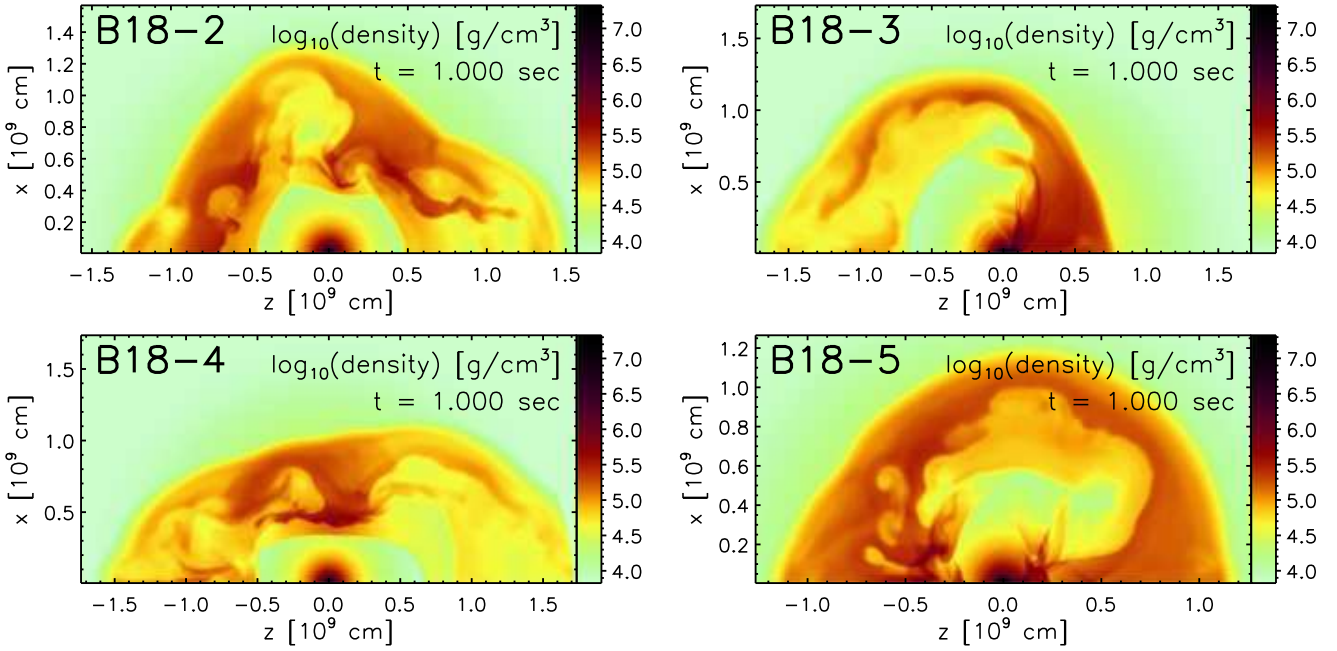


Fig. 11. Density distributions one second after core bounce for four simulations with the same initial and boundary conditions as Model B18, but different patterns of the random seed perturbations imposed on the velocity field of the initial model. The amplitudes of the perturbations (10^{-3}) are the same in all cases. The morphology of the explosion depends in a chaotic way on the initial perturbations.

parametrised, and the relativistic effects and $O(v/c)$ corrections in the transport are neglected. Therefore important differences in the neutrino-matter coupling must be expected. For these reasons one should not demand a quantitative reproduction of the behaviour of hydrodynamic models with Boltzmann transport when the luminosities at the inner boundary are adopted from the Boltzmann results at the corresponding Lagrangian mass coordinate.

Nevertheless, our transport scheme can account qualitatively well for the evolution of core and accretion components of the neutrino luminosities, for the radial and temporal evolution of the luminosities and mean energies of the radiated neutrinos, and for the relative sizes of the ν_e and $\bar{\nu}_e$ emission. We therefore think that our current transport treatment is a reasonably good method for performing parametric explosion studies with the aim to better understand the role of hydrodynamic instabilities during the shock-revival phase of neutrino-driven supernova explosions. This confidence is supported by comparisons of our models to Models s11.2 and s15r of Buras et al. (2003), and to the (flux-limited diffusion) 2D simulations of Burrows et al. (1995), who found similar shock “pulsations” and the same boiling of neutrino-heated matter that we see in our models. However, both groups used computational wedges of only 90° latitudinal width with periodic boundaries in θ -direction. In thus constrained simulations global $l = 1, 2$ modes cannot occur.

We believe that the use of small computational wedges was one of the major drawbacks of previous calculations (e.g. Herant et al. 1992; Burrows et al. 1995; Buras et al. 2003). It is likely that the occurrence of low-mode instabilities would have been observed if these simulations had been carried out with a

full 180° grid for a sufficiently long period of post-bounce evolution. Indeed Buras et al. (2005b) have recently recalculated their Model s11.2 on a 180° grid, and obtained a pronounced $l = 2$ mode with significant $l = 1$ contribution. Moreover, this model exploded whereas its 90° counterpart failed. Apparently, low-order convective modes can help or even trigger the supernova, if the neutrino luminosities are close to the threshold required for an explosion. This is in agreement with the results of our calculations and lends support to the idea that low-order convective modes, the explosion itself, and large neutron star kicks can go hand in hand. The 2D simulations of Fryer (1999) and Fryer & Heger (2000) as well as 3D simulations of Fryer & Warren (2002, 2004) are not in conflict with our findings, because their transport treatment leads to very rapid and powerful explosions in which case we usually also observe that the growth of $l = 1, 2$ mode instabilities is suppressed.

4.5. Sensitivity to the seed perturbations

The highly nonlinear character of the evolution that we see within the first ~ 300 ms suggests that the convective mode that will finally establish in a simulation, might be sensitive to the seed perturbation for triggering convection. To test this we repeat the calculations of some models with varied random seeds for the initial velocity perturbations. Figure 11 displays density plots at $t = 1$ s for the B18-series of models thus obtained. These differ from the original Model B18 (Fig. 5, right column) only in that they are computed with different seed values for the random number generator. The *amplitude* of the perturbations is kept the same (the effects of different perturbation amplitudes will be discussed in the second paper of this series;

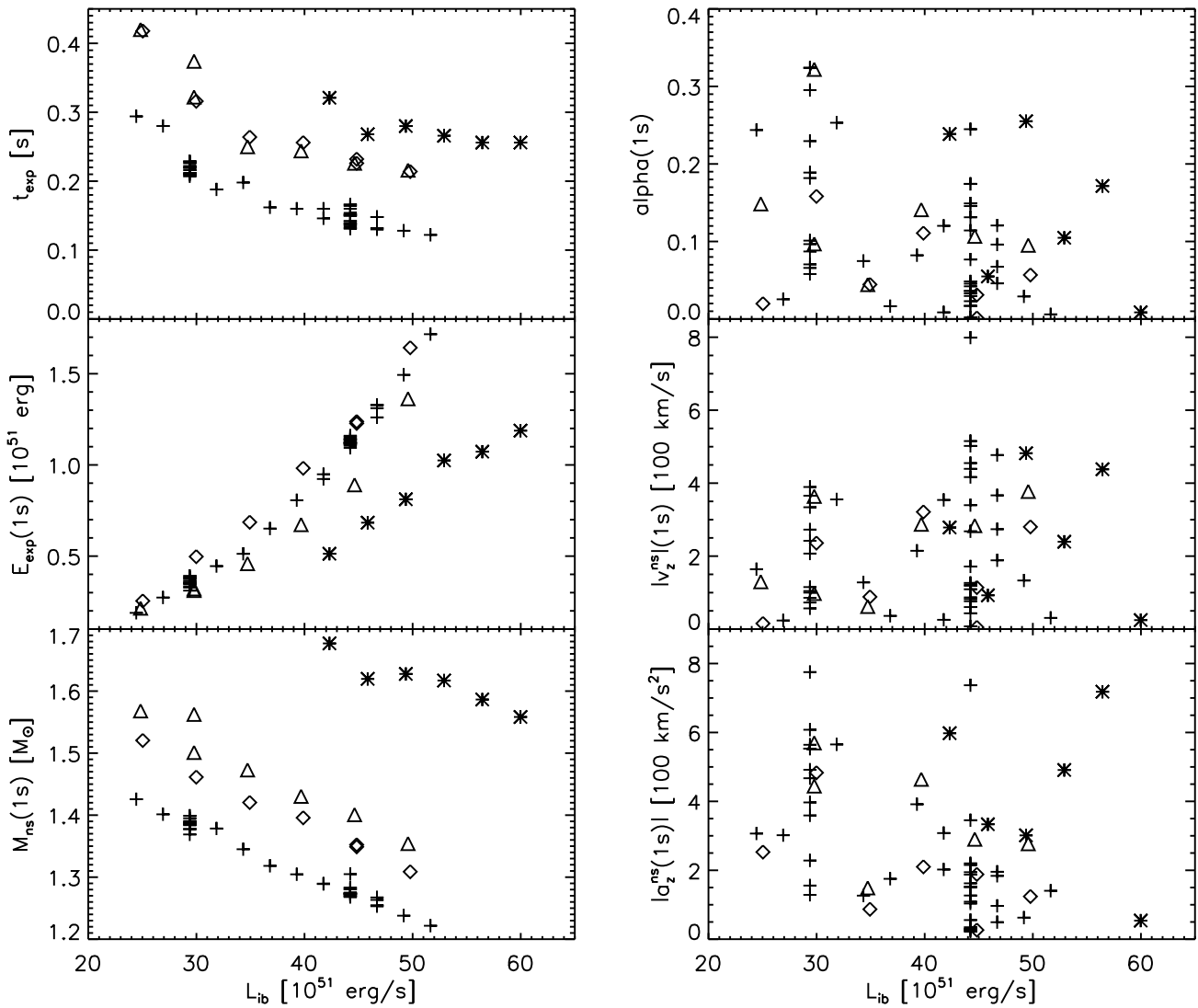


Fig. 12. Dependence of some global quantities on the inner boundary luminosity. The quantities in the left column (explosion time scale, explosion energy, and neutron star mass) depend only on the progenitor and the boundary conditions. The quantities in the right column (anisotropy, neutron star velocity, and acceleration) are strongly influenced by the initial perturbations. All time-dependent quantities are shown at $t = 1$ s. Crosses stand for the B-series of models, stars mark results for the L-series, triangles denote the W-series, and diamonds refer to the R-series of models (see Sect. 3.1 for the differences between these models).

but see also Sect. 5). The outcome supports our conjecture: A sensitive dependence of the late-time shock morphology and anisotropy of the explosion on the initial seed is visible. In fact this sensitivity is so extreme that the system may be described as exhibiting symmetry breaking in a chaotic manner. Even the same model computed on different machines (with supposedly IEEE compliant 64-bit arithmetics) may actually end up with a different morphology.

We emphasise here that integral quantities like the explosion energy, E_{exp} , the explosion time scale, t_{exp} , or the mean shock radius are only weakly affected by varying the random seed perturbations in the described way (see Tables 1–5 and Fig. 11). In contrast, quantities like the neutron star recoil velocity, v_z^{ns} , and the anisotropy parameter, α_{gas} , which depend on the morphology of the ejecta, are affected dramatically. Given

the extreme sensitivity on the initial perturbations, such quantities must be regarded as stochastic. Meaningful conclusions concerning their average values, the shape and width of their distribution functions, etc., can thus only be drawn on the basis of a large number of simulations. The large scatter of neutron star recoil velocities for Models B18-2 to B18-5 (see Table 1) illustrates this clearly. While the neutron star in Model B18-2 moves with only ~ 80 km/s, it is accelerated to 800 km/s in Model B18-3. This latter model is actually the most extreme one that we have found in our ~ 80 simulations. It features an $l = 1$ mode with a long-lasting downflow (Fig. 11), which, despite the relatively high core luminosity of this model, is still connected to the neutron star at times as late as $t = 1$ s after bounce. We also see that neither bipolar oscillations nor the

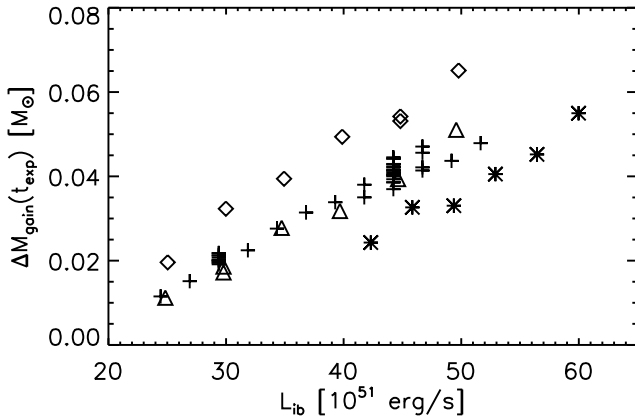


Fig. 13. Mass of the gain layer at the onset of the explosion (t_{exp}) as a function of the boundary luminosity for the set of models displayed in Fig. 12. For every initial model there exists an approximately linear relation between ΔM_{gain} and L_{ib} .

dominance of an $l = 1$ mode are excluded when the explosion energy is relatively large.

5. Dependence on the initial model and the core luminosity

In this section we discuss the variation of the quantities introduced in Sect. 3.2 as functions of the initial model and a systematic variation of the imposed core neutrino luminosity L_{ib} . Tables 1–5 give an overview. To facilitate their interpretation, we also display the most important quantities for all models as a function of L_{ib} graphically in Fig. 12.

The results plotted in that figure show that the neutrino-driven mechanism as computed in our models is able to account for different key observational aspects of supernovae and neutron stars simultaneously, provided that sufficient time is available for low-order convective modes to form. Typical supernova explosion energies of about 10^{51} erg, typical baryonic neutron star masses around $1.4 M_{\odot}$ (actually between 1.3 and $1.6 M_{\odot}$ depending on the progenitor) and high neutron star recoils (with a maximum of 800 km/s in Model B18-3 after 1 s of post-bounce evolution, see Table 1), are obtained at the same time.

What is also apparent is that the quantities displayed in Fig. 12 can be grouped in two classes, those which show a clear correlation with the core luminosity, L_{ib} , and those which do not. Among the former are the explosion time scale, t_{exp} , the explosion energy, E_{exp} , and the neutron star mass, M_{ns} . For a given initial model these quantities show a systematic variation with the boundary luminosity with only little scatter. Among the latter quantities are the ones that depend on the morphology of the explosion, i.e. the anisotropy parameter, α_{gas} , the neutron star recoil velocity, v_z^{ns} , and the neutron star acceleration, a_{ns} . These show the essentially stochastic behaviour in dependence of the seed perturbations as discussed in Sect. 4.5.

A higher luminosity, L_{ib} , from the neutron star core causes the explosion to develop faster, to become more energetic, and

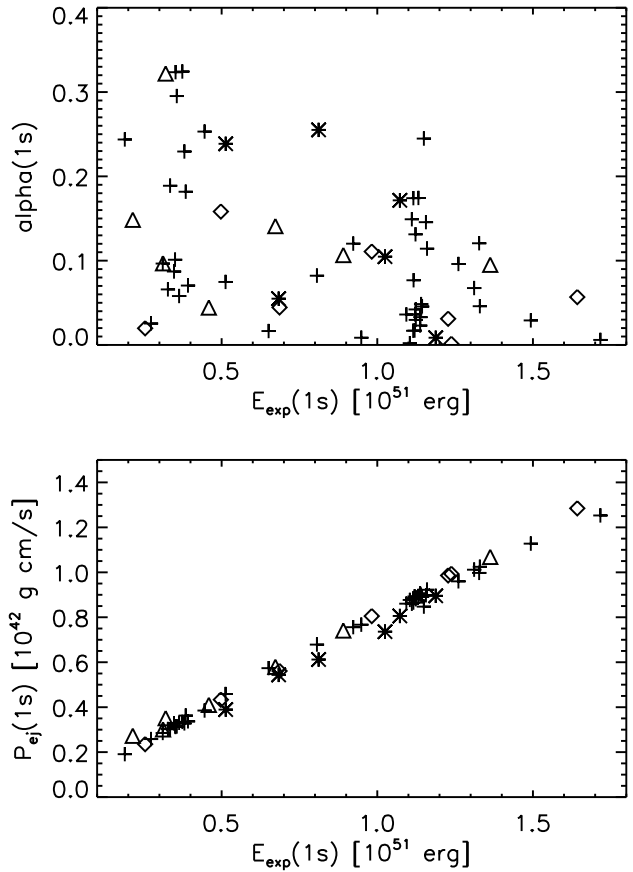


Fig. 14. Anisotropy parameter α_{gas} (upper panel) and (scalar) quasi-momentum of the ejecta, P_{ej} , (lower panel, see Eq. 29) for a time of 1 second after core bounce as a function of the explosion energy. The different symbols have the same meaning as in Fig. 12.

to leave behind a neutron star with a smaller mass, because less material can be accreted onto the core when the explosion occurs faster. The monotonic correlation between L_{ib} and the explosion energy E_{exp} shows that our chosen approach to parameterise our simulations can also be interpreted as one in terms of explosion energy. In this sense L_{ib} and E_{exp} can be exchanged as governing parameters. Note, however, that the $L_{\text{ib}}-E_{\text{exp}}$ relation differs between the initial models.

A similar behaviour is also visible in Fig. 13 for $\Delta M_{\text{gain}}(t_{\text{exp}})$, the mass contained in the gain layer at time t_{exp} , as a function of L_{ib} for all models. In fact, it is actually $\Delta M_{\text{gain}}(t_{\text{exp}})$ which is responsible for the progenitor dependence of the $L_{\text{ib}}-E_{\text{exp}}$ relation visible in Fig. 12, mainly because the recombination of free nucleons to α particles and nuclei in the expanding and cooling ejecta from the gain layer yields a significant fraction of the final explosion energy. This energy contribution increases with more mass in the gain layer. The rest of the explosion energy is due to the power of the neutrino-driven wind of the proto-neutron star (see Appendix C). Since $\Delta M_{\text{gain}}(t_{\text{exp}})$ depends on the mass accretion rate through the shock, there is a dependence on the density profile of the progenitor star. The different initial models reveal significant dif-

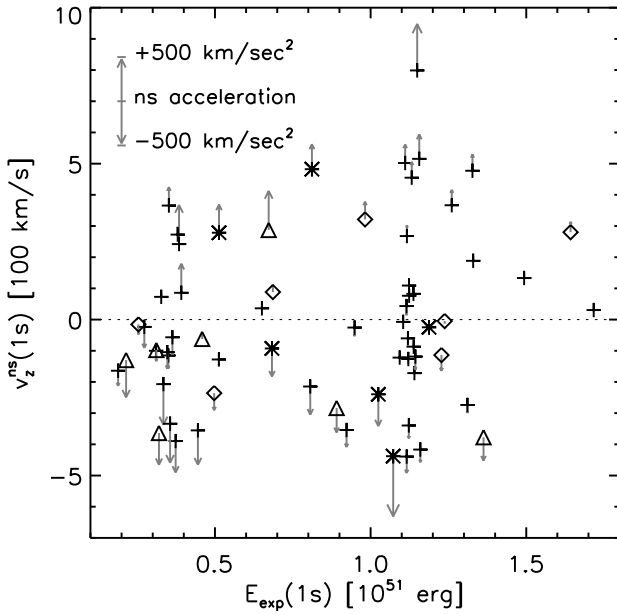


Fig. 15. Neutron star velocities v_z^{ns} and accelerations a_z^{ns} as functions of the explosion energy for all models of Tables 1–5. The plot displays the situation at $t = 1$ s and shows that the accelerations (indicated by the arrows) are still high at this time. The different symbols have the same meaning as in Fig. 12.

ferences in this respect. In particular, the Limongi et al. progenitor exhibits considerably higher densities at the edge of the iron core and in the silicon shell than the Woosley et al. models (Fig. 3), but this progenitor explodes later and thus at a time when the mass accretion rate has already decreased significantly.

It should be noted that rotation will also affect $\Delta M_{\text{gain}}(t_{\text{exp}})$ (see Sect. 6). The systematically larger mass of the gain layer (Fig. 13), and the up to $\sim 50\%$ higher explosion energies of the rotating models compared to the non-rotating models of the s15s7b2 progenitor (Fig. 12), though, are strongly affected by the larger initial perturbations that we have used in the rotating case (see Sects. 3.1 and 6).

A progenitor dependence is also visible in case of t_{exp} and M_{ns} as a function of L_{ib} , as displayed in the left column of Fig. 12. The simulations that are based on the newer $15 M_{\odot}$ progenitor model s15s7b2 of Woosley & Weaver (1995) give explosion time scales that are systematically higher by $\sim 30\%$, and final neutron star masses that are higher by $\sim 10\%$ than those of the older Woosley et al. (1988) core. On the other hand, the results belonging to the Limongi et al. (2000) progenitor again exhibit larger systematic deviations from those for the Woosley et al. stars. The higher mass accretion rate in simulations with the Limongi et al. progenitor delays the development of convective motions, and thus the onset of the explosion (t_{exp}) compared to the other models. This prolongs the time that the revived bounce-shock needs to reach a certain radius. It also reduces the explosion energy, and leads to a larger neutron star mass, for a given value of the boundary luminosity L_{ib} .

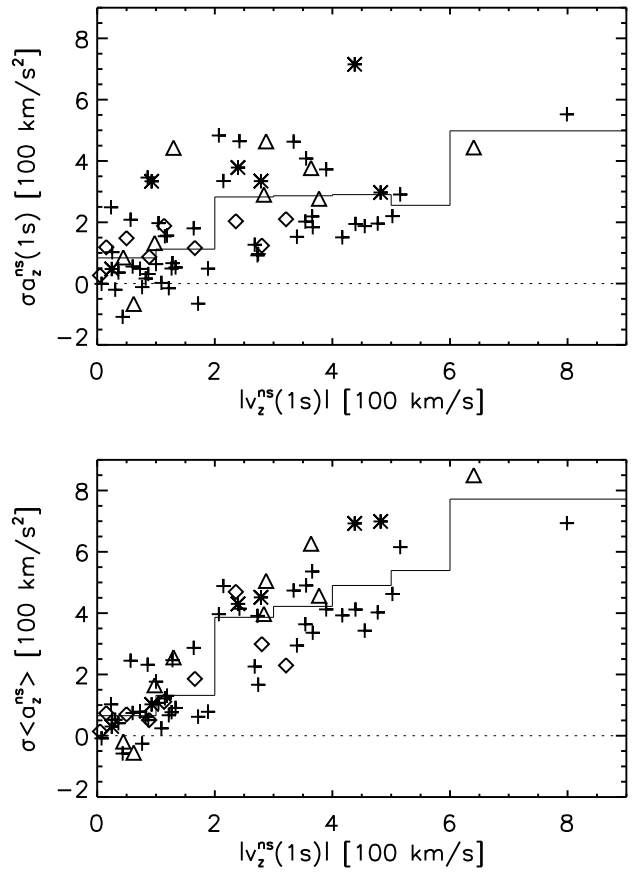


Fig. 16. *Top:* Neutron star acceleration as a function of the neutron star velocity after one second. *Bottom:* Acceleration computed as time-averaged value over the last half of a second of the simulations versus neutron star velocity. The acceleration is multiplied by a factor $\sigma = \text{sign}(v_z^{\text{ns}})$, i.e. $\sigma \langle a_z^{\text{ns}} \rangle < 0$ corresponds to a deceleration of the neutron star. The different symbols have the same meaning as in Fig. 12. Typically, low values of the acceleration ($\sigma \langle a_z^{\text{ns}} \rangle \lesssim 250 \text{ km/s}^2$) are associated with low velocities ($|v_z^{\text{ns}}| < 200 \text{ km/s}$), while much higher values of $\sigma \langle a_z^{\text{ns}} \rangle$ are reached for higher velocities $|v_z^{\text{ns}}|$. This suggests two components of the distribution, one with low velocities and lower average acceleration values and one with both values being higher. The thin solid line indicates the mean values of $\sigma \langle a_z^{\text{ns}} \rangle$, binned in velocity intervals of 100 km/s.

We focus now on the right column of Fig. 12. Recalling the highly nonlinear, chaotic hydrodynamic evolution in response to a variation of the initial perturbations as described in Sect. 4.5, one can understand that there is no clear correlation between L_{ib} and the quantities α_{gas} , v_z^{ns} , and a_z^{ns} , which depend on the explosion morphology. When, however, α_{gas} is plotted as a function of the explosion energy (see Fig. 14), it becomes apparent that the area near the upper right corner in the $\alpha_{\text{gas}}-E_{\text{exp}}$ diagram, satisfying

$$\alpha_{\text{gas}} / \alpha_0 + E_{\text{exp}} / E_{\text{exp},0} > 1 \quad (44)$$

with $E_{\text{exp},0} \approx 2 \times 10^{51} \text{ erg}$ and $\alpha_0 \approx 0.3$, is almost void. This indicates that high-energy explosions with large anisotropies are

disfavoured, which is plausible because there is not sufficient time available for high-order modes to merge. In order to assess the impact of this result on the neutron star recoil by virtue of Eq. (31), we need to consider also the scalar quantity P_{ej} , which is defined in Eq. (29). Figure 14 shows that it is linearly increasing with the explosion energy. Since $|v_z^{\text{ns}}| \propto \alpha_{\text{gas}} P_{\text{ej}}$, this increase of P_{ej} with E_{exp} will tend to compensate the smaller values of α_{gas} for higher explosion energies. Therefore high neutron star velocities (up to 800 km/s at $t = 1$ s) can result for a wide range of explosion energies (cf. Fig. 15). We expect, however, that for sufficiently large boundary luminosities the explosion time scale, and correspondingly α_{gas} , will become so small that the neutron star velocities will remain low for (very) large explosion energies.

Fig. 15 shows that also high acceleration rates (up to more than 700 km/s²) are obtained for the range of explosion energies covered by our simulations. In particular, the neutron stars that have already reached high velocities at $t = 1$ s have typically higher accelerations, too. This becomes somewhat more apparent in the panels of Fig. 16, which display the acceleration at the end of our simulations (top) or averaged over the last half of a second, respectively, as a function of the neutron star recoil velocity. One may discriminate two populations, a low-velocity, low-acceleration component in the lower left corner of the figure and a second component extending to much higher accelerations and velocities. The latter contains simulations with a strong contribution of the $l = 1$ mode, whereas the former is made up of models in which $l = 2$ or higher modes are dominant. Since in many of the simulations the accelerations are still high at $t = 1$ s, one can expect that their neutron star recoil velocities will significantly increase at still later times. We will discuss this in Sect. 7.4.

6. The effects of rotation

We have shown that the magnitude of the neutron star recoil depends sensitively on the convective mode. Here we will consider the influence of rotation, which can have an effect on the pattern of convection (see e.g., Tassoul 1978). In order to investigate how rotation changes the morphology, the energetics of the explosion, and the neutron star recoil velocities, we have computed the R-series of our models. These models start from a post-bounce configuration with a perturbation amplitude of several percent (cf. Sect. 3.1), which is more than an order of magnitude larger than the standard perturbations that we employed in our non-rotating models. Such a large increase of the perturbation amplitude leads to noticeable changes in the explosion time scale and energy. A clean discussion of rotationally induced effects therefore requires recomputing some of the non-rotating models with a higher amplitude of the initial random perturbations. We do this in case of Models W12-c and W18-c (see Table 7), in which the same initial perturbations are applied as in Models R12-c and R18-c, whose results are listed in Table 7, too.

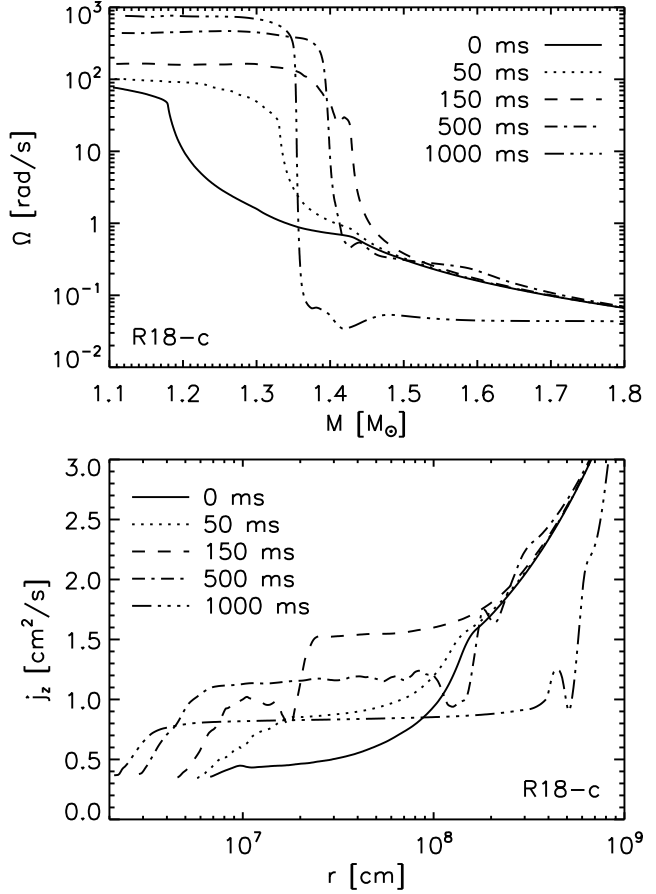


Fig. 17. Angular frequency, Ω , as a function of the enclosed mass, and radial profiles of the specific angular momentum, j_z , for several times after the start of the simulation for Model R18-c. In both cases the *equatorial* profiles of the quantities are shown. The “mass coordinate” is defined by the masses enclosed by spheres with different radii.

6.1. Evolution of the rotation rate

The initial rotation profile that we employ was already discussed in Sect. 3.1. Our choice of this angular velocity profile on the one hand maximises rotational effects in view of the most recent evolution calculations for magnetised rotating massive stars, it yields rotation rates that are more than a factor of two higher in the iron core, and on average a factor of ten higher in the silicon shell than in the calculations of Heger et al. (2004). On the other hand, it avoids sub-millisecond rotation of the newly formed neutron star, which would result for even higher pre-collapse rotation rates. Figure 17 shows that due to angular momentum conservation the contracting protoneutron star spins up to a maximum angular velocity of about 8×10^2 rad/s until one second after core bounce for the assumed contraction. This corresponds to a rotation period of several milliseconds.

6.2. Morphology

Figure 18 compares Model R18-c with its non-rotating counterpart W18-c. It is evident that during the first 75 ms after

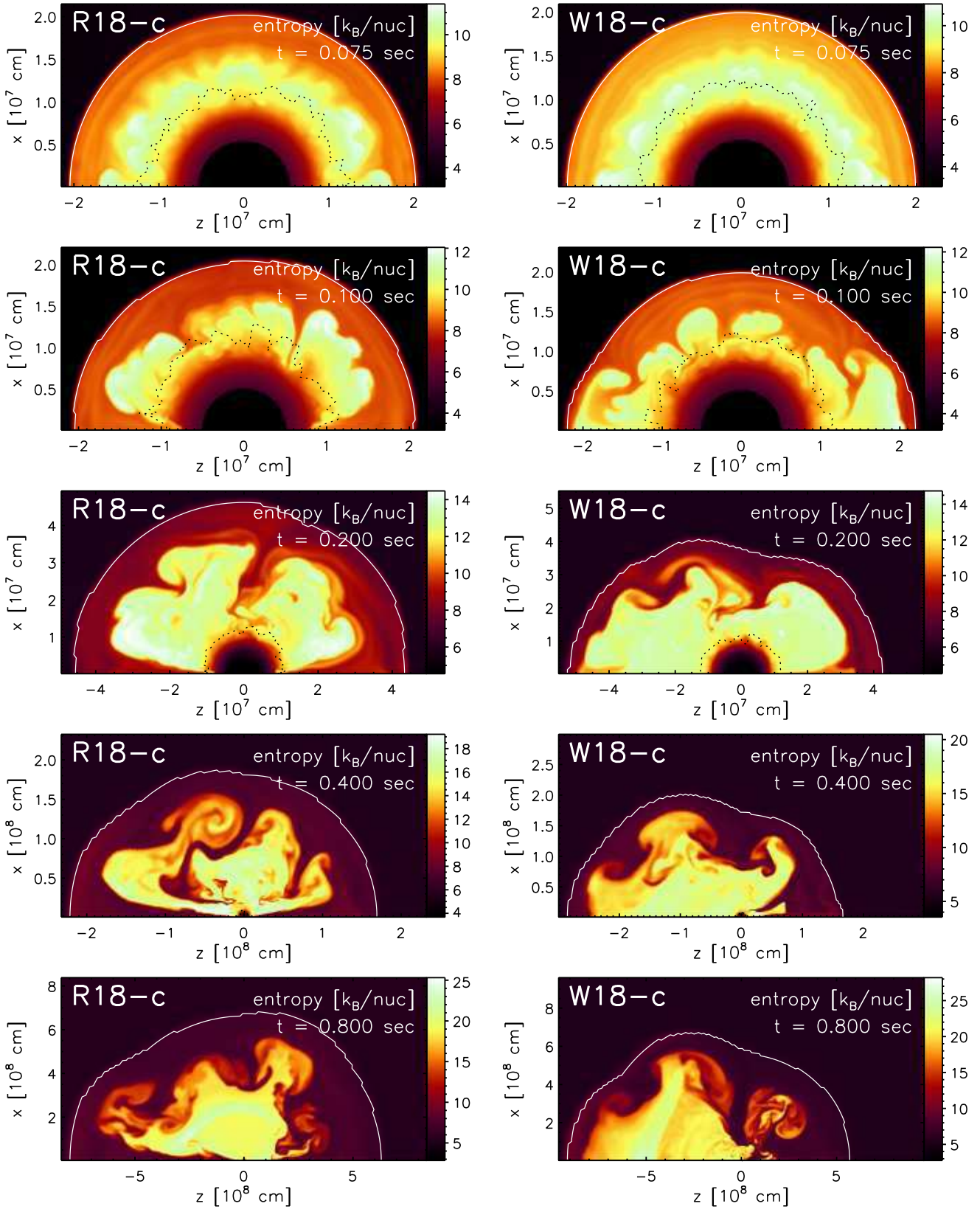


Fig. 18. Entropy distributions of the rotating Model R18-c (left) and of the non-rotating Model W18-c at 75 ms, 100 ms, 200 ms, 400 ms, and 800 ms after the start of the simulations. Dotted black lines mark the gain radius and white lines the supernova shock. Note the two polar downflows in the rotating model, which form soon after convection has set in, and are visible for $t \geq 100$ ms. At $t = 800$ ms they have been blown away from the vicinity of the neutron star by the neutrino-driven wind. The rotation axis is oriented horizontally in the left panels.

Table 7. Rotating and non-rotating models with the same initial perturbations. For more details, see the caption of Table 1.

Model	L_{ib} [B/s]	$\Delta E_{\nu, \text{core}}^{\text{tot}}$ [B]	$\Delta Y_{\text{e,core}}$	$\langle L_{500} \rangle$ [B/s]	ΔE_{500} [B]	E_{exp} [B]	t_{exp} [s]	M_{ns} [M_{\odot}]	v_z^{ns} [km/s]	$v_z^{\text{ns}, \nu}$ [km/s]	a_z^{ns} [km/s 2]	α_{gas}	d_{shock}
W12-c	29.7	71.5	0.11	68.7	57.1	0.40	0.301	1.535	44.4	54.0	85.4	0.03	0.63
W18-c	44.5	107.3	0.16	79.0	61.1	1.06	0.215	1.392	640.4	-8.5	444.4	0.21	0.08
R12-c	29.7	71.5	0.11	64.8	51.1	0.43	0.329	1.480	49.9	31.3	148.1	0.04	-0.03
R18-c	44.5	107.3	0.16	75.5	58.1	1.26	0.236	1.345	166.1	-3.5	116.2	0.04	0.05

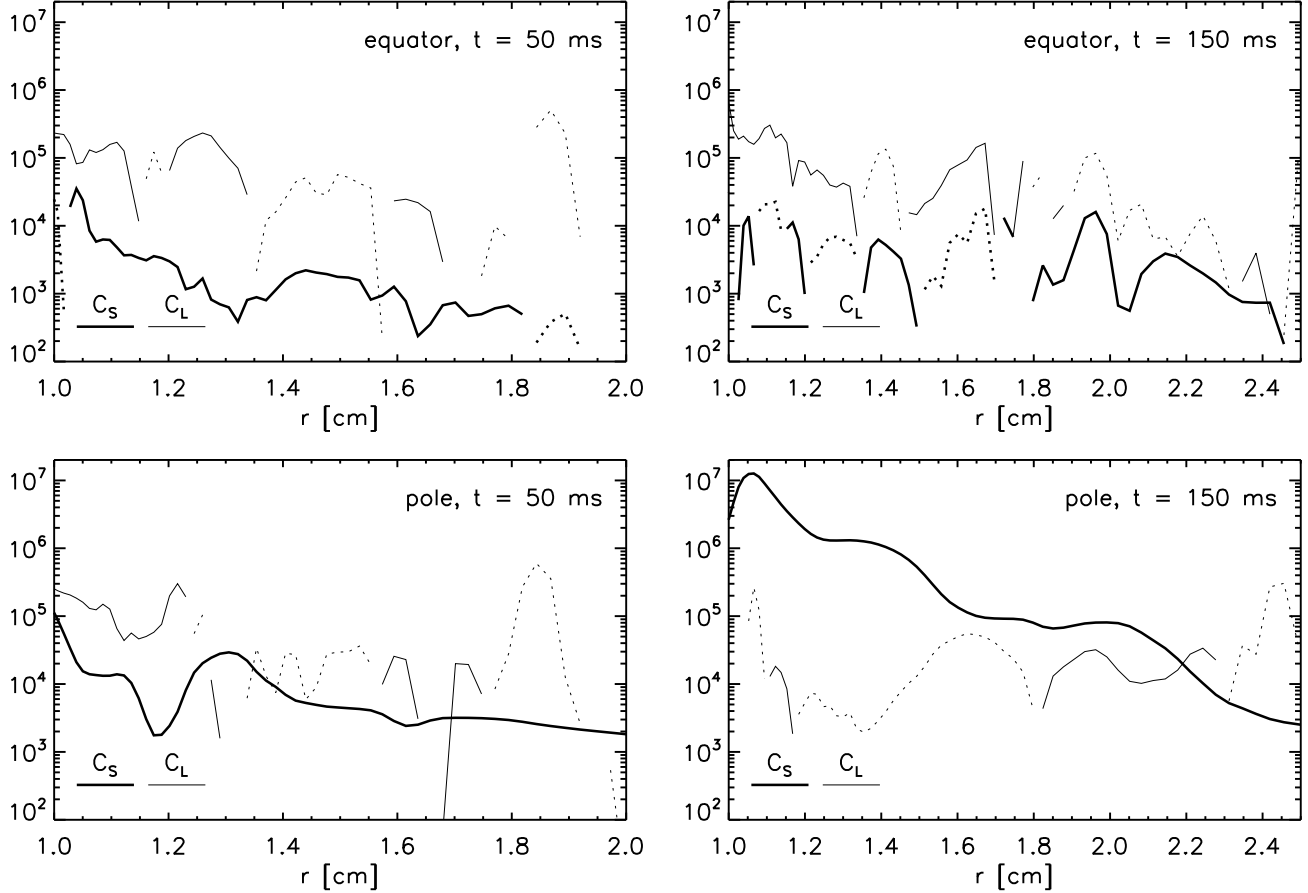


Fig. 20. Radial profiles of the Solberg-term, C_S , and of the Ledoux-term, C_L , (see Eq. 45) for $\theta = 5^\circ$ (“pole”) and $\theta = 90^\circ$ (“equator”) in Model R18-c. We show these quantities for $t = 50$ ms (left column) and $t = 150$ ms (right column). For regions in which C_S or C_L are negative, the absolute values are plotted as dotted lines. At $t = 50$ ms $|C_L| > |C_S|$ and unstable regions ($C_L + C_S < 0$) are present for both latitudes. At a time of 150 ms the gradient $d j_z^2 / dx$ has become sufficiently large to make $C_S > |C_L|$ at the pole, and thus to stabilise the flow, whereas in the equatorial region $|C_S|$ is still small.

the start of the calculations both models evolve quite similarly. Convection sets in between 100 and 150 km, and bubbles of high-entropy matter start rising above the gain radius. The number, wavelength, and location of the convective structures show hardly any differences between both models. This may appear somewhat surprising because the criteria for convective stability differ between the rotating and non-rotating cases. In the former case the flow is stable to convection only

if the Høiland condition,

$$C_H := C_S + C_L \quad (45)$$

$$= \frac{1}{x^3} \frac{d j_z^2}{dx} + \frac{1}{\rho} \mathbf{a} \cdot \left\{ \left(\frac{\partial \rho}{\partial S} \right)_{P,S} \nabla S + \left(\frac{\partial \rho}{\partial Y_e} \right)_{P,S} \nabla Y_e \right\} > 0,$$

is fulfilled (Tassoul 1978). Here \mathbf{a} is the total (gravitational and centrifugal) acceleration, and j_z is the specific angular momentum ($j_z = x \cdot v_\phi$, where $x = r \sin \theta$ is the distance from the axis of rotation). In the non-rotating case the condition of Eq. (45) reduces to the familiar Ledoux criterion for stability, $C_L > 0$, whereas for negligible entropy- and Y_e -gradients Eq. (45) becomes the Solberg-condition $C_S > 0$.

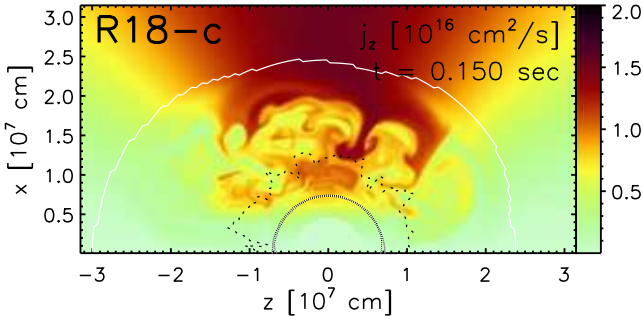


Fig. 19. Distribution of the specific angular momentum j_z of the rotating model R18-c at $t = 150$ ms. Matter with larger and larger specific angular momentum has fallen through the shock (outer solid line), which leads to an overall positive gradient $d j_z^2 / dx$ in the gain layer. However, due to convection, which is suppressed only near the poles, the j_z stratification and its gradient are locally perturbed. The rotation axis is oriented horizontally.

Both Models show a very similar evolution during the first 75 ms because the Solberg-term, C_S , is negligible in this phase. The total angular momentum and the derivative of j_z in the postshock region are initially rather small (see Fig. 17). However, the influence of the Solberg term increases with time because there is a positive gradient of j_z upstream of the shock, and matter with increasingly large specific angular momentum is advected into the postshock region. Therefore the positive derivative of this quantity with x grows within the postshock flow (Figs. 17 and 19). Note that, since we assume axisymmetry, there are no forces (other than fictitious ones) acting in ϕ direction, and hence no source terms for j_z are present. The specific angular momentum of a fluid element therefore remains constant, and j_z is simply carried along with the flow.

For $t > 75$ ms this causes the Solberg term to become sufficiently large so that it affects the pattern of convection. The latter exhibits differences now compared to the non-rotating case. All the rotating models develop downflows at both poles, whereas there is no preference for the formation of polar downflows in the non-rotating models (see Fig. 18). These polar downflows remain stable until they are blown away from the vicinity of the neutron star by the neutrino-driven wind (Fig. 18). The stabilisation is caused by the positive x -derivative of j_z^2 in the Solberg term, which is amplified by the factor $1/x^3$ near the axis of rotation. Given a positive derivative of j_z^2 , a matter element pushed towards the axis feels a larger centrifugal acceleration $a_c = j_z^2/x^3$ than the surrounding matter, and therefore moves back to its original position. Analogously, a fluid element pushed away from the axis feels a restoring force as well. Thus, perturbations perpendicular to the axis are suppressed and perturbations of a gas configuration in rotational equilibrium can only grow parallel to the axis of rotation.

For $t > 75$ ms this stabilising effect of the positive angular momentum derivative becomes sufficiently large to suppress convection near the axis of rotation, i.e. to make $C_H = C_S + C_L > 0$ there. In the rest of the postshock flow the Solberg

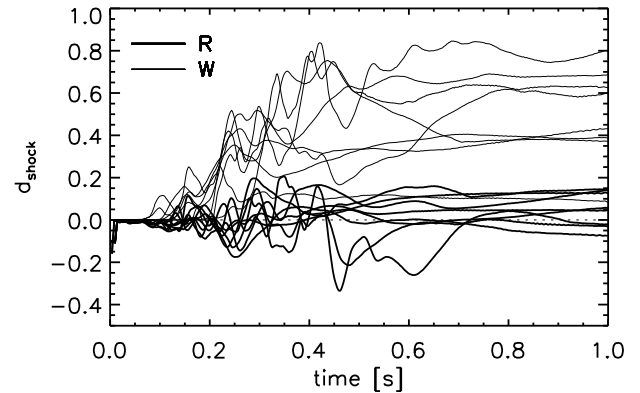


Fig. 21. Evolution of the shock deformation parameter d_{shock} (see Eq. 38) for the rotating (R-series) and the non-rotating models (W-series). Positive and negative values of d_{shock} characterise oblate and prolate deformation of the shock, respectively.

term is negligible (because of its dependence on x^{-3}) compared to the Ledoux term (i.e. $|C_S| \ll |C_L|$) and convection is not affected much. Radial profiles of C_S and C_L illustrating this situation are shown in Fig. 20.

The fact that only polar downflows and no polar outflows form can also be easily explained. Material inside a polar downflow always consists of the lowest j_z -gas which is advected through the shock (see Fig. 19). This guarantees a stable situation because the angular momentum derivative with x remains positive. In contrast, a polar outflow, i.e. a rising polar bubble, would contain postshock matter that would be rather well mixed, because a convective plume encompasses matter from a larger range of latitudes. Therefore such a polar bubble would not consist of gas with a lower j_z than the infalling material near the poles that surrounds such a bubble. This situation would therefore be unstable due to the absence of a positive derivative $d j_z^2 / dx$.

Besides the differences in the pattern of convection another morphological difference becomes evident: The rotating models remain more spherical, whereas the non-rotating models in general develop a clear prolate deformation (Fig. 21). This is partly due to the polar downflows, which damp the shock expansion near the poles. A second reason is the centrifugal acceleration of the matter between neutron star and shock. Owing to the accumulation of angular momentum behind the shock, the initially weak centrifugal forces increase, and their radial components reach up to 20% of the gravitational acceleration. Consequently the shock is pushed out farther in the equatorial region than in the non-rotating models. This has interesting consequences for the explosion energy.

6.3. Energetics

In both rotating Models R12-c and R18-c the explosion energies are higher and the neutron star masses are correspondingly lower than in the non-rotating counterparts of these models (Table 7). In case of models R18-c and W18-c the energy dif-

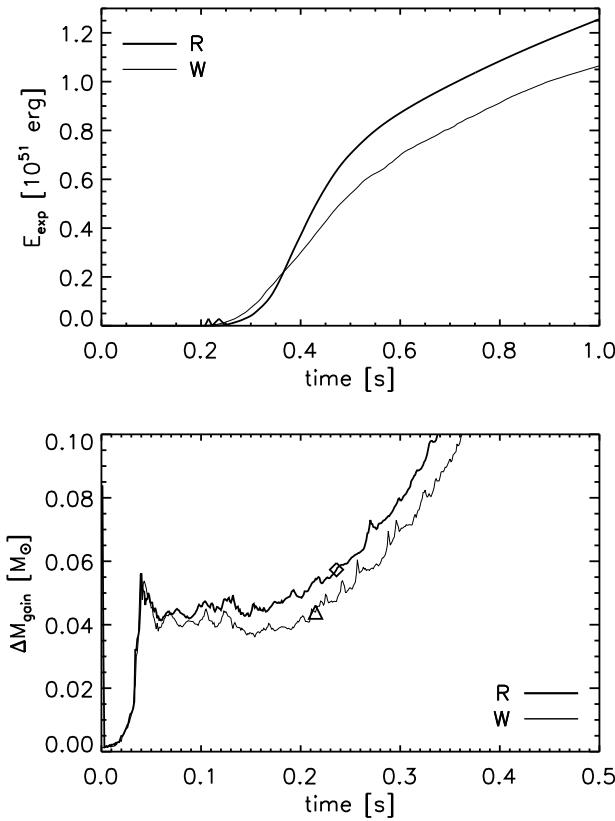


Fig. 22. Evolution of the explosion energy and of the mass in the gain layer for Models R18-c and W18-c. The symbols mark the onset of the explosion at $t = t_{\exp}$. The rotating model attains an explosion energy which is higher by 0.2×10^{51} erg than in the non-rotating model due to a mass in the gain layer that is larger by $0.013 M_{\odot}$.

ference amounts to $\sim 20\%$ (i.e. 0.2×10^{51} erg) and must be caused by rotational effects. This difference builds up when the expanding and cooling neutrino-heated matter in the gain layer recombines from free nucleons to alpha particles (and partly to nuclei) and remains approximately constant in the subsequent phase, in which the explosion energy increases further due to the neutrino-driven wind (see Fig. 22 and Appendix C). It is caused by the larger equatorial shock radius in the rotating model R18-c and the thus wider gain layer, which increases the recombining mass by $0.013 M_{\odot}$ compared to the non-rotating case.

6.4. Neutron star recoil

What are the implications of the morphological differences between rotating and non-rotating models for the neutron star kicks? In the non-rotating case we found that the highest recoil was obtained for Model B18-3, in which a pronounced $l = 1$ mode with a single polar downflow is present. In the rotating case such a flow pattern cannot establish, since we always obtain downflows at both poles. However, significant asymmetries can still develop, since one of the polar accretion funnels may be much stronger than the other, or a third

downflow may be dominating the mass distribution. High neutron star recoils are thus not precluded, although we expect the mean and the maximum kicks to be somewhat smaller than in the non-rotating case.

The results of our rather few simulations, which comprise only nine rotating models (see Tables 4 and 7), are in agreement with this expectation: The largest neutron star recoil velocity obtained in the R-series of models is 321 km/s, whereas it is 640 km/s in case of the W-series (see Model W18-c in Table 7). The average kick velocities for the R- and W-type models are 151 km/s, and 280 km/s, respectively. If one omits Model W18-c, the only W-type model with a “pure $l = 1$ mode”, the average kick velocity of the non-rotating models decreases to only 228 km/s, i.e. it is 50% larger than that of the rotating models. This is a relatively moderate effect if one recalls that the initial angular velocity assumed in the progenitor core of our calculations is clearly extreme compared to the rotation rates obtained from the latest stellar evolution calculations (Heger et al. 2004).

6.5. Spin-kick alignment?

Does rotation lead to an alignment of the kick direction with the rotation axis (the so called “spin-kick alignment”)? This question cannot be conclusively answered on the basis of two-dimensional axisymmetric simulations, because in this case the neutron star kick is always along the rotation axis due to the assumed symmetry of the calculations.

However in the context of our kick scenario also in the three-dimensional case effects can be imagined which may lead to a spin-kick alignment. On the one hand, the rotation axis is a preferred physical direction of the system such that the development of global anisotropies (e.g. polar accretion and outflow, bipolar oscillations) might be favoured along this direction. On the other hand, if the rotation period is smaller than the duration of the neutron star kick by a one-sided, non-axial acceleration (in the corotating frame), then any asymmetry will retain only its component parallel to the spin axis, while the perpendicular component will be reduced or extinguished by rotational averaging.

Our results seem to suggest that the first effect may be the more important one. For the angular momentum present in our models there is a tendency of anisotropies (e.g. of downflows) to develop preferably aligned with the rotation axis. While for the relatively “fast” rotation of our models (in the sense discussed in Sects. 3.1 and 6.1), the second effect may also contribute to produce spin-kick alignment, the influence of rotational averaging will be weaker for slower and possibly more realistic rotation. In case of “slow” rotation, i.e. for spin periods of tens of milliseconds in the nascent neutron star and many hundreds of milliseconds in the neutrino-heated convective postshock layer (which are ten times or more larger than in our models), rotation will be unable to enforce perfect alignment of the directions of kick and spin.

Depending on the amount of angular momentum in the supernova core, the hydrodynamical kick mechanism discussed in this paper therefore allows for both possibilities, spin-kick

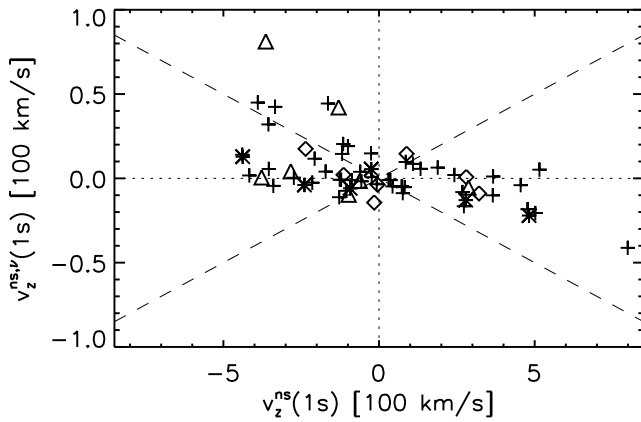


Fig. 23. Estimated velocity correction due to anisotropic neutrino emission, $v_z^{ns,\nu}$, as a function of the neutron star velocity v_z^{ns} caused by the anisotropies in the gas ejecta. The dashed lines correspond to a ratio $|v_z^{ns,\nu}/v_z^{ns}|$ of 10%.

alignment for rapid neutron star rotation ($t_{ns} \ll 1$ s) and misalignment or incomplete alignment for long rotation periods ($t_{ns} \gtrsim$ some 100 ms). This seems to be compatible with recent studies of observational constraints on neutron star kicks for isolated pulsars and for neutron stars in binary systems (Wang et al. 2005), although the interpretation of observations is still ambiguous (Johnston et al. 2005).

7. Robustness and long-time evolution of the neutron star recoils

We have seen above that rotation, even if it is noticeably faster than in the most recent stellar evolution models, does not preclude neutron star kicks of several hundred km/s. However, we have made a number of approximations in our post-processing analysis and used assumptions in our simulations whose impact on the neutron star recoil still needs to be assessed. In addition, we have stopped most of our simulations at a time of one second after core bounce, when the neutron star acceleration was, in many cases, still high. Hence we need to comment also on the later evolution of the kicks. These issues are discussed in the following.

7.1. Anisotropic neutrino emission

The neutron star recoil velocities, v_z^{ns} , that are listed in Tables 1–5 are computed from Eq. (27), i.e. they do not include the effects of anisotropic neutrino emission. As we have shown in Sect. 3.2, anisotropic neutrino emission results in a correction, $v_z^{ns,\nu}$, of the neutron star velocity which is described by Eqs. (34) and (36). In Sect. 4 we have already seen that this correction is small for Models B12 and B18. In Fig. 23 we now display $v_z^{ns,\nu}$ as a function of the neutron star velocity v_z^{ns} for all models of Tables 1–5. It is obvious that for most models $v_z^{ns,\nu}$ is only a small fraction of the velocity which the neutron star obtains due to anisotropies in the gas ejecta. Only in some cases is $|v_z^{ns,\nu}/v_z^{ns}| > 10\%$, and in most of these cases the neutron

stars have small recoil velocities. Note that the correction due to anisotropic neutrino emission in general reduces the kick. This can be understood from the fact that in most models a single prominent accretion funnel is present. The neutron star recoil caused by gas anisotropies is always directed towards this downflow, while the neutrino emission associated with the “hot-spot” created by the downflow on the neutron star surface results in a “neutrino-rocket engine” that kicks the neutron star in the opposite direction.

7.2. Inertial mass of the neutron star

In most of our simulations we make the simplifying assumption that the inertial mass of the neutron star is infinite, i.e. the consequences of the neutron star motion are ignored during the hydrodynamic simulation. This assumption is dropped in one set of models which is listed in Table 5. In these simulations the feedback effect of the neutron star motion is taken into account by changing the frame of reference in every time step, thus allowing the ejecta to move relative to the neutron star instead of following the neutron star motion through the ambient gas (see Sects. 2.3 and 3.2 and Appendix B).

In Fig. 24 results obtained from this approach are compared with corresponding simulations in which the neutron star is assumed to have infinite inertial mass. The neutron star velocities are displayed versus explosion energies for a bunch of low-energy and a number of high-energy models computed with the boundary parameters of Models B12 and B18, respectively. Each group contains simulations with and without “neutron star motion” (labelled as “moving” and “fixed”, respectively, in Fig. 24). The distribution of data points is very similar for both sets of simulations in both the high- and low-energy groups. A single model with $v_z^{ns} \approx 800$ km/s sticks out, but represents the rather rare cases where neutron star velocities higher than about 500 km/s are reached after one second. Usually a larger set of computations is needed to get statistically significant results for these extreme velocities.

7.3. Neutron star contraction and gravitational potential

For practical reasons, all simulations listed in Tables 1–5 and Table 7 were performed with our “standard” prescription for the contraction of the neutron star core (see Sect. 2.4.1), although the “rapid contraction case” also discussed in Sect. 2.4.1 might be more realistic. To study the corresponding differences, we take the “high-perturbation”, non-rotating Model W12-c (see Sect. 6 and Table 7) as a reference case and perform an additional simulation, Model W12F-c, in which we replace the slowly contracting inner boundary of Model W12-c with the prescription for a rapidly contracting proto-neutron star. Table 8 compares some quantities characterising the two models.

Model W12F-c explodes earlier and attains a higher explosion energy than Model W12-c. This can be explained by the facts that for a smaller inner boundary radius more gravitational energy is released, and that for a shorter contraction

Table 8. Important parameters of models W12-c and W12F-c.

Model	L_{ib} [B/s]	$\Delta E_{\nu,\text{core}}^{\text{tot}}$ [B]	$\Delta Y_{\text{e,core}}$	$\langle L_{500} \rangle$ [B/s]	ΔE_{500} [B]	E_{exp} [B]	t_{exp} [s]	M_{ns} [M_{\odot}]	v_z^{ns} [km/s]	$v_z^{\text{ns},v}$ [km/s]	a_z^{ns} [km/s 2]	α_{gas}	d_{shock}
W12-c	29.7	71.5	0.11	68.7	57.1	0.40	0.301	1.535	44.4	54.0	85.4	0.03	0.63
W12F-c	29.7	101.2	0.08	110.9	62.0	0.94	0.118	1.411	611.7	-1.9	580.6	0.21	0.31

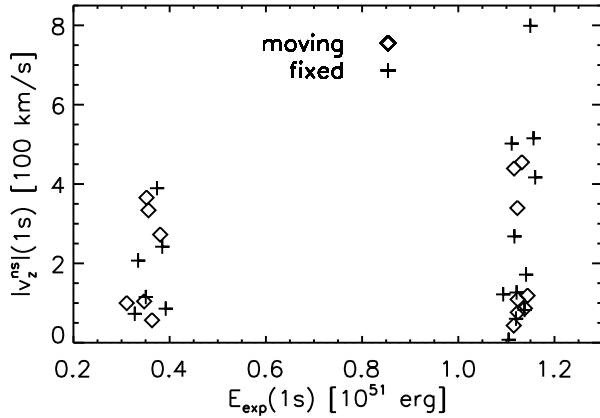


Fig. 24. Neutron star velocity as a function of the explosion energy for simulations with “fixed” (i.e. infinite inertial mass) and “moving” (i.e. finite inertial mass) neutron stars. All models of the left/right group have the same boundary luminosity as Model B12/B18, respectively.

time scale this release occurs earlier (see also Appendix C). With $v_z^{\text{ns}}(1 \text{ s}) = 611 \text{ km/s}$ the neutron star recoil velocity of Model W12F-c is very high. Large kicks are also found in a set of simulations performed with rapid boundary contraction in combination with

1. smaller initial random velocity perturbations of 0.1% (Model W12F in Fig. 25),
2. Newtonian gravitational potential and a constant central point mass chosen such that the same initial gravitational acceleration is obtained at a mass coordinate of $1.1 M_{\odot}$ as in the models of Buras et al. (2003), see Models W12F-n0, W12F-n1 and W12F-n2 in Fig. 25,
3. a Newtonian gravitational potential and a varying central point mass, which is increased with time to reproduce the evolution of the gravitational acceleration at a mass coordinate of $1.1 M_{\odot}$ in the models of Buras et al. (2003), see Models W12F-nv, W12F-nv1 and W12F-nv2 in Fig. 25.

All of these models have in common that they explode more quickly than models with the standard boundary contraction. Yet, for all of these variations we obtain at least one simulation with a neutron star recoil velocity of more than 400 km/s at $t = 1 \text{ s}$ (see Fig. 25). This demonstrates that a faster neutron star contraction does not preclude high neutron star kicks and in particular it shows that it is *not the absolute value of the time scale* for the onset of the explosion which matters. What matters is the time delay until the start of rapid expansion *relative* to the growth time scale of low-mode anisotropies by hydro-

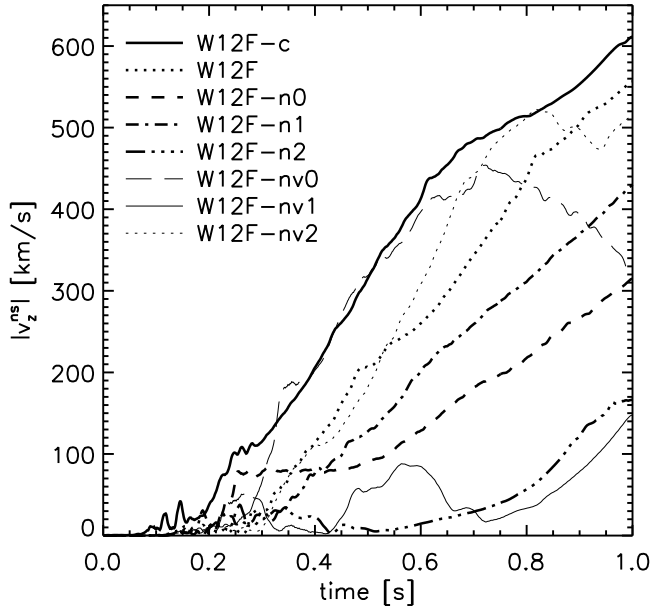


Fig. 25. Neutron star velocities (absolute values) as functions of time for Models W12F-c, W12F and several other models with fast neutron star contraction. In six out of eight models the neutron star moves faster than 300 km/s at $t = 1 \text{ s}$.

dynamic instabilities like convection, the acoustic-vortex cycle or the SASI mechanism. With the faster shrinking of the neutron star not only the explosion time scale decreases, but also other important conditions change, e.g. the neutrino luminosities and ν -heating become larger, the advection time scale in the postshock layer shorter and the sound speed between shock and neutron star higher. These changes affect the growth of instabilities strongly (see Scheck et al., in preparation).

In fact, there are indications that a faster contraction of the nascent neutron star favours higher values for the average recoil velocity. In our largest sample of models sharing the same (slowly contracting) boundary condition, i.e. the 18 B18-like models listed in Tables 1 and 5, only three simulations develop neutron star recoil velocities of more than 500 km/s, and only seven produce neutron stars with more than 300 km/s at 1 second. In contrast, in just eight simulations with rapid boundary contraction we obtain six models with neutron star velocities of more than 300 km/s and three models with neutron stars moving faster than 500 km/s (Fig. 25). Better statistics would require more simulations, which should also be based on the

same initial model¹ and should make use of the same gravitational potential.

We performed some of the simulations discussed above with Newtonian gravity to demonstrate that the choice of the effective relativistic potential in our models was not essential for our results. We recall that only when we use the Newtonian gravitational potential, momentum is strictly conserved in our simulations (also when the point mass is increased with time). The results therefore show that large neutron star recoil velocities are *not* linked to any violation of total momentum conservation associated with the use of the effective relativistic potential (see the discussion in Sect. 4.2).

7.4. Long-time evolution of the neutron star kicks

In order to investigate how the neutron star recoil velocities evolve beyond a time of one second after core bounce, we perform six exemplary long-time simulations. For these we add 150 radial zones to our grid and place the outer grid boundary at a larger radius of 10^{10} cm, which allows us to simulate the first 3–4 s of the post-bounce evolution. In three of the simulations an infinite inertial neutron star mass is assumed, while in the other models the hydrodynamic feedback of the neutron star motion is taken into account. Four of the six models are just continued from models which we have computed up to a time of one second with our standard grid. We map the corresponding data onto the larger grid at $t = 750$ ms and extend the initial model profile from the old to the larger outer boundary of the new grid.

The evolution of the neutron star velocities for all of the long-time simulations is displayed in Fig. 26. The neutron star of Model B18-3, which we already discussed as an extreme case in Sect. 4.5, is accelerated to more than 1200 km/s within 3.7 s. This demonstrates that the acceleration mechanism at work in our calculations has the potential to explain even the highest observed pulsar velocities (see e.g. Chatterjee et al. 2005). The fact that Model B18-3 is the only one in our sample that produces a neutron star with more than 1000 km/s does not appear problematic to us. It may be a matter of low-number statistics and might also change when more extreme conditions are realized in models, e.g. by a faster contraction of the neutron star than assumed in our standard set of models. In this respect the sample of simulations plotted in Fig. 25 looks promising. In quite a number of those the neutron stars have large velocities at one second and also still high accelerations (see, e.g., Model W12F-c in Table 8).

After 3–4 s the neutrino-driven wind has blown away all downflows from the neutron star vicinity and has generated a nearly spherically symmetric wind bubble around it. Therefore the neutron star acceleration diminishes and the recoil velocities approach their terminal values. The latter can be estimated by extrapolating the velocities at $t = 1$ s, applying an average acceleration value $\langle a_z^{\text{ns}} \rangle$, as computed for the time interval between $t = 0.5$ s and 1 s, over a time period $\Delta t_{\text{extrapol}}$, according

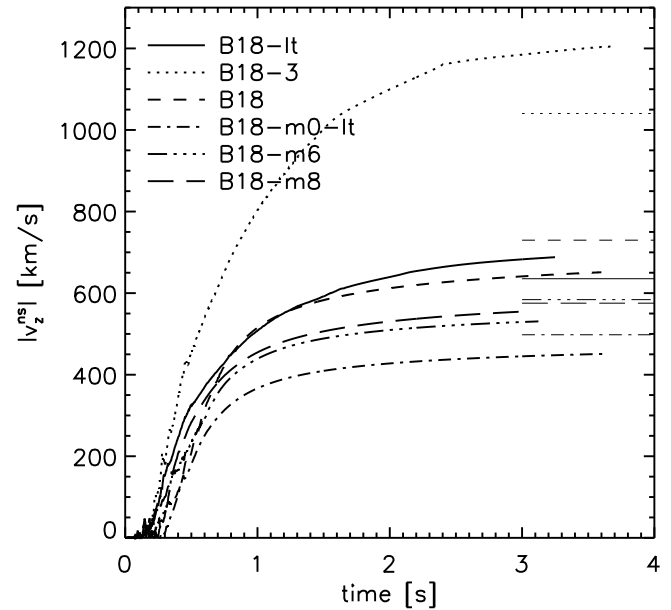


Fig. 26. Evolution of the neutron star velocities in six long-time simulations with the same boundary conditions as Model B18. After four seconds the acceleration has become very weak in all models and no significant further increase of the velocities is expected. For each model a thin horizontal line marks the extrapolated velocity value v_{ns}^{∞} according to Eq. (46), which is a rough estimate of the final neutron star velocity.

to

$$v_{\text{ns}}^{\infty} = v_z^{\text{ns}}(t = 1 \text{ s}) + \Delta t_{\text{extrapol}} \times \langle a_z^{\text{ns}} \rangle. \quad (46)$$

The average acceleration $\langle a_z^{\text{ns}} \rangle$ is introduced as a time-average which is less sensitive to short-time variations of the neutron star acceleration and thus allows for a more robust extrapolation of the velocities. The factor $\Delta t_{\text{extrapol}} = 0.35$ s is “calibrated” by optimising the estimates in case of the models of Fig. 26. The agreement of extrapolated and computed terminal velocities is typically of the order of 10%. In the following section we use Eq. (46) to estimate the final neutron star velocities for all models listed in Tables 1–5. The basic findings of our analysis do not depend on whether we use a_z^{ns} (the acceleration values at the end of our simulations) or $\langle a_z^{\text{ns}} \rangle$ (the mean values in the last 0.5 s) for extrapolating the velocities beyond the simulated period of one second of evolution.

8. Implications for the neutron star velocity distribution

In Sect. 5 we mentioned that Fig. 16, showing the neutron star velocities and accelerations at $t = 1$ s, suggests the existence of two groups of models. One group consists of cases with low velocities and on average low acceleration, and the other group cases with high velocities and significantly higher average acceleration. The latter models are typically characterised by a strong $l = 1$ mode in the flow pattern at the end of our simulations.

¹ The comparison between B and W models is viable, however, because both progenitor models are quite similar.

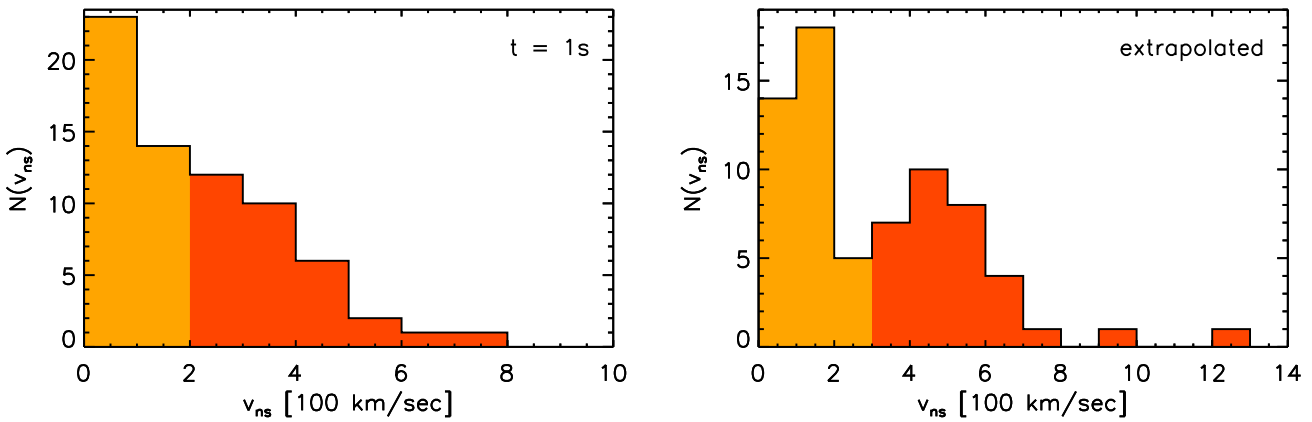


Fig. 27. Histograms of the neutron star velocity distribution for the 70 models of Tables 1–5. The left panel shows the velocity distribution at $t = 1$ s (solid black line). The darker shaded area corresponds to the fraction of models whose neutron stars are moving with more than 200 km/s one second after bounce. The same models are displayed with dark shading also in the right panel, which shows the final velocity distribution as obtained by extrapolation with Eq. (46).

Provided the acceleration shows a trend of increasing more steeply than linearly with the neutron star velocity, one can expect a growth of the separation of both populations when the acceleration continues over a longer period of time. Thus a bimodal velocity distribution will emerge, caused by the larger acceleration associated with the presence of a dominant $l = 1$ mode in the models of the high-velocity group. To test this possibility, we extrapolate the neutron star motions of all of our 70 models listed in Tables 1–5 from one second to the expected final conditions by applying Eq. (46). Figure 27 displays both the velocity distribution at the end of the simulated evolution (at $t = 1$ s; left panel) and the terminal distribution (right panel).

A comparison of the panels in Fig. 27 shows that most neutron stars of the high-velocity and high-acceleration group (which is indicated by the darker shading) accelerate to significantly higher velocities on time scales longer than one second. In contrast, only very few stars of the low-velocity group reach velocities in excess of 200 km/s. As a consequence, a minimum develops in the extrapolated distribution around 300 km/s, separating clearly the two components in velocity space.

We interpret this result as an interesting demonstration that the kick mechanism discussed here is able to produce a bimodal distribution of neutron star velocities simply due to the presence or absence of a dominant $l = 1$ mode in the spatial distribution of the supernova ejecta. Invoking two different processes for neutron star acceleration is not required. It is, however, unclear whether this may provide an explanation of a possible bimodality in the observed velocity distribution of pulsars. The existence of such a bimodality is not only ambiguous, some authors finding hints (e.g. Cordes & Chernoff 1998; Fryer et al. 1998; Arzoumanian et al. 2002; Brisken et al. 2003), while others favour a one-component Maxwellian distribution (e.g. Lyne & Lorimer 1994; Hansen & Phinney 1997; Hobbs et al. 2005; Zou et al. 2005). Also the parameters for the two-component fits differ significantly between the publications.

Though our result is inspiring as well as tantalising, we refrain from making a direct connection with observations. Such

attempts are hampered by the limitations of our analysis, which does not only assume the extrapolation of Eq. (46) to be valid for all cases. Our analysis is also affected by our finding that the magnitude of the neutron star kicks seems to depend on the neutron star contraction (see Sect. 7.3) that is mimicked in our simulations by a moving inner boundary of the computational grid. Moreover, our analysis is constrained to a set of $15 M_{\odot}$ stars², while linking theory with observations would require modelling explosions for a representative distribution of supernova progenitors, making reasonable assumptions about the progenitor dependence of the explosion energy and including the effects from binary breakup. A large set of calculations would have to account for the stochastic nature of the discussed neutron star acceleration mechanism, thus establishing the distribution of kick velocities as a function of the progenitor properties. One might have the concern that in the combined data of all of these runs the minimum visible in the velocity distribution of Fig. 27 is filled up. Finally, quantitatively meaningful calculations of neutron star kicks will ultimately have to be obtained by three-dimensional modelling.

9. Summary and conclusions

The aim of this work was an investigation of hydrodynamic instabilities in the neutrino-heated postshock layer of core-collapse supernovae and of the importance of such instabilities for the development of explosion anisotropies and neutron star kicks.

For this purpose we have presented a large number (more than 70) of supernova simulations in two dimensions (i.e., assuming axisymmetry) for different $15 M_{\odot}$ progenitor models, relying on the viability of the neutrino-driven explosion mechanism. Since this viability is still an open question and no explo-

² The employed progenitor models, however, exhibit large differences in core sizes and core density profiles, which actually may be considered as reflecting the variations over a broader range progenitor masses.

sions are obtained in 2D models with a detailed spectral treatment of neutrino transport for stars more massive than about $11 M_{\odot}$ (see Buras et al. 2005a,b), we triggered the explosions in our simulations by replacing the contracting core of the nascent neutron star by an inner boundary of the computational grid and assuming there suitable neutrino luminosities from the neutron star core. The boundary was placed at a Lagrangian mass coordinate of typically $1.1 M_{\odot}$, where the neutrino optical depths were usually 10 or higher. A systematic variation of the core neutrino luminosities imposed at this boundary allowed us to investigate the growth of hydrodynamic instabilities and the development of the explosion in dependence of the strength of the neutrino heating and thus of the size of the explosion energy.

The neutrino transport in these simulations was treated by a characteristics-based radial integration of the neutrino-energy equation, which could be performed analytically by assuming that the effective local speed of neutrino propagation is given by a radius-dependent function that fits Monte-Carlo results for neutrino transport in the semi-transparent and transparent regimes. This improvement compared to a light-bulb approximation offers the possibility to follow the radial change of the neutrino flux in response to the neutrino emission in the accretion layer and neutrino absorption in the heating layer. The neutrino spectra were approximated by Fermi-Dirac functions. Solving the lepton number transport separately from the energy transport allowed us to determine the neutrino spectral temperature independently from the gas temperature. The spectral degeneracy parameter was assumed to be equal to the equilibrium value at high optical depths and to approach smoothly a fixed value outside of the neutrinosphere. The latter value was chosen to reproduce the typical spectral distribution of escaping neutrinos as determined by multi-energy transport calculations. The transport of neutrinos of all flavours was taken into account, and all relevant neutrino-matter interactions (in particular for ν_e and $\bar{\nu}_e$, which are most relevant for the heating of the postshock layer) were included. While the neutrino flux was prescribed isotropically at the inner boundary in all of the presented simulations, the transport on the grid was followed in a “ray-by-ray” description, i.e., assuming the local neutrino flux is radial. Thus we integrated the radius-dependent neutrino-energy equation separately for the different lateral zones of the employed polar 2D grid. A detailed description of the transport treatment was given in Sect. 2.2 and Appendix A.

Our adherence to the neutrino-driven explosion mechanism and our procedure of triggering supernova explosions by the use of a boundary condition for the neutrino flux may be justified by the still remaining uncertainties in the most recent 2D supernova simulations in spite of the significant improvements of the treatment of neutrino physics and transport compared to the first generation of multi-dimensional models. While the latter simulations used gray neutrino diffusion and found explosions (e.g. Herant et al. 1994; Burrows et al. 1995; Fryer 1999; Fryer & Warren 2002, 2004), more recent 2D simulations with spectral transport (see Buras et al. 2003, 2005a,b) could not confirm the success of the previous models with the simplified neutrino description. However, it should be noted that 3D simulations with spectral transport have not been done yet, but might reveal important differences in the flow dynamics compared to

axisymmetric models, in particular with respect to the growth of Rayleigh-Taylor and convective instabilities, non-radial accretion shock instabilities, and vortex behaviour. Moreover, the question whether convective or mixing processes below and around the neutrinosphere could enhance the neutrinospheric neutrino emission and thus support the neutrino heating behind the shock, must still be considered as unsettled: Doubly diffusive instabilities (Bruenn et al. 2006), neutrino-bubble instabilities (Socrates et al. 2005), or magnetic buoyancy instabilities (Wilson et al. 2005) deserve further investigation by multi-dimensional modelling. Also magneto-rotational instabilities were suggested to aid the explosion by creating viscous heating behind the shock in addition to the still dominant energy input there by neutrinos (Thompson et al. 2005).

Our main results can be summarised as follows.

1. The approximative treatment of the neutrino transport described in this paper is able to reproduce the overall behaviour of neutrino luminosities and mean energies as found in spectral Boltzmann transport calculations. A detailed quantitative comparison, however, is hampered by the radical approximations inherent in the scheme and the strongly simplified handling of the neutrino-matter interactions (ignoring, e.g., complexities of the neutrino distribution in the momentum space). In contrast to previous work (Janka & Müller 1996; Kifonidis et al. 2003) the neutrino luminosities of the neutron star core in the models presented here were not assumed to decay exponentially, but – in better agreement with transport calculations for the whole neutron star – were assumed to remain (roughly) constant over hundreds of milliseconds after bounce. With this boundary condition the transport treatment of the current models ensures a radial and temporal behaviour of the neutrino luminosities and mean spectral energies as qualitatively also found in more complete and fully consistent supernova models.
2. Random perturbations, by which we seed the growth of non-radial instabilities in our simulations, can grow from small initial amplitudes (between 0.1% and some percent of the fluid velocity) to global asphericities by convective instability as well as the vortical-acoustic cycle (Foglizzo 2001, 2002), provided the time until the onset of rapid shock expansion is sufficiently long. Once the shock expansion gains momentum, the further growth of the instabilities, e.g. by the merging of smaller structures to larger ones, is quenched, and the flow pattern essentially freezes out. Not the absolute time until explosion matters in this context, but the delay time relative to the typical growth time scale of the instability. A detailed investigation of the growth of different kinds of non-radial instabilities in the postshock flow and their competition will be published in a subsequent paper (Scheck et al. 2006, in preparation). The neutrino transport description and employed inner boundary condition for the transport used in this work ensured a sufficient delay of the shock acceleration, in contrast to the light-bulb parameters employed by Janka & Müller (1996) and Kifonidis et al. (2003).

3. The growth of the instabilities proceeds extremely nonlinearly and chaotically such that the final ejecta anisotropy turns out to be sensitive to the initial random pattern of the seed perturbations as well as small differences between numerical runs (connected, e.g., to small changes in the grid zoning, machine specific truncation and roundoff errors or small differences of the input physics). Despite the different ejecta geometry, however, integral parameters of the models such as the neutron star mass, explosion time scale or explosion energy, show little variability.
4. This is different for quantities, which depend on hemispheric asymmetries. The instabilities lead to symmetry breaking and the ejecta can attain a net linear momentum, balanced by the recoil absorbed by the neutron star. In practise, the momentum exchange was found to be mediated by gravitational as well as hydrodynamic forces. Typically the former are more important, but in cases where the neutron star accretes anisotropically over long periods of time, also hydrodynamic interaction can contribute significantly. In our standard setup for the calculations, the neutron star is fixed (due to the use of the inner grid boundary) at the centre of the grid. Since it therefore does not start moving in spite of momentum gain, this situation can be considered as a case where the neutron star is assumed to have infinite inertial mass. In order to test whether this affects the results, we performed a number of runs by imposing the negative of the instantaneous neutron star velocity (as calculated from its attained momentum) on the ambient gas on the computational grid. This leads to a collective gas motion relative to the neutron star fixed at the grid centre and corresponds to a change of the frame of reference by applying a Galilei transformation after every hydrodynamics step. Although, of course, a specific model develops differences, we could not detect any changes of the ensemble behaviour with respect to explosion parameters or magnitude and distribution of neutron star kick velocities.
5. Further tests also showed that the details of the neutrino treatment, the employed gravitational potential (i.e., performing the simulations with Newtonian gravity or an effective relativistic potential according to Marek et al. (2005), the assumed amplitude of initial perturbations or the assumed contraction of the inner grid boundary (which mimics the shrinking of the cooling nascent neutron star) do not have any qualitative influence on our results for the neutron star kicks. Quantitatively, we discovered indications (based on a limited set of computations, however) that a faster contraction of the forming neutron star – which may correspond to a softer nuclear equation of state or more rapid cooling – seems to favour higher neutron star kicks on average. This can be explained by the more rapid release of gravitational binding energy, stronger neutrino heating and gravitational acceleration, and thus a more violent gas flow between neutron star and shock.
6. While the neutrino flux imposed at the inner grid boundary was assumed to be isotropic in all of our simulations, the neutrino radiation at large distances from the neutron star could become anisotropic because of lateral differences in the neutrino emission and absorption. The

biggest such differences are associated with long-lasting, narrow downflows through which the neutron star accretes gas anisotropically. The gas heats up strongly upon falling towards the neutron star surface and getting decelerated in shocks. We found, however, that the corresponding anisotropic neutrino emission produces a neutrino-mediated acceleration, which accounts only for small corrections to the neutron star velocities produced by the asymmetric mass ejection. These corrections rarely exceed 10%. Both accelerations usually produce motion in opposite directions. The reason for this is that the neutron star receives a kick *towards* a downflow (which attracts the neutron star gravitationally or leads to a momentum deficit of the expanding ejecta shell on the side of the downflow), whereas the neutrino radiation is more intense in the hemisphere of the downflow and thus propels the neutron star in the other direction. Since the accretion luminosity is radiated near the neutron star surface, we do not think that our use of the inner boundary underestimates this effect. The inverse is more likely. Our “ray-by-ray” radial transport tends to overestimate the anisotropy of the outgoing radiation, because truly multi-dimensional transport would redistribute the locally emitted neutrinos more isotropically in all directions instead of favouring their radial propagation (see the discussion in Livne et al. 2004).

7. After one second of post-bounce evolution, which was the period of time we simulated for most models, we obtained maximum neutron star velocities up to 800 km/s. The models appear grouped in two populations, one in which the neutron stars move with less than 200 km/s and have low acceleration at $t = 1$ s, and another one, roughly equally strong, where the stars have velocities higher than 200 km/s and on average also higher accelerations (see Figs. 15, 16, and the left panel of Fig. 27). The two groups differ by the absence or presence, respectively, of a strong or dominant $l = 1$ dipole mode in the gas distribution around the neutron star. The simulated models cover roughly equally a range of explosion energies between about 0.3×10^{51} erg and more than 1.5×10^{51} erg. We could not detect any systematic variations of the typical magnitude or scatter of the kick velocities with the explosion energy. We also did not discover any obvious correlation of the kicks with the properties of the three considered $15 M_{\odot}$ progenitor stars, which exhibited major differences in their core sizes and density structures. Rotation with a fairly high pre-collapse rate of 0.5 rad/s in the iron core, which in view of the most recent stellar evolution models is probably unrealistically large for ordinary supernovae (see Heger et al. 2004), lead to slightly higher explosion energies (due to a larger mass in the gain layer), a more spherical shock surface, and the presence of downflows at both poles of the rotating neutron star. This suggests a weaker contribution of an $l = 1$ mode in this situation compared to the nonrotating models, where downflows in only one hemisphere are rather common. Although very extreme cases were missing in our fairly small sample of simulations with such rapid rotation, we nevertheless obtained kick velocities in excess of 300 km/s (still rising at one second after bounce), and could not detect any bias to-

wards the group with low velocities and low average acceleration.

8. The two populations in our velocity distribution at one second are certainly interesting in view of the possibility of a bimodality in the distribution of measured pulsar velocities, which however is still controversial. We therefore attempted to derive from our set of about 70 simulations the distribution at the time the neutron stars have reached their terminal velocities. In order to do that we continued some of our models until 3–4 seconds, at which time the accelerations have become very small. These models served for calibrating the typical period of time which a representative acceleration must be applied to extrapolate from the velocity at one second to the terminal values. The representative acceleration was taken as the average value between 0.5 s and 1 s after bounce, a choice which guaranteed that short-time fluctuations of the size and direction of the acceleration (which are rather frequent in case of low-energetic explosions) do not corrupt the extrapolation. Indeed the extrapolated velocity distribution revealed a clear bimodal structure with a minimum around 300 km/s and a high-velocity component that extends up to 1300 km/s (right panel of Fig. 27). This component consists of most of the neutron stars that belong to the high-velocity, high-acceleration group at one second. Both components are similar in strength, but this may depend on the choices of parameters for the considered set of models. The basic result of a bimodality, however, turned out to be very robust against variations of the exact way of extrapolation.

Although the presence or absence of a pronounced $l = 1$ mode in the ejecta distribution offers a natural as well as suggestive way to obtain a bimodality in the context of our hydrodynamic kick mechanism, we refrain from claiming that our result is a strong support for the existence of such a bimodality in the observed distribution of pulsar velocities. There are too many uncertainties which might lead to a filling of the minimum of our distribution. Not only do we assume that our extrapolation law (Eq. 46) can be applied with the same value for the duration of the average acceleration to all models of our sample, we also consider only a very constrained selection of progenitor models, which is not representative for the true distribution of supernova progenitors. Though our simulations do not reveal systematic differences of the kicks in dependence of the explosion energy or progenitor structure, we do not feel able to exclude that a correlation of both over the range of supernova progenitors could not conspire such that the bimodality of Fig. 27 gets wiped out.

Apart from all the assumptions and approximations entering this work and discussed in detail above, the biggest deficiency of the present analysis is the fact that it is based on simulations which assume axial symmetry with the polar axis being a coordinate singularity that is impenetrable for the fluid flow. Currently it is neither clear to which degree pronounced $l = 1$ modes of the ejecta distribution and long-lasting downflows of matter to the neutron star can develop in the three-dimensional environment, and how common they are, although first 3D simulations with the setup and input physics described here are

promising (they will be presented in a future publication, but see Janka et al. 2005b for some results). Nor is it clear what the distribution of neutron star recoil velocities from 3D models will be. The large number of long-time simulations required by the stochastic nature and long duration of the proposed hydrodynamic kick mechanism, is currently out of reach due to its enormous demand of computer time. Our results must therefore be considered as indicative but they are far from providing definitive answers.

Acknowledgements. We thank R. Buras, M. Rampp and S. Bruenn for providing us with post-bounce models, M. Limongi and S. Woosley for their progenitor models, and J. Niemeyer for valuable suggestions. Support by the Sonderforschungsbereich 375 on “Astroparticle Physics” of the Deutsche Forschungsgemeinschaft is acknowledged. We are grateful to the Institute for Nuclear Theory at the University of Washington for its hospitality during several visits throughout the duration of this work. The computations were performed on the NEC SX-5/3C of the Rechenzentrum Garching (RZG) and the IBM p690 clusters of the RZG and the John-von-Neumann Institute for Computing in Jülich.

References

Arras, P. & Lai, D. 1999a, ApJ, 519, 745
 Arras, P. & Lai, D. 1999b, Phys. Rev. D, 60, 043001
 Arzoumanian, Z., Chernoff, D. F., & Cordes, J. M. 2002, ApJ, 568, 289
 Blondin, J. M. & Mezzacappa, A. 2005, ApJ, submitted, astro-ph/0507181
 Blondin, J. M., Mezzacappa, A., & DeMarino, C. 2003, ApJ, 584, 971
 Brisken, W. F., Fruchter, A. S., Goss, W. M., Herrnstein, R. M., & Thorsett, S. E. 2003, AJ, 126, 3090
 Bruenn, S. W. 1985, ApJS, 58, 771
 Bruenn, S. W. 1993, in Nuclear Physics in the Universe, ed. M. W. Guidry & M. R. Strayer (Bristol: IOP), 31
 Bruenn, S. W., Raley, E. A., & Mezzacappa, A. 2006, ApJ, submitted, astro-ph/0404099
 Buras, R., Rampp, M., Janka, H.-T., & Kifonidis, K. 2003, Phys. Rev. Lett., 90, 241101
 Buras, R., Rampp, M., Janka, H.-T., & Kifonidis, K. 2005a, A&A, submitted, astro-ph/0507135
 Buras, R., Rampp, M., Janka, H.-T., & Kifonidis, K. 2005b, A&A, submitted, astro-ph/0512189
 Burrows, A. & Fryxell, B. A. 1993, ApJ, 418, L33
 Burrows, A. & Hayes, J. 1996, Phys. Rev. Lett., 76, 352
 Burrows, A., Hayes, J., & Fryxell, B. A. 1995, ApJ, 450, 830
 Cen, R. 1998, ApJ, 507, L131
 Chandrasekhar, S. 1961, Hydrodynamic and hydromagnetic stability (New York: Dover)
 Chatterjee, S., Vlemmings, W. H. T., Brisken, W. F., et al. 2005, ApJ, 630, L61
 Colella, P. & Woodward, P. R. 1984, J. Comput. Phys., 54, 174
 Cordes, J. M. & Chernoff, D. F. 1998, ApJ, 505, 315
 Cordes, J. M., Romani, R. W., & Lundgren, S. C. 1993, Nature, 362, 133
 Einfeldt, B. 1988, SIAM J. Num. Anal., 25, 294
 Foglizzo, T. 2001, A&A, 368, 311

Foglizzo, T. 2002, A&A, 392, 353

Foglizzo, T. & Galletti, P. 2004, in Proc. of the workshop "3-D signatures in stellar explosions", June 10-13 2003, Austin, Texas, USA, ed. P. Hoflich, P. Kumar, & J. C. Wheeler (Cambridge, UK: Cambridge University Press), 238, astro-ph/0308534

Foglizzo, T., Scheck, L., & Janka, H.-T. 2005, A&A, submitted, astro-ph/0507636

Foglizzo, T. & Tagger, M. 2000, A&A, 363, 174

Fryer, C., Burrows, A., & Benz, W. 1998, ApJ, 496, 333

Fryer, C. & Kusenko, A. 2005, ApJ, submitted, astro-ph/0512033

Fryer, C. L. 1999, ApJ, 522, 413

Fryer, C. L. & Heger, A. 2000, ApJ, 541, 1033

Fryer, C. L. & Warren, M. S. 2002, ApJ, 574, L65

Fryer, C. L. & Warren, M. S. 2004, ApJ, 601, 391

Fuller, G. M., Kusenko, A., Mocioiu, I., & Pascoli, S. 2003, Phys. Rev. D, 68, 103002

Galletti, P. & Foglizzo, T. 2005, in Proc. of the SF2A meeting, 17-30 June 2005, Strasbourg, EDPS Conference Series in Astronomy & Astrophysics, ed. F. Casoli, T. Contini, H. M. Hameury, & L. Pagani, astro-ph/0509635

Goldreich, P., Lai, D., & Sahrling, M. 1996, in Unsolved Problems in Astrophysics, ed. J. N. Bahcall & J. P. Ostriker (Princeton: Princeton Univ. Press)

Hansen, B. M. S. & Phinney, E. S. 1997, MNRAS, 291, 569

Heger, A., Langer, N., & Woosley, S. E. 2000, ApJ, 528, 368

Heger, A., Woosley, S., Langer, N., & Spruit, H. C. 2004, in Proc. IAU Symp. No. 215, ed. A. Maeder & P. Eenens (San Francisco: Astronomical Society of the Pacific), 591, astro-ph/0301374

Herant, M. 1995, Phys. Rep., 256, 117

Herant, M., Benz, W., & Colgate, S. 1992, ApJ, 395, 642

Herant, M., Benz, W., Hix, W. R., Fryer, C. L., & Colgate, S. A. 1994, ApJ, 435, 339

Hobbs, G., Lorimer, D. R., Lyne, A. G., & Kramer, M. 2005, MNRAS, 360, 974

James, F. 1994, Comput. Phys. Commun., 79, 111

James, F. 1996, Comput. Phys. Commun., 97, 357

Janka, H.-T. 1990, in Nuclear Astrophysics, 5th Workshop, 130-+

Janka, H.-T. 1991, Dissertation, Technische Universität München

Janka, H.-T., Buras, R., Kifonidis, K., Plewa, T., & Rampp, M. 2003, in From Twilight to Highlight: The Physics of Supernovae, Proc. of the ESO/MPA/MPE Workshop, Garching, Germany, July 29-31, 2002, ed. W. Hillebrandt & B. Leibundgut (Berlin: Springer), 39, astro-ph/0212316

Janka, H.-T., Buras, R., Kifonidis, K., Plewa, T., & Rampp, M. 2004a, in Stellar Collapse, ed. C. Fryer (Dordrecht: Kluwer Academic Publishers), 65, astro-ph/0212314

Janka, H.-T., Buras, R., Kitaura Joyanes, F., Marek, A., & Rampp, M. 2004b, in Procs. of the 12th Workshop on Nuclear Astrophysics, Ringberg Castle, Tegernsee, March 22-27, 2004, Report MPA-P14, Max-Planck-Institut für Astrophysik, Garching, ed. E. Müller & H.-T. Janka, 150, astro-ph/0405289

Janka, H.-T. & Hillebrandt, W. 1989, A&AS, 78, 375

Janka, H.-T., Kifonidis, K., Buras, R., Marek, A., & Rampp, M. 2005a, in Cosmic Explosions (On the 10th Anniversary of SN1993J), Proceedings IAU Coll. 192, Valencia, Spain, April 22-26, 2003, ed. J. Marcaide & K. Weiler (Berlin: Springer Verlag), 253, astro-ph/0401461

Janka, H.-T. & Müller, E. 1994, A&A, 290, 496

Janka, H.-T. & Müller, E. 1996, A&A, 306, 167

Janka, H.-T., Scheck, L., Kifonidis, K., Müller, E., & Plewa, T. 2005b, in ASP Conf. Ser. 332: The Fate of the Most Massive Stars, ed. R. Humphreys & K. Stanek (San Francisco: Astronomical Society of the Pacific), 372, astro-ph/0408439

Johnston, S., Hobbs, G., Vigeland, S., et al. 2005, MNRAS, 364, 1397

Kane, J., Arnett, W. D., Remington, B. A., et al. 2000, ApJ, 528, 989

Keil, M. T., Raffelt, G. G., & Janka, H.-T. 2003, ApJ, 590, 971

Khokhlov, A. M., Höflich, P. A., Oran, E. S., et al. 1999, ApJ, 524, L107

Kifonidis, K., Plewa, T., Janka, H.-T., & Müller, E. 2003, A&A, 408, 621

Kifonidis, K., Plewa, T., Scheck, L., Janka, H.-T., & Müller, E. 2005, A&A, submitted, astro-ph/0511369

Kotake, K., Sawai, H., Yamada, S., & Sato, K. 2004, ApJ, 608, 391

Kotake, K., Yamada, S., & Sato, K. 2003, ApJ, 595, 304

Kuhlen, M., Woosley, W. E., & Glatzmaier, G. A. 2003, in ASP Conf. Ser. Vol. 293: 3D Stellar Evolution, ed. S. Turcotte, S. Keller, & R. Cavallo (San Francisco: Astron. Society of the Pacific), 147

Lai, D. 2001, in LNP Vol. 578: Physics of Neutron Star Interiors, ed. D. Blaschke, N. Glendenning, & A. Sedrakian (Berlin: Springer), 424

Lai, D., Chernoff, D. F., & Cordes, J. M. 2001, ApJ, 549, 1111

Lai, D. & Goldreich, P. 2000, ApJ, 535, 402

Lattimer, J. M. & Swesty, F. D. 1991, Nucl. Phys. A, 535, 331

Liebendörfer, M., Mezzacappa, A., Thielemann, F., et al. 2001, Phys. Rev. D, 63, 103004

Liebendörfer, M., Rampp, M., Janka, H.-T., & Mezzacappa, A. 2005, ApJ, 620, 840

Limongi, M., Straniero, O., & Chieffi, A. 2000, ApJS, 129, 625

Livne, E., Burrows, A., Walder, R., Lichtenstadt, I., & Thompson, T. A. 2004, ApJ, 609, 277

Lüscher, M. 1994, Comput. Phys. Commun., 79, 100

Lyne, A. G. & Lorimer, D. R. 1994, Nature, 369, 127

Marek, A., Dimmelmeyer, H., Janka, H.-T., Müller, E., & Buras, R. 2005, A&A, submitted, astro-ph/0502161

Minerbo, G. N. 1978, J. Quant. Spectrosc. Radiat. Transfer, 20, 541

Murphy, J. W., Burrows, A., & Heger, A. 2004, ApJ, 615, 460

Myra, E. S. & Burrows, A. 1990, ApJ, 364, 222

Ohnishi, N., Kotake, K., & Yamada, S. 2005, ApJ, submitted, astro-ph/0509765

Rampp, M. & Janka, H.-T. 2000, ApJ, 539, L33

Rampp, M. & Janka, H.-T. 2002, A&A, 396, 361

Scheck, L., Plewa, T., Janka, H.-T., Kifonidis, K., & Müller, E. 2004, Phys. Rev. Lett., 92, 011103

Schinder, P. J., Schramm, D. N., Wiita, P. J., Margolis, S. H., & Tubbs, D. L. 1987, ApJ, 313, 531

Socrates, A., Blaes, O., Hungerford, A., & Fryer, C. 2005, ApJ, submitted, astro-ph/0412144

Tassoul, J.-L. 1978, Theory of Rotating Stars (Princeton, New Jersey: Princeton University Press)

Thompson, C. 2000, ApJ, 534, 915

Thompson, T. A., Burrows, A., & Meyer, B. S. 2001, ApJ, 562, 887

Thompson, T. A., Burrows, A., & Pinto, P. A. 2003, ApJ, 592, 434

Thompson, T. A., Quataert, E., & Burrows, A. 2005, ApJ, 620, 861

Tubbs, D. L. 1979, ApJ, 231, 846

Tubbs, D. L. & Schramm, D. N. 1975, ApJ, 201, 467

Wang, C., Lai, D., & Han, J. 2005, ApJ, submitted, astro-ph/0509484

Wang, L., Baade, D., Höflich, P., & Wheeler, J. C. 2003, ApJ, 592, 457

Wang, L., Howell, D. A., Höflich, P., & Wheeler, J. C. 2001, ApJ, 550, 1030

Wang, L., Wheeler, J. C., Höflich, P., et al. 2002, ApJ, 579, 671

Wheeler, J. C., Meier, D. L., & Wilson, J. R. 2002, ApJ, 568, 807

Wilson, J. R., Mathews, G. J., & Dalhed, H. E. 2005, ApJ, 628, 335

Woodward, P. R., Porter, D. H., & Jacobs, M. 2003, in ASP Conf. Ser. Vol. 293: 3D Stellar Evolution, ed. S. Turcotte, S. Keller, & R. Cavallo (San Francisco: Astron. Society of the Pacific), 45

Woosley, S. E., Pinto, P. A., & Enzman, L. 1988, ApJ, 324, 466

Woosley, S. E. & Weaver, T. A. 1995, ApJS, 101, 181

Zou, W. Z., Hobbs, G., Wang, N., et al. 2005, MNRAS, 362, 1189

Appendix A: Neutrino Transport

A.1. Transport Equation

We start from the equation of radiation transport in spherical symmetry

$$\frac{1}{c} \frac{\partial}{\partial t} I + \mu \frac{\partial}{\partial r} I + \frac{1-\mu^2}{r} \frac{\partial}{\partial \mu} I = S, \quad (\text{A.1})$$

where $I = I(t, r, \epsilon, \mu)$ is the specific intensity, $S = S(t, r, \epsilon, \mu)$ is the source function, ϵ is the neutrino energy, $\mu = \cos \theta$ and θ is the angle between radiation propagation and radial direction. Solid angle integration yields the zeroth angular moment equation,

$$\frac{1}{c} \frac{\partial}{\partial t} J + \frac{1}{r^2} \frac{\partial}{\partial r} (r^2 H) = S^{(0)} \equiv \frac{1}{2} \int_{-1}^{+1} d\mu S \quad (\text{A.2})$$

with $\{J, H\}(t, r, \epsilon) := \frac{1}{2} \int_{-1}^{+1} d\mu \mu^{[0,1]} I(t, r, \epsilon, \mu)$. Integration over energy leads to

$$\frac{\partial}{\partial t} E + \frac{1}{r^2} \frac{\partial}{\partial r} (r^2 F) = Q^+ - Q^- \quad (\text{A.3})$$

with $\{E, F\}(t, r) := 4\pi \int_0^{\infty} d\epsilon \{J/c, H\}(t, r, \epsilon)$ being energy density and energy flux, respectively. The source term has been

split in an emission rate Q^+ and an absorption rate $Q^- = \kappa_a c E$, which is proportional to the energy density. The *flux factor* is defined as the ratio of flux to energy density,

$$f(r, t) := F(r, t) / c E(r, t). \quad (\text{A.4})$$

In neutrino transport simulations solving the full Boltzmann equation (see e.g. Buras et al. 2003, 2005a,b) this quantity shows only little short-time variability during most phases of the supernova evolution. Therefore $\partial f / \partial t = 0$ is an acceptably good approximation. With $L := 4\pi r^2 F = 4\pi r^2 f c E$ one can now rewrite Eq. (A.3) as

$$\frac{\partial}{\partial t} L + c_{\text{eff}} \frac{\partial}{\partial r} L = 4\pi r^2 c_{\text{eff}} \{Q^+ - Q^-\}, \quad (\text{A.5})$$

where an effective speed of neutrino propagation has been introduced as $c_{\text{eff}} := c f$. Provided c_{eff} were known, the solution of Eq. (A.5) requires considerably less effort than the numerical integration of Eq. (A.1). For vanishing source terms Q^+ and Q^- the neutrino energy or number density is just advected along characteristics $r(t) = r_0 + c_{\text{eff}} t$. Although c_{eff} depends through $f(r, t)$ on the solution of the transport problem (Eq. A.4), neutrino transport calculations in the neutrino-decoupling layer of forming neutron stars reveal that it can be well fitted by a r -dependent function which depends on the steepness of the density profile (see Janka 1990, 1991). Assuming further that the (medium-dependent) coefficients Q^+ and $\tilde{\kappa} \equiv \kappa_a / f = 4\pi r^2 Q^- / L$ are constant between two points (r, t) and (r^*, t^*) , which are connected by a characteristic line, i.e.,

$$r^* = r - c_{\text{eff}} (t - t^*), \quad (\text{A.6})$$

Eq. (A.5) can be integrated analytically to yield

$$\begin{aligned} L(r, t) = & L(r^*, t^*) e^{-\tilde{\kappa} c_{\text{eff}} (t - t^*)} \\ & + \frac{4\pi Q^+}{\tilde{\kappa}^3} \{ [1 - e^{-\tilde{\kappa} c_{\text{eff}} (t - t^*)}] [1 + (\tilde{\kappa} r^* - 1)^2] \\ & + \tilde{\kappa} c_{\text{eff}} (t - t^*) [2\tilde{\kappa} r^* + \tilde{\kappa} c_{\text{eff}} (t - t^*) - 2] \}, \end{aligned} \quad (\text{A.7})$$

where $L(r, t)$ and $L(r^*, t^*)$ are the luminosity values at both ends of the characteristic line.

We use Eq. (A.7) to construct a numerical scheme to solve Eq. (A.5) in the general case: We assume that the luminosity is known at the cell interfaces of a one-dimensional radial grid for a time t^{n-1} , and that the cell-averaged values of the quantities needed to compute the emission rate Q^+ and absorption coefficient $\tilde{\kappa}$ are also known for that time. As a further simplification we do not allow neutrinos to propagate in negative radial direction (actually this is granted by defining a non-negative function for the flux factor, see Sect. A.2). Then the luminosities at $t^n = t^{n-1} + \Delta t$ for each zone interface (starting at the innermost zone) can be computed using Eq. (A.7). In doing so we have to distinguish between two cases (see Fig. A.1): If $c_{\text{eff}} \Delta t > \Delta r$, we can use point A as the starting point of the integration, $(r^*, t^*) = (r_{i-1}, t_A)$. The luminosity at this point is derived from a linear interpolation between $L(r_{i-1}, t^{n-1})$ and $L(r_{i-1}, t^n)$ (which is already known, as we are integrating outwards). If $c_{\text{eff}} \Delta t \leq \Delta r$, we use point B, the luminosity at this point being given by a linear interpolation between $L(r_{i-1}, t^{n-1})$ and $L(r_i, t^{n-1})$.

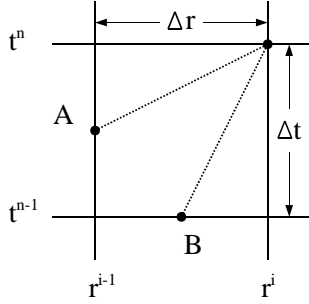


Fig. A.1. The solution at (r^i, t^n) is computed from the data at a point (r^*, t^*) located on the same characteristic line. Depending on the grid spacing, Δr , the time step, Δt , and the effective speed of neutrino propagation, c_{eff} , either point A or point B must be used. The solution there can be obtained by interpolation in time or space, respectively.

For time integration we use a predictor-corrector method: The transport routine is called two times. In the first (predictor) step the luminosities, emission rates and absorption coefficients of the last time step $[L^{n-1}, Q^{n-1}, \kappa^{n-1}]$ are used to compute preliminary values $(\tilde{Q}^n, \tilde{\kappa}^n)$ for the neutrino-medium coupling at the next time level. In the second (corrector) step the final values $[L^n, Q^n, \kappa^n]$ are calculated using $[L^{n-1}, \frac{1}{2}(Q^{n-1} + \tilde{Q}^n), \frac{1}{2}(\kappa^{n-1} + \tilde{\kappa}^n)]$ as input.

Equation (A.5) is solved not only for the energy luminosity $L = L_e$, but also for the number luminosity $L_n = 4\pi r^2 F_n = 4\pi r^2 f_{\text{cn}}$ (n is the particle density and f is assumed to be the same flux factor as for the energy transport). Furthermore the equation has to be integrated for three neutrino types, ν_e , $\bar{\nu}_e$, and ν_x (the latter denoting ν_μ , $\bar{\nu}_\mu$, ν_τ , and $\bar{\nu}_\tau$, which are treated identically). In the following we will use indices $\nu \in \{\nu_e, \bar{\nu}_e, \nu_x\}$ and $\alpha \in \{e, n\}$ to distinguish between these different cases.

In the 2D case the neutrino transport is assumed to proceed only radially, i.e. lateral components of the neutrino flux are ignored and Eq. (A.5) is integrated in radial direction in every lateral zone of the polar coordinate grid. Total luminosities of the star are obtained by summing up the flux densities $L/4\pi r^2$ for all angular cells (at a given radius r), appropriately weighting them with the corresponding surface elements.

A.2. Neutrino Distribution Function

To calculate the source terms we have to make an assumption about the neutrino energy spectrum, i.e. about the energy dependency of the specific intensity, which for particle energy and particle number is linked with the particle distribution function $f_{D,\nu}$ in the following way:

$$I_{\nu,\{n,e\}}(t, r, \epsilon, \mu) = \left(\frac{\epsilon^{2,3}}{(hc)^3} \right) c f_{D,\nu}(t, r, \epsilon, \mu). \quad (\text{A.8})$$

We assume that $f_{D,\nu}$ can be written as product of a Fermi-Dirac distribution function,

$$f_{\text{FD}}(x, \eta) = \frac{1}{1 + \exp(x - \eta)}, \quad (\text{A.9})$$

and an angle-dependent function g_ν ,

$$f_{D,\nu}(r, t, \epsilon, \mu) = g_\nu(r, t, \mu) f_{\text{FD}}\left(\frac{\epsilon}{k_B T_\nu(r, t)}, \eta_\nu(r, t)\right), \quad (\text{A.10})$$

where in general the spectral temperature and degeneracy parameter, T_ν and η_ν , are different from the matter temperature and equilibrium degeneracy parameter.

Furthermore we assume that η_ν is just a function of the optical depth τ_ν :

$$\eta_\nu(\tau_\nu) = \eta_{\text{eq},\nu} (1 - e^{-\tau_\nu}) + \eta_{0,\nu} e^{-\tau_\nu}, \quad (\text{A.11})$$

where $\eta_{\text{eq},\nu}$ is the equilibrium degeneracy parameter and $\eta_{0,\nu}$ is a chosen value as typically found in detailed transport calculations for $\tau_\nu \rightarrow 0$. The values for the different neutrino types are (cf. Janka 1991; Janka & Hillebrandt 1989; Myra & Burrows 1990; Keil et al. 2003):

$$\begin{aligned} \eta_{\text{eq},\nu_e} &= (\mu_e + \mu_p - \mu_n)/k_B T, & \eta_{0,\nu_e} &\equiv 3, \\ \eta_{\text{eq},\bar{\nu}_e} &= -\eta_{\text{eq},\nu_e}, & \eta_{0,\bar{\nu}_e} &\equiv 2, \\ \eta_{\text{eq},\nu_x} &= 0, & \eta_{0,\nu_x} &\equiv 0. \end{aligned} \quad (\text{A.12})$$

With η_ν defined, T_ν can now be calculated from the local average neutrino energy, which is computed from $L_{e,\nu}$ and $L_{n,\nu}$ as

$$\begin{aligned} \langle \epsilon_\nu \rangle &= L_{e,\nu}/L_{n,\nu} = E_\nu(r, t)/n_\nu(r, t) \\ &= \frac{\int_0^\infty d\epsilon \int_{-1}^{+1} d\mu I_{e,\nu}(r, t, \epsilon, \mu)}{\int_0^\infty d\epsilon \int_{-1}^{+1} d\mu I_{n,\nu}(r, t, \epsilon, \mu)} \\ &= k_B T_\nu \mathcal{F}_3(\eta_\nu)/\mathcal{F}_2(\eta_\nu) \end{aligned} \quad (\text{A.13})$$

with the Fermi integrals defined by

$$F_n(\eta) \equiv \int_0^\infty dx x^n f_{\text{FD}}(x, \eta) \quad (\text{A.14})$$

Thus the energy-dependent part of $f_{D,\nu}$ is fully defined. The angle-dependent part is related to the flux factor by

$$f_\nu = F_\nu/c E_\nu = \frac{\int_{-1}^{+1} d\mu \mu I_\nu}{\int_{-1}^{+1} d\mu I_\nu} = \frac{\int_{-1}^{+1} d\mu \mu g_\nu(\mu)}{\int_{-1}^{+1} d\mu g_\nu(\mu)} = \langle \mu_\nu \rangle. \quad (\text{A.15})$$

To solve Eq. (A.5) only f_ν is needed, not the angle-dependent function $g_\nu(\mu)$. Far outside of the neutrinosphere, f_ν is approaching the *vacuum solution*. The latter can be derived under the assumption that neutrinos are emitted isotropically from the sharp surface of a sphere with radius R_ν , which is located at a distance r from the observer. In this case the flux factor is

$$f_{\nu,\text{vac}} = \frac{1}{2} \left[1 + \sqrt{1 - (R_\nu/r)^2} \right]. \quad (\text{A.16})$$

$f_{\nu,\text{vac}}$ approaches 1 for $r \rightarrow \infty$ (*free streaming limit*) and $f_{\nu,\text{vac}} = 1/2$ at the neutrinosphere. In a more realistic situation the neutrinosphere is not a sharp surface but a layer with finite thickness in which neutrinos gradually decouple from the stellar medium. In detailed transport calculations $f_\nu(R_\nu)$ is therefore found to be about 1/4. (see e.g. Janka & Hillebrandt 1989; Janka 1990). How fast f_ν approaches $f_{\nu,\text{vac}}$ (with declining optical depth) depends on the steepness of the density gradient at

the neutrinosphere (Janka 1990). Inside the neutrinosphere detailed transport calculations show that the flux factor behaves roughly like $f_\nu \propto \tau_\nu^m$ with $m < 0$.

Taking all this into account, the following function constitutes a good approximation for the flux factors from detailed transport calculations (Janka 1991, 1990):

$$f_\nu(\tau_\nu) = \begin{cases} \frac{1}{2}[1+D] & \text{if } \tau_\nu < \tau_{\nu,1}, \\ \frac{1}{1+(1+D)(1-D^2)^{(n-1)/2}} & \\ 1/4(\tau_\nu/\tau_{\nu,1})^m, & \text{if } \tau_\nu > \tau_{\nu,1}. \end{cases} \quad (\text{A.17})$$

Here $D = \sqrt{1 - (R_\nu/r)^2}$, the neutrinosphere radius is defined by $\tau_\nu(R_\nu) = \tau_{\nu,1}$ and we adopt $\tau_{\nu,1} = 1.1$. The power-law index m is chosen such that $f_\nu(10) = 1/25$, and n is defined by a local power-law fit of the density profile around the neutrinosphere, $\rho(r) \propto r^{-n}$. A higher value of n therefore means a steeper density gradient.

A.3. Optical Depth

Knowledge of the optical depth is necessary to evaluate Eqs. (A.11) and (A.17). For this purpose it is sufficient to compute τ_ν approximately by considering only the most relevant neutrino processes and assuming that the neutrino spectrum is given by the spectrum for local thermodynamic equilibrium. This means that instead of Eq. (A.10) we use

$$f_{D,\nu}^{\text{eq}}(\epsilon_\nu, r) = f_{\text{FD}} \left(\frac{\epsilon_\nu}{k_B T(r)}, \eta_{\text{eq},\nu}(r) \right) \quad (\text{A.18})$$

with $\eta_{\text{eq},\nu}$ and T instead of η_ν and T_ν .

The “transport optical depth” is defined as the integral

$$\tau_{t,\nu}(r) = \int_r^\infty dr' \langle \kappa_{t,\nu} \rangle(r') \quad (\text{A.19})$$

of the energy-averaged “transport opacity” (i.e. the opacity which is relevant for momentum transfer), $\langle \kappa_{t,\nu} \rangle(r)$.

The most important opacity-producing reactions are scattering off nucleons (n,p) and nuclei (Z_j, A_j), where $j = 1, 2, \dots$ denotes the considered nuclear species, and absorption by neutrons and protons in case of ν_e and $\bar{\nu}_e$, respectively. Thus one can write

$$\langle \kappa_{t,\nu} \rangle = \langle \kappa_\nu^a \rangle + \sum_{i \in \{\text{n,p}, A_j\}} \langle \kappa_{t,\nu}^{s,i} \rangle. \quad (\text{A.20})$$

Here the (neutrino-flavour independent) scattering opacities are

$$\langle \kappa_{t,\nu}^{s,p} \rangle = \frac{1}{6} \left[\frac{5}{4} \alpha^2 + (C_V - 1)^2 \right] \frac{\sigma_0}{(m_e c^2)^2} \langle \epsilon_\nu^2 \rangle n_p, \quad (\text{A.21})$$

$$\langle \kappa_{t,\nu}^{s,n} \rangle = \frac{5\alpha^2 + 1}{24} \frac{\sigma_0}{(m_e c^2)^2} \langle \epsilon_\nu^2 \rangle n_n, \quad (\text{A.22})$$

$$\langle \kappa_{t,\nu}^{s,A_j} \rangle = \frac{1}{6} A_j^2 [C_A - 1 + \frac{Z_j}{A_j} (2 - C_A - C_V)]^2 \times \frac{\sigma_0}{(m_e c^2)^2} \langle \epsilon_\nu^2 \rangle n_{A_j}, \quad (\text{A.23})$$

for scattering off protons, nucleons and nuclei, respectively. The absorption opacities for ν_e and $\bar{\nu}_e$ are

$$\langle \kappa_{\nu_e}^a \rangle = \frac{1}{4} (3\alpha^2 + 1) \frac{\sigma_0}{(m_e c^2)^2} n_n \times \left(\langle \epsilon_{\nu_e}^2 \rangle + 2\Delta \langle \epsilon_{\nu_e} \rangle + \Delta^2 \right) \Theta(\langle \epsilon_{\nu_e} \rangle), \quad (\text{A.24})$$

$$\langle \kappa_{\bar{\nu}_e}^a \rangle = \frac{1}{4} (3\alpha^2 + 1) \frac{\sigma_0}{(m_e c^2)^2} n_p \times \left(\langle \epsilon_{\bar{\nu}_e}^2 \rangle^* + 2\Delta \langle \epsilon_{\bar{\nu}_e} \rangle^* + \Delta^2 \langle \epsilon_{\bar{\nu}_e}^0 \rangle^* \right). \quad (\text{A.25})$$

(see Tubbs & Schramm 1975; Bruenn 1985).

Here $\sigma_0 = 4G_F^2 m_e^2 \hbar^2 / \pi c^2 = 1.76 \times 10^{-44}$ cm (with the Fermi coupling constant G_F), $\Delta = 1.2935$ MeV is the rest mass difference of neutrons and protons, $\alpha = 1.254$, and $C_A = \frac{1}{2}$, $C_V = \frac{1}{2} + 2 \sin^2 \theta_W$ and $\sin^2 \theta_W = 0.23$.

In deriving Eqs. (A.21) – (A.25) (as well as for all rates and source terms given below) the electron and positron rest masses are ignored ($m_e c^2 \ll \epsilon_\nu$) and nucleons and nuclei are assumed to have infinite rest masses ($m_{n,p,A_j} c^2 \gg \epsilon_\nu$). For electrons, phase space blocking is included in Eq. (A.25) by the factor

$$\Theta(\langle \epsilon_\nu \rangle) = 1 - f_{\text{FD}} \left(\frac{\langle \epsilon_\nu \rangle + \Delta}{k_B T}, \eta_e \right), \quad (\text{A.26})$$

which accounts for the fact that a significant fraction of the possible final electron states may be occupied. Phase space blocking can be neglected in $\langle \kappa_{\bar{\nu}_e}^a \rangle$ (Eq. A.25), because the positrons are non-degenerate.

The neutrino energy moments are (generalising Eq. A.13) given by

$$\langle \epsilon_\nu^n \rangle = (k_B T_\nu)^n \frac{\mathcal{F}_{2+n}(\eta_\nu)}{\mathcal{F}_2(\eta_\nu)}, \quad (\text{A.27})$$

$$\langle \epsilon_\nu^n \rangle^* = (k_B T_\nu)^n \frac{\mathcal{F}_{2+n}(\eta_\nu - \Delta/k_B T_\nu)}{\mathcal{F}_2(\eta_\nu)}, \quad (\text{A.28})$$

and for evaluating Eqs. (A.21) – (A.25) to compute $\tau_{t,\nu}$ (Eq. A.19) for use in Eq. (A.17), we take $\eta_\nu = \eta_{\text{eq},\nu}$ and $T_\nu = T$.

In contrast, Eq. (A.11) is evaluated with the “effective optical depth for equilibration”,

$$\tau_\nu(r) = \int_r^\infty dr' \langle \kappa_{\text{eff},\nu} \rangle(r'), \quad (\text{A.29})$$

where the effective opacity is defined as

$$\langle \kappa_{\text{eff},\nu} \rangle = \sqrt{\langle \kappa_\nu^a \rangle \times \langle \kappa_\nu^a + \kappa_{t,\nu}^s \rangle}. \quad (\text{A.30})$$

Here the spectrally averaged absorption opacity, $\langle \kappa_\nu^a \rangle$, is taken to include neutrino-pair annihilation to e^\pm -pairs (Eq. 4), which is assumed to be the most important reaction for producing $\nu_x \bar{\nu}_x$ pairs. Both $\langle \kappa_\nu^a \rangle$ and $\langle \kappa_\nu^a + \kappa_{t,\nu}^s \rangle$ are evaluated for the “true” (not the local equilibrium) neutrino spectrum (i.e. for the spectral temperature T_ν and the spectral degeneracy η_ν instead of T and $\eta_{\text{eq},\nu}$) by employing the source terms from the neutrino transport solution of the last time step.

A.4. Source Terms

Solving Eq. (A.7) requires the knowledge of the emission rates, Q_{ν}^+ , and absorption coefficients, $\tilde{\kappa}_{\nu} = \kappa_{\nu}^a/f_{\nu}$, which appear in this equation. Since Eq. (A.7) is used to determine the number fluxes, $L_{n,\nu}$, and luminosities, $L_{e,\nu}$, of all neutrinos and antineutrinos $\nu \in \{\nu_e, \bar{\nu}_e, \nu_x\}$, the source terms need to be calculated for the neutrino number as well as energy. As in Eq. (A.30), κ_{ν}^a is defined to include the contributions from the β -processes, (Eqs. 2 and 3) for ν_e and $\bar{\nu}_e$ as well as those of e^+e^- pair annihilation (Eq. 4). The absorption coefficient κ_{ν}^a can be computed from the corresponding neutrino absorption rate by

$$\kappa_{\nu}^a = Q_{\nu}^- 4\pi r^2 f_{\nu} / L_{\nu} = (Q_{\nu}^a + Q_{\nu}^{\text{ann}}) 4\pi r^2 f_{\nu} / L_{\nu}. \quad (\text{A.31})$$

For the number transport the neutrino absorption and emission rates (in units of number per cm^3 per second) by charged-current β -reactions between leptons and nucleons can be written with our approximations for the neutrino distribution function and the appropriate statistical weights for the leptons as follows:

$$\mathcal{R}_{\nu_e}^a = \sigma c \frac{L_{e,\nu_e} n_n}{4\pi r^2 c f_{\nu_e}} \frac{\langle \epsilon_{\nu_e}^2 \rangle + 2\Delta \langle \epsilon_{\nu_e} \rangle + \Delta^2}{\langle \epsilon_{\nu_e} \rangle} \Theta(\langle \epsilon_{\nu_e} \rangle), \quad (\text{A.32})$$

$$\mathcal{R}_{\bar{\nu}_e}^a = \sigma c \frac{L_{e,\bar{\nu}_e} n_p}{4\pi r^2 c f_{\bar{\nu}_e}} \frac{\langle \epsilon_{\bar{\nu}_e}^2 \rangle^* + 2\Delta \langle \epsilon_{\bar{\nu}_e} \rangle^* + \Delta^2 \langle \epsilon_{\bar{\nu}_e}^0 \rangle^*}{\langle \epsilon_{\bar{\nu}_e} \rangle}, \quad (\text{A.33})$$

$$\mathcal{R}_{\nu_e}^e = \frac{1}{2} \sigma c n_p n_{e^-} [\langle \epsilon_{e^-}^2 \rangle^* + 2\Delta \langle \epsilon_{e^-} \rangle^* + \Delta^2 \langle \epsilon_{e^-}^0 \rangle^*], \quad (\text{A.34})$$

$$\mathcal{R}_{\bar{\nu}_e}^e = \frac{1}{2} \sigma c n_n n_{e^+} [\langle \epsilon_{e^+}^2 \rangle + 2\Delta \langle \epsilon_{e^+} \rangle + \Delta^2], \quad (\text{A.35})$$

where $\sigma = \frac{1}{4}(3\alpha^2 + 1)\sigma_0/(m_e c^2)^2$.

The electron and positron energy moments are given by

$$\langle \epsilon_e^n \rangle = (k_B T)^n \frac{\mathcal{F}_{2+n}(\eta_e)}{\mathcal{F}_2(\eta_e)}, \quad (\text{A.36})$$

$$\langle \epsilon_e^n \rangle^* = (k_B T)^n \frac{\mathcal{F}_{2+n}(\eta_e - \Delta/k_B T)}{\mathcal{F}_2(\eta_e)}. \quad (\text{A.37})$$

The annihilation and production rates of neutrino number in e^+e^- pair reactions are given by (adapted from Schinder et al. 1987; see also Janka 1991):

$$\mathcal{R}_{\nu}^{\text{ann}} = \frac{\sigma_0 c}{(4\pi r^2 c)^2} \frac{L_{n,\nu} L_{n,\bar{\nu}}}{\langle \epsilon_{\nu} \rangle \langle \epsilon_{\bar{\nu}} \rangle} \left\{ \frac{2}{9} \frac{\Phi(f_{\nu}, \chi_{\nu})}{f_{\nu} f_{\bar{\nu}}} \frac{C_{Av}^2 + C_{V\nu}^2}{(m_e c^2)^2} \langle \epsilon_{\nu} \rangle \langle \epsilon_{\bar{\nu}} \rangle \right. \\ \left. + \frac{1}{6} \frac{1 - f_{\nu} f_{\bar{\nu}}}{f_{\nu} f_{\bar{\nu}}} (2C_{V\nu}^2 - C_{Av}^2) \right\}, \quad (\text{A.38})$$

$$\mathcal{R}_{\nu}^{\text{prod}} = \frac{1}{18} \frac{\sigma_0 c}{(m_e c^2)^2} n_{e^-} n_{e^+} \left\{ (C_{Av}^2 + C_{V\nu}^2) \langle \epsilon_{e^-} \rangle \langle \epsilon_{e^+} \rangle \right. \\ \left. + \frac{3}{4} (m_e c^2)^2 (2C_{V\nu}^2 - C_{Av}^2) \right\}. \quad (\text{A.39})$$

These rates hold for neutrinos ν or antineutrinos $\bar{\nu}$ of all flavours. In Eq. (A.31), \mathcal{R}_{ν}^a and $\mathcal{R}_{\nu}^{\text{ann}}$ have to be used instead of \mathcal{Q}_{ν}^a and $\mathcal{Q}_{\nu}^{\text{ann}}$ for computing the absorption coefficient for the number transport. In Eq. (A.38), $\Phi(f_{\nu}, \chi_{\nu})$ is a geometrical factor,

$$\Phi(f_{\nu}, \chi_{\nu}) = \frac{3}{4} \left[1 - 2f_{\nu} f_{\bar{\nu}} + \chi_{\nu} \chi_{\bar{\nu}} + \frac{1}{2} (1 - \chi_{\nu})(1 - \chi_{\bar{\nu}}) \right], \quad (\text{A.40})$$

where we express the variable Eddington factor χ_{ν} in terms of the flux factor f_{ν} (Eq. A.4) using a statistical form, which was derived by Minerbo (1978) on grounds of maximum entropy considerations (for photons or nondegenerate neutrinos, as assumed here):

$$\chi_{\nu} = \langle \mu_{\nu}^2 \rangle = \frac{1}{3} + \frac{0.01932 f_{\nu} + 0.2694 f_{\nu}^2}{1 - 0.5953 f_{\nu} + 0.02625 f_{\nu}^2}. \quad (\text{A.41})$$

The weak coupling constants in Eqs. (A.38) and (A.39) are given by

$$C_{Av} = \begin{cases} +\frac{1}{2} & \text{for } \nu \in \{\nu_e, \bar{\nu}_e\}, \\ -\frac{1}{2} & \text{for } \nu \in \{\nu_{\mu}, \bar{\nu}_{\mu}, \nu_{\tau}, \bar{\nu}_{\tau}\}, \end{cases} \quad (\text{A.42})$$

$$C_{V\nu} = \begin{cases} +\frac{1}{2} + 2 \sin^2 \theta_W & \text{for } \nu \in \{\nu_e, \bar{\nu}_e\}, \\ -\frac{1}{2} + 2 \sin^2 \theta_W & \text{for } \nu \in \{\nu_{\mu}, \bar{\nu}_{\mu}, \nu_{\tau}, \bar{\nu}_{\tau}\}. \end{cases} \quad (\text{A.43})$$

The source term which describes the rate of change per unit of volume in the evolution equation of the electron lepton number of the stellar medium is

$$Q_N = \dot{Y}_e n_b = (\mathcal{R}_{\nu_e}^a - \mathcal{R}_{\nu_e}^e) - (\mathcal{R}_{\bar{\nu}_e}^a - \mathcal{R}_{\bar{\nu}_e}^e). \quad (\text{A.44})$$

The source terms which account for the absorption and emission of energy through ν_e and $\bar{\nu}_e$ are computed in analogy to Eqs. A.32 – A.32 as

$$\mathcal{Q}_{\nu_e}^a = \sigma c \frac{L_{e,\nu_e} n_n}{4\pi r^2 c f_{\nu_e}} \frac{\langle \epsilon_{\nu_e}^3 \rangle + 2\Delta \langle \epsilon_{\nu_e}^2 \rangle + \Delta^2 \langle \epsilon_{\nu_e} \rangle}{\langle \epsilon_{\nu_e} \rangle} \Theta(\langle \epsilon_{\nu_e} \rangle), \quad (\text{A.45})$$

$$\mathcal{Q}_{\bar{\nu}_e}^a = \sigma c \frac{L_{e,\bar{\nu}_e} n_p}{4\pi r^2 c f_{\bar{\nu}_e}} \times \frac{\langle \epsilon_{\bar{\nu}_e}^3 \rangle^* + 3\Delta \langle \epsilon_{\bar{\nu}_e}^2 \rangle^* + 3\Delta^2 \langle \epsilon_{\bar{\nu}_e}^0 \rangle^*}{\langle \epsilon_{\bar{\nu}_e} \rangle}, \quad (\text{A.46})$$

$$\mathcal{Q}_{\nu_e}^e = \frac{\sigma c}{2} n_p n_{e^-} [\langle \epsilon_{e^-}^3 \rangle^* + 2\Delta \langle \epsilon_{e^-}^2 \rangle^* + \Delta^2 \langle \epsilon_{e^-} \rangle^*], \quad (\text{A.47})$$

$$\mathcal{Q}_{\bar{\nu}_e}^e = \frac{\sigma c}{2} n_n n_{e^+} [\langle \epsilon_{e^+}^3 \rangle + 3\Delta \langle \epsilon_{e^+}^2 \rangle + 3\Delta^2 \langle \epsilon_{e^+} \rangle + \Delta^3]. \quad (\text{A.48})$$

The annihilation or production of energy in neutrinos (ν) by e^+e^- pair reactions is given as

$$\mathcal{Q}_{\nu}^{\text{ann}} = \frac{\sigma_0 c}{(4\pi r^2 c)^2} \frac{L_{e,\nu} L_{e,\bar{\nu}}}{\langle \epsilon_{\nu} \rangle \langle \epsilon_{\bar{\nu}} \rangle} \left\{ \frac{2}{9} \frac{\Phi(f_{\nu}, \chi_{\nu})}{f_{\nu} f_{\bar{\nu}}} \frac{C_{Av}^2 + C_{V\nu}^2}{(m_e c^2)^2} \langle \epsilon_{\nu}^2 \rangle \langle \epsilon_{\bar{\nu}} \rangle \right. \\ \left. + \frac{1}{6} \frac{1 - f_{\nu} f_{\bar{\nu}}}{f_{\nu} f_{\bar{\nu}}} (2C_{V\nu}^2 - C_{Av}^2) \langle \epsilon_{\nu}^2 \rangle \right\}, \quad (\text{A.49})$$

$$\mathcal{Q}_{\nu}^{\text{prod}} = \frac{1}{36} \frac{\sigma_0 c}{(m_e c^2)^2} n_{e^-} n_{e^+} \times \left\{ [\langle \epsilon_{e^-}^2 \rangle \langle \epsilon_{e^+} \rangle + \langle \epsilon_{e^+}^2 \rangle \langle \epsilon_{e^-} \rangle] (C_{Av}^2 + C_{V\nu}^2) \right. \\ \left. + \frac{3}{4} (m_e c^2)^2 [\langle \epsilon_{e^-} \rangle + \langle \epsilon_{e^+} \rangle] (2C_{V\nu}^2 - C_{Av}^2) \right\}. \quad (\text{A.50})$$

For annihilation of antineutrino ($\bar{\nu}$) energy, $\langle \epsilon_{\bar{\nu}}^2 \rangle$ has to be replaced by $\langle \epsilon_{\bar{\nu}}^2 \rangle^*$ and $\langle \epsilon_{\nu} \rangle$ has to be exchanged with $\langle \epsilon_{\bar{\nu}} \rangle$ in Eq. (A.49), while the production of ν and $\bar{\nu}$ was assumed to be symmetric and both rates are given by Eq. (A.50).

Table A.1. Weak coupling constants for ν and $\bar{\nu}$ scattering off e^+ or e^- (cf. Eq. A.51). C_3^x stands for $C_3^x = (C_A - 1)^2 - (C_V - 1)^2$, $C_A = \frac{1}{2}$, $C_V = \frac{1}{2} + 2 \sin^2 \theta_W$, and ν_x can be ν_μ or ν_τ .

	C_1	C_2	C_3
$\nu_e e^-$	$(C_V + C_A)^2$	$(C_V - C_A)^2$	$C_A^2 - C_V^2$
$\nu_e e^+$	$(C_V - C_A)^2$	$(C_V + C_A)^2$	$C_A^2 - C_V^2$
$\bar{\nu}_e e^-$	$(C_V - C_A)^2$	$(C_V + C_A)^2$	$C_A^2 - C_V^2$
$\bar{\nu}_e e^+$	$(C_V + C_A)^2$	$(C_V - C_A)^2$	$C_A^2 - C_V^2$
$\nu_x e^-$	$(C_V + C_A - 2)^2$	$(C_V - C_A)^2$	C_3^x
$\nu_x e^+$	$(C_V - C_A)^2$	$(C_V + C_A - 2)^2$	C_3^x
$\bar{\nu}_x e^-$	$(C_V - C_A)^2$	$(C_V + C_A - 2)^2$	C_3^x
$\bar{\nu}_x e^+$	$(C_V + C_A - 2)^2$	$(C_V - C_A)^2$	C_3^x

Also in scattering processes energy can be exchanged between neutrinos and the stellar medium. For scattering off e^- or e^+ , using the rates of Tubbs & Schramm (1975), the following expression for the energy transfer rate per unit of volume can be derived (see Janka 1991):

$$\begin{aligned} Q_{\nu e} = & \frac{1}{12} (C_1 + \frac{1}{6} C_2) \frac{\sigma_0 c}{(m_e c^2)^2} n_e \frac{L_{e,\nu}}{4\pi r^2 c f_\nu \langle \epsilon_\nu \rangle} \\ & \left[\left\langle \epsilon_\nu^2 \right\rangle \left(\langle \epsilon_e \rangle + \frac{3}{4} m_e c^2 \right) - \langle \epsilon_\nu \rangle \langle \epsilon_e^2 \rangle \right] \\ & + \frac{3}{8} \frac{C_3}{C_1 + \frac{1}{3} C_2} (m_e c^2)^2 \left[\langle \epsilon_\nu \rangle - \frac{\langle \epsilon_e^2 \rangle}{\langle \epsilon_e \rangle} \right], \end{aligned} \quad (\text{A.51})$$

where e can be e^+ or e^- and ν stands for neutrinos or antineutrinos of all flavours and the constants C_1, C_2, C_3 for the different combinations are listed in Table A.1.

Every transfer by neutrino-nucleon scattering, which is only “nearly conservative”, is taken into account following Tubbs (1979). The corresponding rate is (see Janka 1991):

$$\begin{aligned} Q_{\nu N} = & \frac{1}{4} \frac{\sigma_0 c}{(m_e c^2)^2} C_N \mathcal{E}_N \frac{n_N}{m_N c^2} \left\{ \langle \epsilon_\nu^4 \rangle - 6T \langle \epsilon_\nu^3 \rangle \right\} \\ & \times \frac{L_{e,\nu}}{4\pi r^2 c f_\nu \langle \epsilon_\nu \rangle} \end{aligned} \quad (\text{A.52})$$

with

$$C_N \mathcal{E}_N = \begin{cases} \frac{2}{3} [(C_V - 1)^2 + \frac{5}{4} \alpha^2] & \text{for } N = p, \\ \frac{1}{6} (1 + 5\alpha^2) & \text{for } N = n. \end{cases}$$

The symbol ν stands again for neutrinos and antineutrinos of all flavours. Also scattering contributions are included in the energy generation rate Q^+ and absorption coefficient $\tilde{\kappa}$ used in Eq. (A.7). Considering scattering as an absorption process followed immediately by an emission process, we add the net energy exchange rates $Q_{\nu e^-}$, $Q_{\nu e^+}$, $Q_{\nu p}$ and $Q_{\nu n}$ to Q_ν^- (used for computing $\tilde{\kappa}_\nu$ in Eq. A.7) when the rates are positive (i.e. in case of energy transfer from neutrinos to the stellar gas), and the absolute values of $Q_{\nu e^-}$, $Q_{\nu e^+}$, $Q_{\nu p}$ and $Q_{\nu n}$ to Q_ν^+ otherwise. The total neutrino energy source term to be used in the gas energy equation including the contributions from ν_e and $\bar{\nu}_e$ absorption

and emission, $\nu\bar{\nu}$ pair production, and all scattering reactions is

$$\begin{aligned} Q_E = & \sum_{\nu \in \{\nu_e, \bar{\nu}_e\}} (Q_\nu^a - Q_\nu^e) + \sum_{\nu \in \{\nu_e, \nu_\mu, \nu_\tau\}} (Q_{\nu\bar{\nu}}^{\text{ann}} - Q_{\nu\bar{\nu}}^{\text{prod}}) \\ & + \sum_{\nu \in \{\nu_e, \nu_\mu, \nu_\tau, \bar{\nu}_e, \bar{\nu}_\mu, \bar{\nu}_\tau\}} (Q_{\nu e^+}^s + Q_{\nu e^-}^s + Q_{\nu p}^s + Q_{\nu n}^s), \end{aligned} \quad (\text{A.53})$$

where $Q_{\nu\bar{\nu}}^{\text{ann}} = Q_\nu^{\text{ann}} + Q_{\bar{\nu}}^{\text{ann}}$ and $Q_{\nu\bar{\nu}}^{\text{prod}} = Q_\nu^{\text{prod}} + Q_{\bar{\nu}}^{\text{prod}}$.

In practise, however, the lepton number source term Q_N as well as the energy source term for the hydrodynamics part of the code is not computed from Eq. (A.44) and (A.53), respectively, but from the luminosity change between points (r^i, t^n) and (r^*, t^*) (cf. Fig. A.1). The source terms \tilde{Q}_N^i and \tilde{Q}_E^i for a grid cell i at time level t^n are then given by

$$\tilde{Q}_N^i = \frac{L_n^{\text{diff}}(r^i, t^n) - L_n^{\text{diff}}(r^*, t^*)}{\Delta V_i}, \quad (\text{A.54})$$

$$\tilde{Q}_E^i = \frac{L_e^{\text{tot}}(r^i, t^n) - L_e^{\text{tot}}(r^*, t^*)}{\Delta V_i}, \quad (\text{A.55})$$

where $\Delta V_i = \frac{4\pi}{3} (r_i^3 - r^*{}^3)$ is the part of the cell volume crossed by the characteristic line between (r^i, t^n) and (r^*, t^*) , L_e^{tot} is the sum of the luminosities of neutrinos and antineutrinos of all flavours, and L_n^{diff} is the difference between the ν_e and $\bar{\nu}_e$ number fluxes, $L_{\nu_e, n} - L_{\bar{\nu}_e, n}$. Equations (A.54) and (A.55) work well as a description of the neutrino sources in the gas equations only, if the neutrino fluxes do not exhibit a large degree of variability on the radial and temporal scales of the r - t cells. This, however, is reasonably well fulfilled in the context considered in this paper.

Finally, the outgoing neutrino fluxes transfer also momentum to the stellar fluid. To account for this, we include a momentum source term Q_M which enters the Euler equation of the hydrodynamics solver. It is sufficient to include only the most important reactions, by which neutrinos transfer momentum, i.e. ν_e and $\bar{\nu}_e$ absorption on n and p , respectively, and the scattering processes of ν and $\bar{\nu}$ of all flavours off nucleons and nuclei (pair processes and electron/positron scattering can be safely ignored). For a neutrino or antineutrino ν , the corresponding rate (in units of erg/cm⁴) is

$$Q_M^\nu = \frac{L_{e,\nu}}{4\pi r^2 c} \left(\frac{\langle \kappa_\nu^a \epsilon_\nu \rangle}{\langle \epsilon_\nu \rangle} + \sum_{i \in \{p, n, A_j\}} \frac{\langle \kappa_{i,\nu}^{s,i} \epsilon_\nu \rangle}{\langle \epsilon_\nu \rangle} \right), \quad (\text{A.56})$$

where the first term in the sum is relevant only for ν_e and $\bar{\nu}_e$. The energy averages of the scattering transport opacities, $\kappa_{i,\nu}^{s,i}$, and of the absorption opacities, κ_ν^a , all weighted by the neutrino

energy, are given by

$$\langle \kappa_{t,v}^{s,p} \epsilon_v \rangle = \frac{1}{6} \left[\frac{5}{4} \alpha^2 + (C_V - 1)^2 \right] \frac{\sigma_0}{(m_e c^2)^2} \langle \epsilon_v^3 \rangle n_p, \quad (A.57)$$

$$\langle \kappa_{t,v}^{s,n} \epsilon_v \rangle = \frac{5\alpha^2 + 1}{24} \frac{\sigma_0}{(m_e c^2)^2} \langle \epsilon_v^3 \rangle n_n, \quad (A.58)$$

$$\langle \kappa_{t,v}^{s,A_j} \epsilon_v \rangle = \frac{1}{6} A_j^2 \left[C_A - 1 + \frac{Z_j}{A_j} (2 - C_A - C_V) \right] \frac{\sigma_0}{(m_e c^2)^2} \langle \epsilon_v^3 \rangle n_{A_j}, \quad (A.59)$$

$$\langle \kappa_{v_e}^a \epsilon_{v_e} \rangle = \frac{1}{4} (3\alpha^2 + 1) \frac{\sigma_0}{(m_e c^2)^2} \times \left(\langle \epsilon_{v_e}^3 \rangle + 2\Delta \langle \epsilon_{v_e}^2 \rangle + \Delta^2 \langle \epsilon_{v_e} \rangle \right) \Theta(\langle \epsilon_{v_e} \rangle), \quad (A.60)$$

$$\langle \kappa_{\bar{v}_e}^a \epsilon_{\bar{v}_e} \rangle = \frac{1}{4} (3\alpha^2 + 1) \frac{\sigma_0}{(m_e c^2)^2} \times \left(\langle \epsilon_{\bar{v}_e}^3 \rangle^* + 3\Delta \langle \epsilon_{\bar{v}_e}^2 \rangle^* + 3\Delta^2 \langle \epsilon_{\bar{v}_e} \rangle^* + \Delta^3 \langle \epsilon_{\bar{v}_e}^0 \rangle^* \right). \quad (A.61)$$

The energy moments $\langle \epsilon_v^n \rangle$ and $\langle \epsilon_v^n \rangle^*$ are given in Eqs. (A.27) and (A.28). They are calculated using the nonequilibrium neutrino spectral parameters T_v and η_v . The momentum source term in the equation of gas motion then reads

$$Q_M = \sum_{v \in \{v_e, v_\mu, v_\tau, \bar{v}_e, \bar{v}_\mu, \bar{v}_\tau\}} Q_M^v \quad (A.62)$$

It was not included in the simulations presented in this paper, but will be taken into account in future calculations.

The implementation of the source terms \tilde{Q}_N , \tilde{Q}_E , and Q_M into the framework of our PPM hydrodynamics code was discussed in detail by Rampp & Janka (2002) and Buras et al. (2005a).

We finish by pointing out that the approximative neutrino transport scheme developed here employs two basic assumptions, which are radical simplifications of the true situation:

1. In deriving Eq. (A.7) from the transport equation we assumed that the flux factor $f(r, t)$ is a *known* function, although it is actually dependent on the solution of the transport problem (see Eq. A.4). Equation (A.7) certainly has the advantage of analytic simplicity, but also has a severe disadvantage: The source terms can be very large and the numerical use requires a very fine grid zoning at high optical depths. The cell size should fulfil the constraint that the optical depth of the cell stays around unity or less. Moreover, the implementation of the source terms in (A.7) and the medium sources (Eqs. A.54, A.55) is not symmetric and the numerical scheme does not strictly conserve the total lepton number and total energy of neutrinos plus gas.
2. For treating the spectral dependence, we made the assumption that the neutrino phase space distribution function can be factorised into a product of an angle-dependent function g_v and an energy-dependent term, which we assume to be of Fermi-Dirac shape. This certainly constrains the spectral shape, but the factorisation also implies that the flux-factor is assumed not to be an energy-dependent quantity. This in turn means that the mean energy of the neutrinos flux, $\langle \epsilon_v \rangle_{\text{flux}} \equiv L_{e,v}(r, t)/L_{n,v}(r, t)$ is identical with the mean energy of the local neutrino density, $\langle \epsilon_v \rangle_{\text{local}} \equiv E_v(r, t)/n_v(r, t)$.

This is certainly a problematic simplification in view of the fact that the neutrino interactions with the stellar medium are strongly energy-dependent.

Nevertheless, the described neutrino transport treatment represents a practical approximation which is able to reproduce basic features of more detailed transport solutions and yields agreement with those even beyond the purely qualitative level.

Appendix B: Hydrodynamics in an accelerated frame of reference

In an inertial frame of reference the hydrodynamic equations are given by

$$\frac{\partial \rho}{\partial t} + \nabla \cdot (\rho \mathbf{v}) = 0, \quad (B.1)$$

$$\rho \left(\frac{\partial \mathbf{v}}{\partial t} + (\mathbf{v} \cdot \nabla) \mathbf{v} \right) - \nabla \mathcal{P} = \rho \mathbf{g}, \quad (B.2)$$

$$\frac{\partial \rho E}{\partial t} + \nabla \cdot ((\rho E + \mathcal{P}) \mathbf{v}) = \rho \mathbf{v} \cdot \mathbf{g}, \quad (B.3)$$

where ρ is the density, \mathbf{v} is the velocity, \mathcal{P} is the pressure, \mathbf{g} is the gravitational acceleration and $E = \epsilon + v^2/2$ is the sum of internal energy, ϵ , and kinetic energy, ϵ_{kin} , per unit mass.

Let AF be a frame of reference that coincides with an inertial frame IF at time $t = 0$ and accelerates with a constant rate \mathbf{a} in z -direction, $\mathbf{a} = a \mathbf{e}_z$. The Cartesian coordinates of both frames are then related by

$$(x', y', z', t') = (x, y, z - at^2/2, t) \quad (B.4)$$

(primed quantities are used for the accelerated frame), which implies that

$$\partial z'(x, y, z, t)/\partial t = -at \quad \text{and} \quad \partial z(x', y', z', t')/\partial t' = at. \quad (B.5)$$

For density, pressure, velocity, kinetic energy and gravitational acceleration the following relations hold:

$$\begin{aligned} \rho'(x', y', z', t) &= \rho(x, y, z, t), \\ \mathcal{P}'(x', y', z', t) &= \mathcal{P}(x, y, z, t), \\ \mathbf{v}'(x', y', z', t) &= \mathbf{v}(x, y, z, t) - a \mathbf{e}_z \\ \epsilon'_{\text{kin}}(x', y', z', t) &= \epsilon_{\text{kin}}(x, y, z, t) - v_z^2/2 + (v_z - at)^2/2, \\ \mathbf{g}'(x', y', z', t) &= \mathbf{g}(x, y, z, t) - a \mathbf{e}_z. \end{aligned} \quad (B.6)$$

From relations (B.4)–(B.6), it is easy to see that the equation of mass conservation (B.1) does not change in the accelerated frame. The momentum equation in this frame is

$$\rho' \left(\frac{\partial \mathbf{v}'}{\partial t} + (\mathbf{v}' \cdot \nabla') \mathbf{v}' \right) + \nabla' \mathcal{P}' - \rho' \mathbf{g}' = -at \rho \left(\frac{\partial v_x}{\partial z} \mathbf{e}_x + \frac{\partial v_y}{\partial z} \mathbf{e}_y \right).$$

Note that in contrast to Eq. (B.2) there is now an additional term on the right hand side, which affects the momentum components perpendicular to the direction of acceleration. Thus for instance the x -component of the time derivative of the velocity is

$$\frac{\partial v'_x}{\partial t} = - \left(v'_x \frac{\partial v'_x}{\partial x'} + v'_y \frac{\partial v'_x}{\partial y'} + v'_z \frac{\partial v'_x}{\partial z'} \right) - \frac{1}{\rho'} \frac{\partial \mathcal{P}'}{\partial x'} + g'_x - at \frac{\partial v_x}{\partial z}, \quad (B.7)$$

where the additional (rightmost) term is negligible compared to $v'_z (\partial v'_x / \partial z')$, as long as $|at| \ll |v_z|$.

Similarly, it can be shown that the additional terms arising in the energy equation (B.3) for an accelerated frame of reference are of order t^2 and can also be neglected, as long as $|at| \ll |v_z|$ holds.

Within a typical time step Δt of a supernova simulation (of order 10^{-6} s) the condition $|a\Delta t| \ll |v_z|$ is satisfied, because the maximum neutron star accelerations are of $\mathcal{O}(10^8 \text{ cm/s}^2)$, and hence $|a\Delta t| = \mathcal{O}(100 \text{ cm/s})$, which is much smaller than the relevant velocities in the simulations, which are of $\mathcal{O}(10^6 \text{ cm/s})$. Thus a solution of the inertial frame hydrodynamics equations with the simple replacement $\mathbf{g} \rightarrow \mathbf{g}' = \mathbf{g} - \mathbf{a}$ should yield an excellent approximation to the solution of the hydrodynamic equations in the accelerated frame.

Unfortunately, in the present problem the neutron star acceleration, and hence the instantaneous acceleration of the frame, $\mathbf{a}(t)$, is not known *a priori*, because it is coupled to the solution of the hydrodynamic problem during a considered time step. Therefore we need to make use of an operator-splitting approach, in which we first ignore the acceleration of the frame of reference and simply solve the inertial frame hydrodynamics equations (just using the gravitational acceleration \mathbf{g}). We can then compute the current value of $\mathbf{a}(t)$, which is assumed to be constant over the time step, using momentum conservation: The sum of the momenta of the neutron star core, \mathbf{P}_{core} , and the matter on the numerical grid, \mathbf{P}_{grid} , is conserved and initially zero, so that $\Delta \mathbf{P}_{\text{core}} = -\Delta \mathbf{P}_{\text{grid}}$. We can then use the relation

$$\mathbf{a}(t^n) = -\frac{\mathbf{P}_{\text{grid}}(t^n) - \mathbf{P}_{\text{grid}}(t^{n-1})}{M_{\text{core}} \Delta t} \quad (\text{B.8})$$

to determine the acceleration in this time step. Finally we take the effects of the global acceleration of our frame into account in a second step, by adding $-\mathbf{a}(t^n) \Delta t$ to the hydrodynamic velocity in each zone of the grid, in essence performing a Galilei transformation to an instantaneous inertial frame in which the neutron star is again at rest.

Appendix C: Explosion energy

The explosion energy of neutrino-driven supernovae consist of two major contributions. The first is the recombination energy of the matter in the gain layer at the onset of the explosion. This matter consists of free nucleons and alpha particles at the time the explosion starts. Almost all of this mass (except for some fraction in the downflows, which is accreted onto the neutron star) ends up in a dense shell behind the expanding shock. As the shock propagates outward, the temperature in this expanding shell decreases and the matter recombines to α -particles and later to nuclei.

Figure C.1 displays the available recombination energy of the matter in the gain layer at the time of the explosion,

$$E_{\text{rec}}^{\text{gain}}(t_{\text{exp}}) = \int_{\text{gain layer}} \epsilon_{\text{rec}}(r, t_{\text{exp}}) dV. \quad (\text{C.1})$$

Here $\epsilon_{\text{rec}}(r, t)$ denotes the density of recombination energy available when matter consists of nucleons, α -particles and

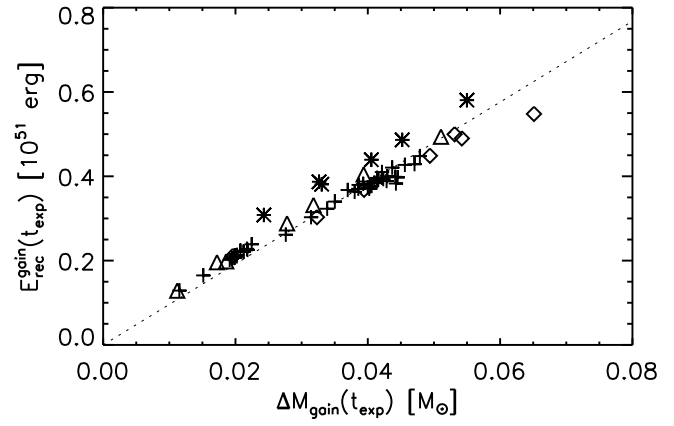


Fig. C.1. Available recombination energy, $E_{\text{rec}}^{\text{gain}}$, as a function of the mass in the gain layer, ΔM_{gain} , at the time of explosion for the models of Tables 1–5. The slope of this approximately linear relation corresponds to about 5 MeV per baryon (dotted line).

some mass fraction of heavy nuclei,

$$\epsilon_{\text{rec}}(r, t) = B_h n_h^{\text{max}}(r, t) - (B_\alpha n_\alpha(r, t) + B_h n_h(r, t)), \quad (\text{C.2})$$

with B_h and B_α being the binding energies of a representative heavy nucleus ($Z_h, A_h = N_h + Z_h$) from the iron group (as assumed in our equation of state) and of α -particles, respectively, and $n_h^{\text{max}} = \min(n_p^{\text{tot}}/Z_h, n_n^{\text{tot}}/N_h)$ and n_h are the maximum and current number densities, respectively, of this heavy nucleus when n_p^{tot} and n_n^{tot} are the total (bound+free) number densities of protons and neutrons.

Figure C.1 shows that for all models of Tables 1–5 $E_{\text{rec}}^{\text{gain}}(t_{\text{exp}}) \approx N_b^{\text{gain}}(t_{\text{exp}}) \times 5 \text{ MeV}$, when N_b^{gain} is the total number of baryons in the gain layer. This means that due to the partial assembly of free n and p in α -particles at the time of explosion, about 5 MeV (instead of > 8 MeV) remain available for being released by recombination during the subsequent expansion and cooling.

This recombination is essentially complete when the shock has reached a radius of 3000 km (recombination to α -particles happens even much earlier). We denote this time by t_{rec} . Figure C.2 demonstrates that the explosion energy at time t_{rec} , $E_{\text{exp}}(t_{\text{rec}})$, roughly equals the available recombination energy, $E_{\text{rec}}^{\text{gain}}(t_{\text{exp}})$, at the onset of the explosion. This means that neutrino heating essentially has the effect of lifting the total energy of mass elements in the gain layer close to zero (i.e., $\epsilon_{\text{tot}} = \epsilon_{\text{kin}} + \epsilon_{\text{int}} + \epsilon_{\text{grav}} \approx 0$) and thus makes this matter unbound and enables its expansion in the gravitational potential of the forming neutron star. The excess energy of this matter at time t_{rec} , i.e. $E_{\text{exp}}(t_{\text{rec}})$, is provided by the recombination of nucleons to α -particles and finally to iron-group nuclei. Only in case of higher explosion energies, $E_{\text{exp}}(t_{\text{rec}})$ is clearly larger than $E_{\text{rec}}^{\text{gain}}(t_{\text{exp}})$ (Fig. C.2). In this case neutrino heating in the gain layer is stronger and the heating time scale of the matter there shorter than the expansion time scale when the shock begins to accelerate outwards. Therefore neutrinos are able to

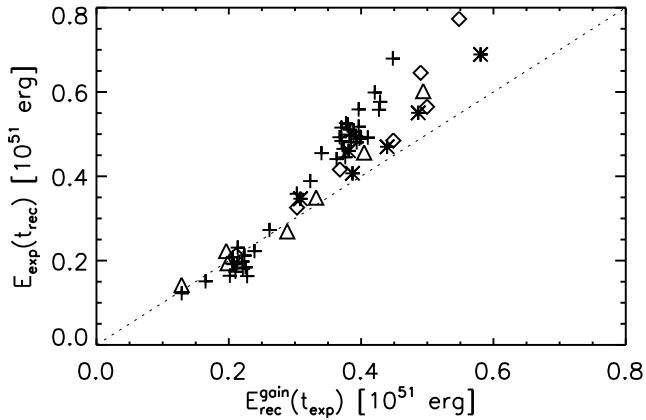


Fig. C.2. Explosion energy after the recombination of the ejecta, $E_{\text{exp}}(t_{\text{rec}})$, as a function of the available recombination energy in the gain layer at the onset of the explosion, $E_{\text{rec}}^{\text{gain}}(t_{\text{exp}})$, for the models of Tables 1–5. For low explosion energies the two quantities agree well.

deposit “excess energy” in the ejecta before they have moved out of the region of strong heating.

The second contribution to the explosion energy comes from the neutrino-driven baryonic wind which sets in after the surroundings of the nascent neutron star have been cleaned from the initially heated gas. Indeed this wind is an important energy source at “late” times. To demonstrate this, we compare the time derivative of the explosion energy, dE_{exp}/dt , with the wind power, L_{wind} , and the net energy loss/gain rate L_{shock} at the shock (Fig. C.3). The curve for dE_{exp}/dt in Fig. C.3 is calculated as the numerical derivative of the energy integral

$$E_{\text{exp}}(t) = \int_{V^+} \epsilon_{\text{tot}}(r, t) dV, \quad (\text{C.3})$$

where the integration is performed over the volume V^+ , in which the total energy $\epsilon_{\text{tot}}(r, t)$ is positive (see also Eq. 23). For $t > t_{\text{rec}}$ this volume fills the region between an inner boundary at $r \approx 200$ km and the shock (except for some parts of the accretion downflows, where ϵ_{tot} may still be negative).

The explosion energy is subject to changes by $\mathcal{P}dV$ -work performed at, and by energy fluxes through the boundaries of V^+ , in particular by the wind, whose power is given by the surface integral

$$L_{\text{wind}} = \oint_{r=200 \text{ km}} (\epsilon_{\text{tot}} + \epsilon_{\text{rec}} + \mathcal{P}) \max(v_r, 0) dS. \quad (\text{C.4})$$

This expression takes into account the total energy ($\epsilon_{\text{tot}} = \rho e_{\text{tot}}$ with e_{tot} defined by Eq. 24) of the wind material streaming through the inner boundary radius into V^+ , the energy that will be set free at larger radii by recombination (Eq. C.1), as well as the work performed by pressure forces. Here we have neglected effects due to downflows by omitting contributions to the surface integral from zones with negative radial velocity.

The change of the explosion energy due to energy flow through the outer boundary of V^+ (i.e., the shock), is given by

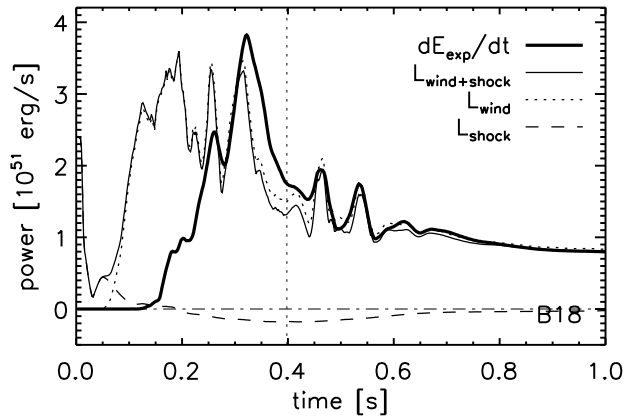


Fig. C.3. Evolution of the time derivative of the explosion energy (dE_{exp}/dt , thick solid) for Model B18. Also shown are the wind power at a radius of 200 km (L_{wind} , dotted), the energy loss/gain rate at the shock by $\mathcal{P}dV$ work and swept-up matter (L_{shock} , dashed), and the sum of the latter two quantities ($L_{\text{wind}+\text{shock}}$, thin solid). $L_{\text{wind}+\text{shock}}$ agrees well with dE_{exp}/dt for $t > t_{\text{rec}}$ (right of the vertical line).

the net energy loss/gain rate

$$L_{\text{shock}} = \oint_{r=R_s(\theta)^+} [(\epsilon_{\text{tot}} + \epsilon_{\text{rec}} + \mathcal{P}) v_r + (\epsilon_{\text{tot}} + \epsilon_{\text{rec}}) \dot{R}_s] dS. \quad (\text{C.5})$$

The integration has to be performed over a surface located slightly upstream of the shock. Compared to Eq. (C.4) an additional term arises here from the motion of the shock, which propagates with a local velocity $\dot{R}_s(\theta)$.

Figure C.3 shows that these two terms explain the evolution of dE_{exp}/dt for $t > t_{\text{rec}}$, i.e.

$$dE_{\text{exp}}/dt \approx L_{\text{wind}} + L_{\text{shock}} \quad (\text{C.6})$$

holds at late times, and the thin and thick solid lines in Fig. C.3 almost coincide. Note also that $L_{\text{wind}} \gg |L_{\text{shock}}|$. This is true for all our models, and therefore the increase of the explosion energy after about 0.5 s post bounce is (almost exclusively) associated with the time-integrated wind power (see Fig. C.4).

The relative importance of the two major constituents of the explosion energy that we have discussed here, i.e., the nuclear recombination energy of the matter in the gain layer and the integrated power of the neutrino-driven wind, varies with the explosion energy. In our “standard boundary contraction” models the fraction of the explosion energy provided by recombination drops from about 70% for the low-energy models to about 30% for the model with $E_{\text{exp}}(1 \text{ s}) \approx 1.5 \times 10^{51} \text{ erg}$ (Fig. C.5). This fraction declines because the wind power is proportional to a higher power of the luminosity ($L_{\text{wind}} \propto L_{\nu}^{\alpha}$ with $\alpha \approx 3$; Thompson et al. 2001) and although the mass in the gain layer at the onset of the explosion scales linearly with the boundary luminosity (Fig. 13).

For the “rapid boundary contraction” cases the wind contribution is even more important, e.g. for Model W12F- $E_{\text{rec}}^{\text{gain}}(t_{\text{exp}})/E_{\text{exp}}(1 \text{ s}) \approx 0.2$, i.e. about 80% of the explosion energy are generated by the neutrino-driven wind. For a

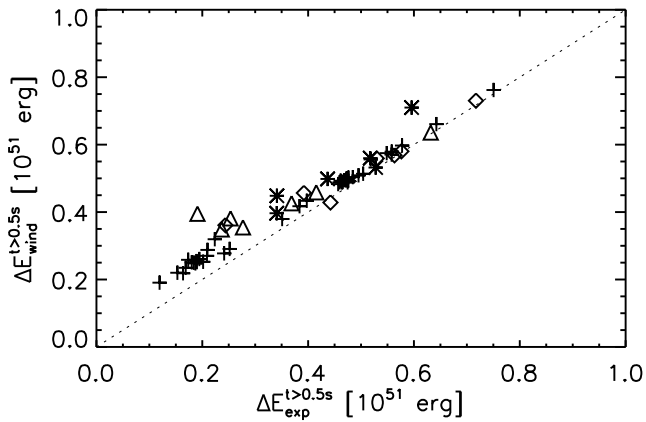


Fig. C.4. Relation between the increase of the explosion energy between $t = 0.5$ s and $t = 1$ s, $\Delta E_{\text{exp}}^{t>0.5\text{s}}$, and the integrated wind power during this time interval, $\Delta E_{\text{wind}}^{t>0.5\text{s}}$, for the models of Tables 1–5.

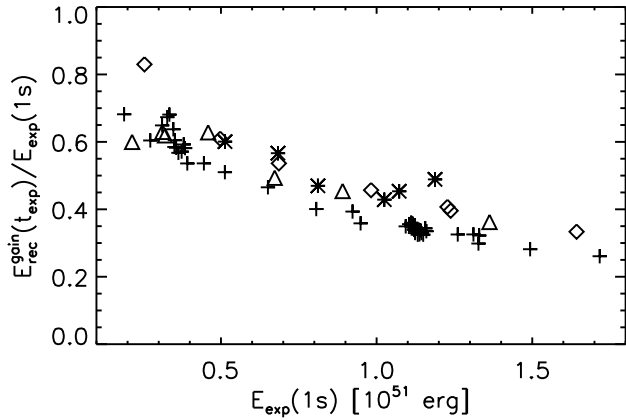


Fig. C.5. Ratio of the recombination contribution to the total explosion energy 1 s after core bounce, $E_{\text{rec}}^{\text{gain}}(t_{\text{exp}})/E_{\text{exp}}(1\text{ s})$, as a function of $E_{\text{exp}}(1\text{ s})$ for the models of Tables 1–5. For low-energy models the recombination contribution dominates, whereas for higher explosion energies the wind contribution becomes more important.

fixed boundary luminosity the wind power is higher in this case than for the “standard boundary contraction”, because L_{wind} increases with decreasing neutron star radius (see e.g. Thompson et al. 2001). However, $\Delta M_{\text{gain}}(t_{\text{exp}})$, and thus also $E_{\text{rec}}^{\text{gain}}(t_{\text{exp}})$, are similar for models with “standard” and “rapid” boundary contraction and the same L_{ib} . This is so because two effects compensate each other roughly: On the one hand the density at a given radius r in the gain layer is lower for a faster contraction ($\rho^r(r, t_{\text{exp}}^r) < \rho^s(r, t_{\text{exp}}^s)$, where r and s denote the rapid and standard contraction cases, respectively), but on the other hand also the gain radius is smaller and thus located in a region of higher density, $\rho^r(R_g, t_{\text{exp}}^r) > \rho^s(R_g, t_{\text{exp}}^s)$.

Figure 22 indicates that the explosion energy is still increasing at $t = 1$ s when we stopped most of our simulations. Yet, with the subsequent drop of the core luminosity (we assume a $t^{-3/2}$ behaviour at $t > t_L$, see Eq. 13) also the wind power, which

is proportional to L_{v}^{α} (with $\alpha \approx 3$; Thompson et al. 2001), must decline strongly. Therefore the explosion energy will grow only moderately. In case of the long-time simulation B18-It it rose from 1.14×10^{51} erg at $t = 1$ s to 1.43×10^{51} erg at $t = 2$ s, and reached 1.46×10^{51} erg by the end of the simulation at $t = 3.6$ s.